TURBO

Scientific Journal

Diplomă

Locul 2

Locul 2 în Top Afaceri România 2020

INSTITUTUL NATIONAL DE CERCETARE DEZVOLTARE TURBOMOTOARE COMOTI

Top pentru Romania Intreprinderi cu Capital Romanesc, judetul BUCURESTI, domeniul 72: Cercetare-dezvoltare, conform bilant 2019.

Certificat de
ListaFirme.ro

COMOTI
WORKS FOR
A BETTER WORLD

Diplomă

Locul 3

Locul 3 în Top Afaceri România 2020

INSTITUTUL NATIONAL DE CERCETARE DEZVOLTARE TURBOMOTOARE COMOTI

Top pentru Romania, judetul BUCURESTI, domeniul 72: Cercetare-dezvoltare, conform bilant 2019.

Certificat de
ListaFirme.ro

Editorial Board

CONTENT

Editorial

Timpul îşi are propriul curs

După Al Doilea Război Mondial uzina Volkswagen, aflată sub control britanic și în pragul falimentului traversa o perioadă grea, de aceea se impunea redresarea. Un potențial cumpărător a fost chiar Ford, care a venit în Germania pentru a vedea ce era de văzut. Dând cu ochii de celebra mașină Beetle, Ford a decis să nu cumpere fabrica: *Este cea mai ridicolă mașină pe care am văzut-o vreodată, Beetle nu va avea niciodată succes pe piață!*

Însă un personaj, în treacăt fie spus evreu, creatorul de imagine William Bernbach, maestru vizionar al campaniilor publicitare *Think Small* și *Lemon*, a făcut din Beetle una dintre cele mai celebre și vândute mașini din lume, iar Wolkswagen și-a câștigat notorietatea prin lansarea clasei de mașini mici la prețuri mici înaintea altor producători concurenți.

A fost un mod în care realitatea ne-a arătat cum căutarea asiduă a căilor de ieșire din marile crize conduce la salturi majore. În cazul crizei anilor 1929-1933 s-a ajuns la performanțe tehnologice în inginerie, aviație civilă și militară, în construcțiile de înaltă complexitate sau în industria energetică, iar mai târziu, sub presiunea crizei sistemice din perioada 1971-1975 s-a dat startul erei tehnologice: microelectronică, tehnologia calculatoarelor, internet, comunicații mobile. În mod evident natura unei crizei economice se reflectă de fiecare dată în ciclurile mari ale economiei.

Până la începutul anului 2020, omenirea avea să cunoască o dezvoltare impresionantă prin uriașe progrese științifice și tehnologice. Oamenii de știință au descoperit cele mai intime secrete ale universului, tehnologiile supercomputer și inteligența artificială, au introdus economia digitală, comerțul serviciilor și obiectelor pe internet, robotica și contactele rapide nelimitate. Savanții au promis pentru următoarele decenii o eră tehnologică nouă, cu energie infinită, materiale noi miraculoase, tinerețe veșnică.

S-au construit stadioane futuriste, săli de concert inimaginabile, hoteluri de lux, stațiuni la modă, restaurante și turism de masă, toate au ilustrat o bunăstare evidentă și un tip de accesibilitate a tuturor acestor răsfățuri. Omenirea a pășit în regatul euforiei fără să-și dea seama, ba mai mult: a uitat! Lecțiile istoriei au fost uitate! Pandemiile au fost uitate!

Acum pandemia coronavirusului ne-a lovit pe toți iar *Lumea* a devenit brusc diferită și nu se va mai întoarce niciodată la vechea stare de fapt, cu tot ce presupunea până mai ieri, ca abordare a valorilor materiale și spirituale. Dezbaterile mondiale pe teme filosofice, politice, istorice, economice, umanitare și de mediu, denotă fragilitatea la care s-a ajuns iar problema care ne frământă pe toți este incertitudinea în privința comportamentului viitor, apropiat ori îndepărtat al coronavirusului. Probabil mulți oameni s-au gândit în acest an la vechiul roman fantasy *The War of the Worlds* al lui Herbert Wells, prin prisma acestor abordări noi cognitiv-psihologice.

Întrebarea *ce facem*? a urmat repede întrebării *cine e de vină*? și a deschis o perspectivă vastă pentru activități organizaționale și pentru cercetare științifică, dar cel mai important lucru este cum Știința va știi să gestioneze Știința! Cercetarea, nu doar biologică și medicală, a căpătat o varietate inedită de aspecte fundamentale, aplicate și tehnologice, devenind catalizator pentru toate disciplinele științifice: bioinginerie, chimie, fizică, inginerie spațială, stiința materialelor, nanotehnologie ori ingineria mediului.

A devenit foarte clar că matematica va fi prezentă în toate formele sale: teoretică, aplicată și computațională, în tehnologii de programare și informație, în inteligența artificială. Algoritmi super rapizi vor fi incluși în arhitectura supercalculatoarelor, pentru o putere în creștere exponențială care să îmbunătățească mult penetrarea tuturor științelor prin realizări care se impun momentului incert în care ne aflăm. În curând vom avea soluții tehnice neașteptate, metodologii noi științifice și organizaționale, noi abordări cognitiv-psihologice care vor schimba radical formele de comunicare, așa cum au făcut-o în timp telefonia, internetul și telefonul mobil.

O consecință a pandemiei, necesar a fi combătută prin metode științifice potrivite, este criza economiilor mondiale și naționale. Există răspunsuri, sau intenții de răspuns la noile provocările globale în filosofie, sociologie, etică și moralitate. Există și întrebarea nerostită: succesul în căutarea adevăratei căii va atinge granițele Utopia sau granițele Distopia? Cum se spune adeseori: rămâne de văzut.

Ec. Elena Banea

Editorial

Time has its own course

After the Second World War, the Volkswagen plant, which was under British control and on the verge of bankruptcy, was going through a difficult period, so its recovery was absolutely necessary. A potential buyer was Ford himself, who came to Germany to see what it was to be seen. Coming across the famous Beetle car, Ford decided not to buy the factory: *It is the most ridiculous car I have ever seen; Beetle will never be successful on the market!*

But a certain character of Jewish origin, the image creator William Bernbach, a visionary master of the Think *Small* and *Lemon* advertising campaigns, made Beetle one of the most famous and best-sold cars in the world, and Volkswagen gained notoriety by launching small cars class at low prices ahead of other competing manufacturers.

This episode was a concrete example of how mankind learned that searching for ways out of the great crises leads to major progress. In the case of the 1929-1933 crisis, major technological performances were reached in engineering, civil and military aviation, in highly intricate constructions or the energy industry, and later on, under the pressure of the systemic crisis during 1971-1975, the technological era began: microelectronics, computer technology, the internet, and mobile communications. Obviously, the nature of an economic crisis is always reflected in the great cycles of the economy.

By the beginning of 2020, mankind was to experience impressive development through huge scientific and technological advances. Scientists have discovered the most subtle secrets of the universe, highly performing digital technologies, and artificial intelligence; they introduced the digital economy, the robotics, services, and items trade on the Internet, as well as unlimited and fast digital connections. For the next decades, scientists have considered a new technological era, which includes infinite energy, miraculous new materials, and eternal youth.

Futuristic stadiums, unimaginable concert halls, luxury hotels, fashionable resorts, restaurants, and mass tourism have been built, all of which illustrating an obvious well-being and a type of accessibility of all these spoiling stuff. Mankind has stepped into the realm of euphoria without realizing it, moreover: it has forgotten! History lessons have been forgotten! Pandemics have been forgotten!

Now, the corona virus pandemic has hit us all, and the *World* has suddenly changed and it will never return to the old state of affairs, with all that it supposed until recently, as far as the approach to material and spiritual values is concerned. The global debates on philosophical, political, historical, economic, humanitarian and environmental issues denote the fragility that has been reached, and the problem that worries us all is the uncertainty about the future evolution of the corona virus pandemic, both on a short and a long term perspective. Many people may have thought this year about Herbert Wells' old fantasy novel *The War of the Worlds* in terms of these new cognitive-psychological approaches.

The question of *what do we do*? quickly followed the question of *who is to blame*? And, thus, it opened a vast perspective for organizational activities and scientific research, but the most important thing is how Science will know how to manage Science! Research, not only biological and medical as such, has diversified in a unique variety of fundamental, applied and technological aspects, becoming a catalyst for all scientific disciplines: bioengineering, chemistry, physics, space engineering, materials science, nanotechnology or environmental engineering.

It has become very clear that mathematics, in all its forms, will be present (theoretical, applied and computational) in programming and information technologies or in artificial intelligence. Super fast algorithms will be included in the architecture of supercomputers, for an exponentially increasing power that will greatly improve the inoculation of all sciences by achievements that are asked for in the uncertain times we are living today. Not before long, we will have discovered unexpected technical solutions, new scientific and organizational methodologies, new cognitive-psychological approaches that will radically change the means of communication, the same way as telephony, the internet and the mobile phone have done over time.

One consequence of this pandemic, which needs to be overcome through appropriate scientific methods, is the crisis of world and national economies. There are answers to or intentions to respond to new global challenges on philosophical, sociological, ethical and moral levels. There is also the unspoken question: will success in the search for the true path reach the borders of Utopia or of Dystopia? As they often say: we shall see about that.

Ec. Elena Banea

DRAG BASED WIND TURBINE VORTICITY CONTOURS EVOLUTION ASSESSMENT

Ioana Octavia BUCUR[1], Ion MALAEL[1]

ABSTRACT: In recent years, interest regarding green sources of energy has increased due to climate changes and higher levels of pollution. Wind energy represents a reliable source of energy, being produced by wind turbines. They convert currents of air into kinetic energy, generating electric or mechanical energy. Vertical axis wind turbines can be classified by the way the forces are generated on the blades as follows: lift-based (Darrieus) or drag-based (Savonius). Darrieus configurations have better efficiency compared to Savonius, but their starting torque is very low, so an additional power source is required for start-up. In this paper the commercial ANSYS software is employed for the CFD analysis of two Savonius geometries, the classic configuration and a modified one, in order to evaluate their power and moment coefficients at different tip speed ratio values. Furthermore, the vorticity contours for the discussed configurations are provided and compared at different blade positions, in order to investigate how blade shape can influence vortices evolution. The study concludes that the proposed geometry for the Savonius wind turbine is more efficient than the classic one. The work presented in this research represents a firm baseline for further development and optimization of the studied type of wind turbine by analysing the vorticity contours evolution and their impact on the overall efficiency of the turbine.

KEYWORDS: Savonius, vorticity, CFD, power coefficient, torque coefficient

NOMENCLATURE

CFD - Computational Fluid Dynamics
C_p – power coefficient
C_T – torque coefficient
HAWT – Horizontal Axis Wind Turbine
SST – Shear Stress Transport

URANS – Unsteady Reynolds-Averaged Navier-Stokes
VAWT - Vertical Axis Wind Turbine
V_∞ - wind velocity
λ – tip speed ratio

1. INTRODUCTION

The need for renewable eco-friendly energy sources has become more and more urgent in recent years as the level of pollution has increased and measures to reduce it are in need. To this attempt, the Renewable Energy Directive implies that the European Union must achieve a target of at least 32% renewable energy of the total global energy demand by the year 2030 [1]. An important source of renewable energy is represented by wind energy and in order to meet the target imposed by the Renewable Energy Directive many countries in the EU have developed wind farms [2]. Wind turbines are divided into two large categories: horizontal and vertical. Horizontal axis wind turbines (HAWTs) are especially suited for open field or offshore areas, as well as high hills, where turbulences are lower compared to urban areas and wind speeds are higher [3]. In cities or their vicinities, vertical axis wind turbines (VAWTs) are more efficient than HAWTs due to their omnidirectionality, the fact that they can work in turbulent flows and at low wind speeds [4]. Vertical axis wind turbines can also be divided into two major categories, namely Savonius and Darrieus. Savonius wind turbines are suited for applications that do not require a high amount of power and often include water pumping or small-scale consumers, such as households, farms or enterprises, including private or public institutions [5].

---

[1] Romanian Research and Development Institute for Gas Turbines COMOTI, Bucharest, Romania

Giving the advantages of the Savonius geometry and its promising possibilities of optimization, as the configuration of the rotor allows the implementation of various alternative geometries, many researchers focused their attention on Savonius wind turbines [6]. As a result, current literature provides insightful information regarding CFD analysis of improved configurations, in order to enhance performances, for the discussed type of VAWT [7]. In paper [8], three different designs are numerically simulated using ANSYS CFX. The authors compare the classical Savonius geometry with a Bach-type Savonius and an Elliptical Savonius, concluding that the most efficient geometry in their study was the Bach-type one, as it surpassed the other two in terms of power coefficient. They also highlight the need of applying a transition model for such analysis, otherwise the torque might be over predicted slightly. Wenehenubun et al. [9] study the impact of blade number on the overall performances of a Savonius wind turbine. Their article presents the analyse of three geometries, with two, three and four blades. Depending on the wind's velocity, the research concludes that each configuration presents both advantages and disadvantages. For example, the three bladed model has better performances for tip speed ratios above 0.4, compared with the four bladed geometry, for which the power coefficient decreases as abruptly as it increases, concluding that this geometry is only efficient for tip speed ratios below the value of 0.4. Analysing their results, the most stable model with respect to wind velocity fluctuations is the two-blade model. Regarding the blade shape of a Savonius wind turbine, several alternatives for the classical blade have been investigated in order to assess better performances. In paper [10] a novel type of blade shape that consists of a combination between the classical and elliptical one is investigated using Fluent. The novel blade design behaves better than the two baselines and the authors further on compare a two and three blades Savonius model, concluding that the two blades wind turbine is more efficient, whereas for the three bladed model the power coefficient is reduced by 17.2%. For the optimization of the classic Savonius wind turbine the study of the vorticity magnitude field represents an important aspect to be considered, as turbulent flows imply the creation and separation of vortices, which have a direct impact on blade efficiency. The vorticity magnitude field around a classical Savonius VAWT is studied in paper [11].

In this paper, the emphasis will be on the two-bladed Savonius configuration and its global performances will be studied by means of CFD analysis. Two different geometries will be investigated using ANSYS Fluent software and their global performances will be compared.

2. METHODOLOGY AND CFD SETUP

In this study a classical two-bladed rotor Savonius wind turbine is slightly optimized by modifying its blade shape in order to enhance its overall performances. The classical geometry consists of two half cylinders disposed with a gap of 0.2m from each other. The modified investigated geometry is provided with a linear sector in the overlapping zone, in an attempt to positively influence the flow inside the rotor in that area. An unsteady 2D analysis of the flow around both turbine geometries is carried out using the mesh motion model in ANSYS Fluent, for tip speed ratios varying from 0.4 and up to 1.6 (by increasing the value with 0.2 gradually), at a wind velocity of 11 m/s. A total number of seven cases for each geometry were studied in order to generate the power and torque coefficients variation with tip speed ratio. For the numerical simulations, the computational domain was divided into two main regions: the rotor and the stator domain, with an interface between them. The geometrical characteristics of the Savonius wind turbine are presented in table 1 and the boundary conditions for the numerical simulations in table 2.

Table 1. Geometrical parameters

Parameter	Unit	Value
Diameter	[m]	2.5
Height	[m]	3.75
Number of blades	-	2
Gap	[m]	0.2
Tip Speed Ratio (λ)	-	0.4-1.6
Angular velocity	[rad/s]	3.52-14.08
Wind velocity (V_∞)	[m/s]	11
Rotor domain diameter	[m]	3.4
Stator domain diameter	[m]	16

Table 2. Boundary Conditions

Boundary	Condition
Blades	Wall
Shaft	Wall
Rotor	Mesh motion
Stator	Stationary
Interface	Rotor-stator interface

The grids for both geometries were generated using ANSYS Meshing, Quadrilateral Dominant method. Near the blade an inflation with 30 layers was inserted for better accuracy. The assumed value for y+ was 1, in order to resolve possible problems in the vicinity of the boundary layer. The grids for the studied geometries are illustrated in figure 1 and 2, respectively.
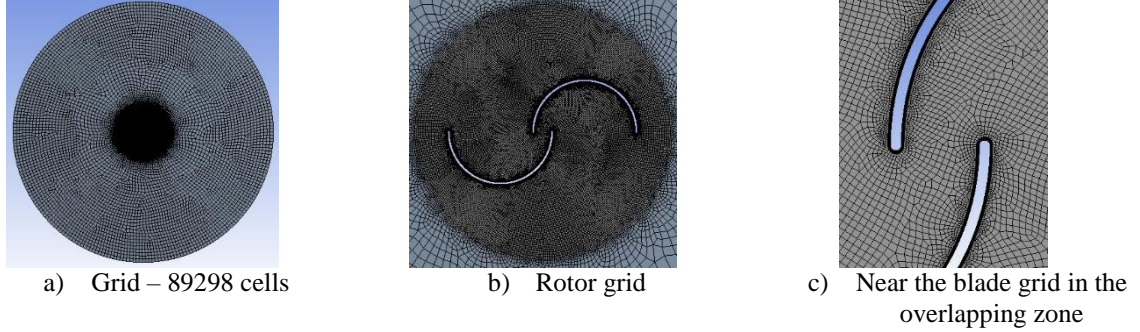

a)   Grid – 89298 cells   b)   Rotor grid   c)   Near the blade grid in the overlapping zone

Fig. 1 Grid for the classical Savonius geometry

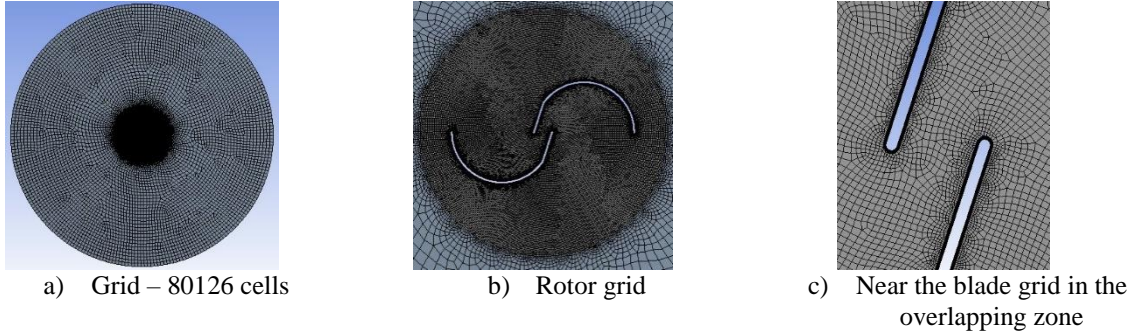a)   Grid – 80126 cells   b)   Rotor grid   c)   Near the blade grid in the overlapping zone

Fig. 2 Grid for the modified Savonius geometry

In ANSYS Fluent the URANS k-ω SST transition turbulence model was employed in order to investigate the flow around the two configurations. This model was considered the most appropriate one for obtaining accurate results, as it combines the standard k-ω model (used in the near-wall regions) with the standard k-ε model (which is used away from the wall) [12]. The SIMPLE method with 2nd order discretization schemes was used. Each of the cases was studied for seven complete revolutions of the turbine, resulting a total of 2520 iterations per case, meaning that there were 360 iterations per revolution. The time step was evaluated individually for each case in accordance with the rotational speed resulted for each tip speed ratio value.

3.   RESULTS

In this section, the results of the numerical CFD simulations for both cases are compared, with emphasis on the torque and power coefficient, and the vorticity magnitude fields are assessed for different tip speed ratios for both configurations. The torque coefficient was set as an output result from the numerical simulations, whereas the power coefficient was evaluated in each case as a function of tip speed ratio with the following formula:

$$C_P = C_T \lambda \tag{1}$$

The seven studied cases were used to evaluate the power coefficient variation with the tip speed ratio, as plotted in figure 3. The classic Savonius model is more efficient for tip speed ratio values below 1, whereas when this parameter surpasses the value of 1, the modified proposed geometry exceeds the efficiency of the classic configuration. However, for both geometries the maximum value of the power coefficient is obtained at a tip speed ratio value of 1.2.
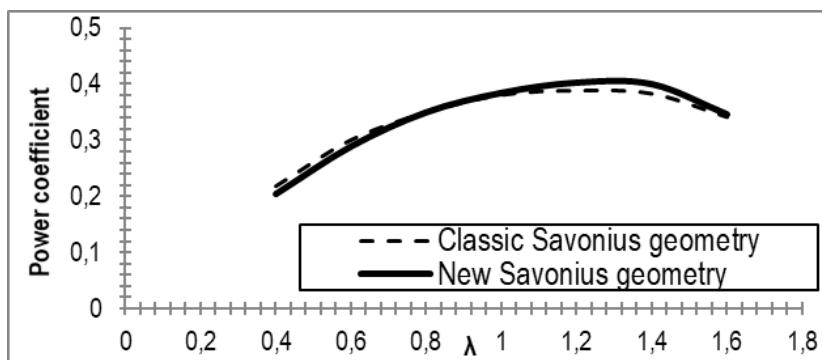
Fig. 3 Power coefficient variation with tip speed ratio

In figure 4 and 5, the torque coefficient variation for a complete rotation is illustrated for both geometries. In order to not load the graph and make it illegible, the variation was plotted for only four cases (TSR values 0.4, 0.8, 1.2 and 1.6). The mean value for the torque coefficient at a tip speed ratio of 1.2 is 0.324 for the classical Savonius geometry and 0.335 for the modified one.
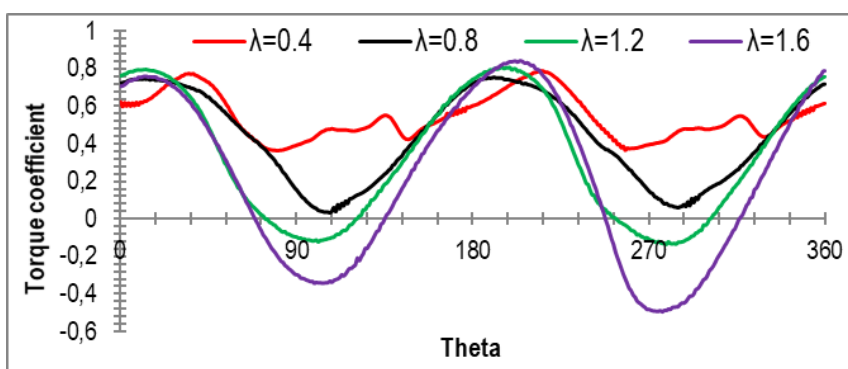

Fig. 4 Torque coefficient variation for the classical Savonius geometry
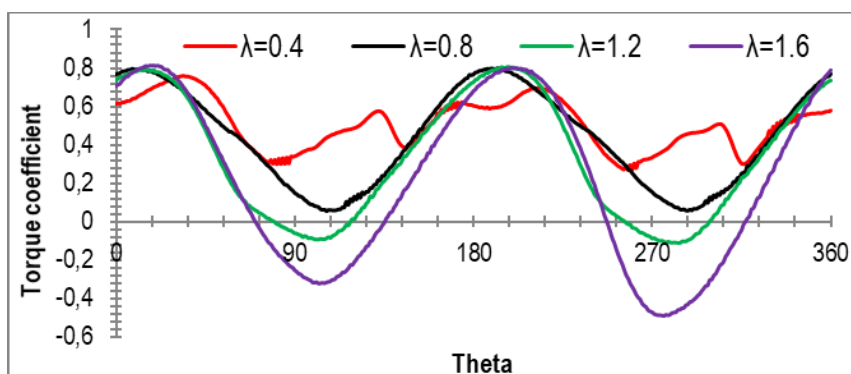

Fig. 5 Torque coefficient variation for the modified Savonius geometry

In the following figures, the vorticity magnitude field around the two investigated Savonius geometries will be presented, at different blade positions, for two cases: case 1 – at a tip speed ratio value of 0.4, case 2 – at a tip speed ratio value of 1.2 (the maximum value of the power coefficient). In Fig. 6 the legend for Figs. 7-8 is illustrated separately.
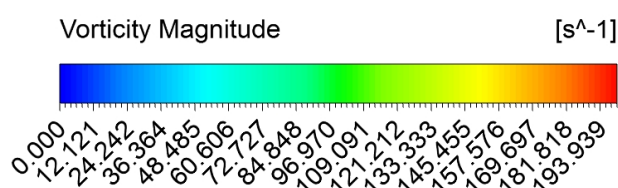

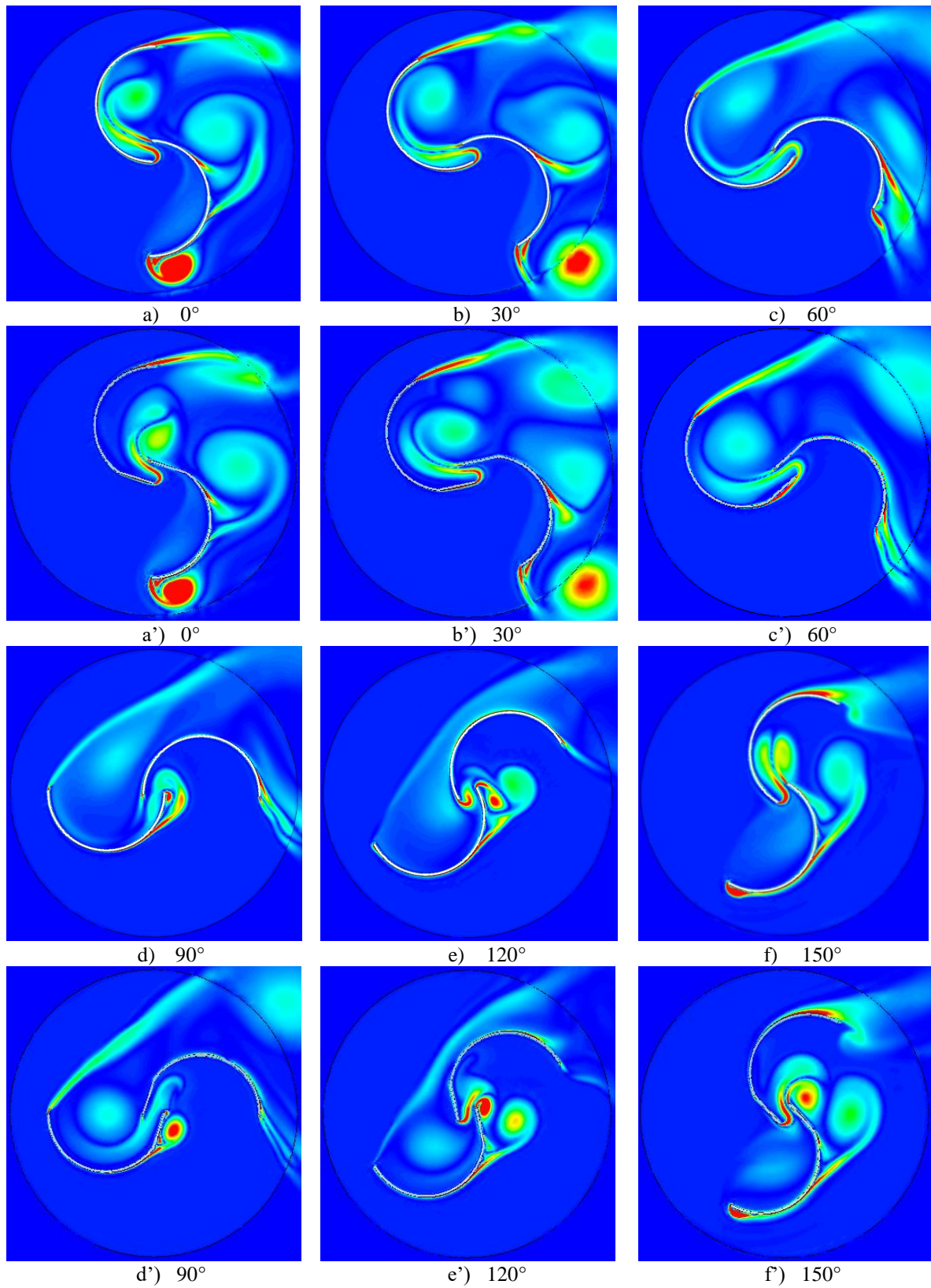**Fig. 6 Legend for the vorticity magnitude field**

Fig. 7 Vorticity magnitude for the classic Savonius geometry (a, b, c, d, e, f) and the modified one (a', b', c', d', f'), at V_∞=11m/s and λ=0.4
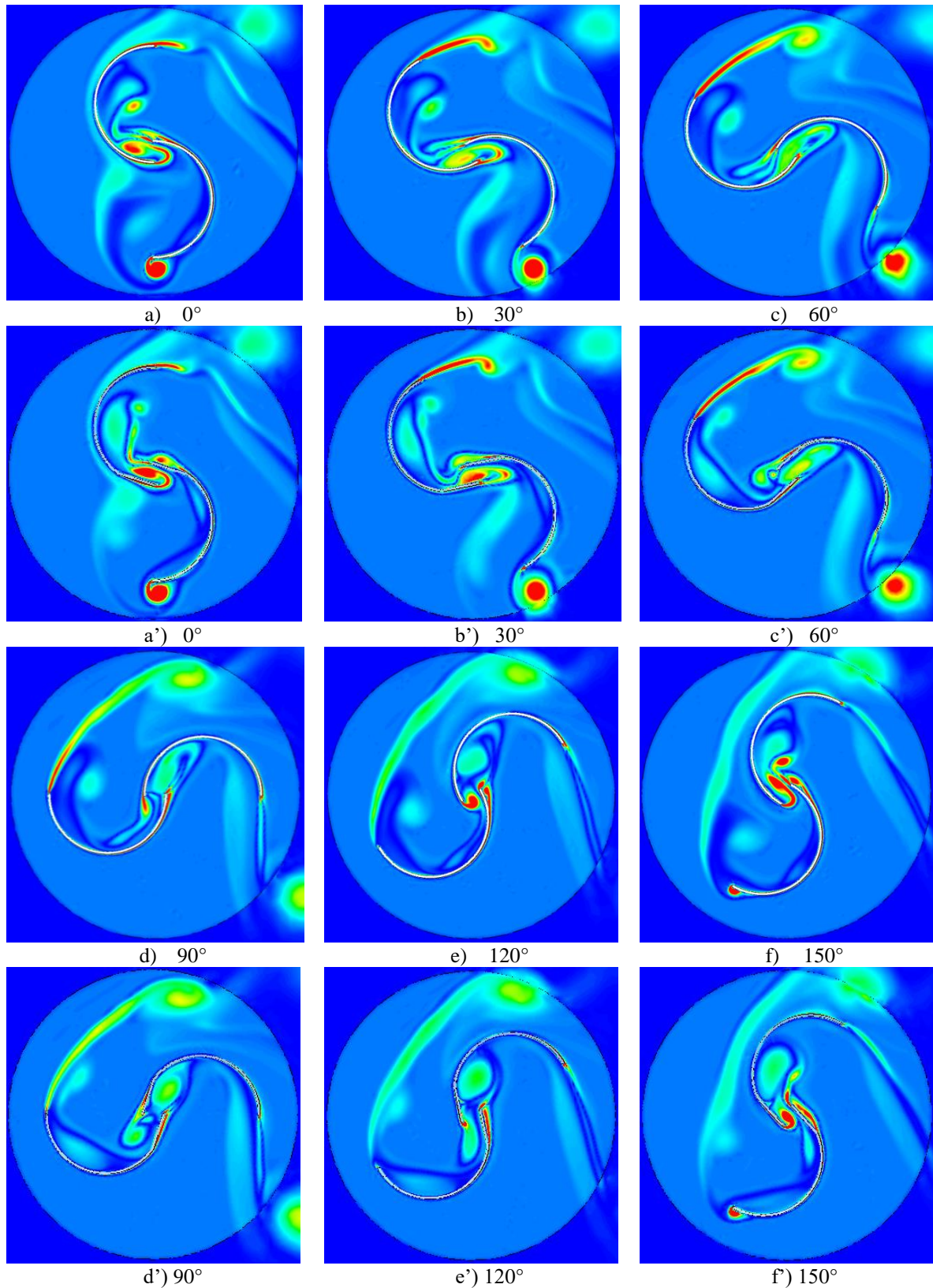
a) 0°   b) 30°   c) 60°

a') 0°   b') 30°   c') 60°

d) 90°   e) 120°   f) 150°

d') 90°   e') 120°   f') 150°

Fig. 8 Vorticity magnitude for the classic Savonius geometry (a, b, c, d, e, f) and the modified one (a', b', c', d', f'), at V∞=11m/s and λ=1.2

Comparing the vorticity contours presented in figure 7, at a low tip speed ratio value (0.4 in this case), an increased value for the vorticity magnitude is observed in the overlapping area for the modified geometry.

This aspect is reflected in the lower efficiency values for this one compared to the classical one when functioning at tip speed ratios below 1. On the other hand, when the tip speed ratio exceeds the value of 1, the modified proposed geometry behaves better. Its vorticity magnitude is lower in the overlapping zone compared to the classical Savonius geometry, as pictured in figure 8 for the case of a tip speed ratio value of 1.2. The difference between the vorticity magnitudes in the overlapping area for the two different geometries is most noticeable when comparing Fig. 8 e) with Fig. 8 e') and Fig. 8 f) with Fig. 8 f'), namely at 120° and 150° blade positions. This evolution of the vorticity contours for both investigated geometries is reflected in figure 3, when after a tip speed ratio of 1, the modified Savonius geometry exceeds the classic's one efficiency. Both geometries present the best efficiency for a tip speed ratio value of 1.2, but the linear sector of the proposed geometry, included in the overlapping zone, allows it to provide better performances.

4. CONCLUSIONS

The purpose of this paper was to assess the vorticity contours evolution for a classical Savonius wind turbine geometry and a modified proposed model, in order to investigate how the vorticity magnitude field evolution impacts overall performances. Both power and torque coefficient variations with the tip speed ratio were plotted for the studied configurations. The maximum efficiency in both cases was registered at a value of 1.2 for the tip speed ratio. The power coefficient for the classic Savonius geometry had a maximum value of 0.389, whereas the modified configuration exceeded it, with a maximum power coefficient value of 0.403. By altering the original geometry in the overlapping zone an increase of 1.4% in terms of efficiency was possible. Further studies should concentrate on analysing the optimal length for the linear sector, as well as the optimal angle between it and the axis on which the half cylinders are placed. It is important to specify that the discussed values for the efficiency are for the 2D case, and that the 3D effects of the flow have not been considered in this research.

REFERENCES

[1]. Official Journal of the European Union, June 2009, L 140. DOI: 10.3000/17252555.L_2009.140.eng.
[2]. Walsh C. and Pineda I., 2019, Wind Energy in Europe in 2018 – Trends and statistics, Available at: windeurope.org.
[3]. Johari M. K., Jalil M. A. A. and Shariff M. F. M., 2018, Comparison of horizontal axis wind turbine (HAWT) and vertical axis wind turbine (VAWT), *International Journal of Engineering & Technology*, 7, pp. 74 – 80.
[4]. Njiri J. G. and Soffker D., 2016, State-of-the-art in wind turbine control: Trends and challenges, *Renewable and Sustainable Energy Reviews*, 60, pp. 377 – 393.
[5]. Paraschivoiu I., 2002, *Wind Turbine Design - With Emphasis on Darrieus Concept*, Polytechnic International Press.
[6]. Kothe L. B., Möller S. V. and Petry A. P., 2020, Numerical and experimental study of a helical Savonius wind turbine and a comparison with a two-stage Savonius turbine, *Renewable Energy*, 148, pp. 627 – 638.
[7]. Roy S. and Saha U. K., 2013, Review on the numerical investigations into the design and development of Savonius wind rotors, *Renewable and Sustainable Energy Reviews*, 24, pp. 73 – 83.
[8]. Kacprzak K., Liskiewicz G. and Sobczak K., 2013, Numerical investigation of conventional and modified Savonius wind turbines, *Renewable Energy*, 60, pp. 578 – 585.
[9]. Wenehenunbun F., Saputra A. and Sutanto H., 2015, An Experimental Study on the Performance of Savonius Wind Turbines Related With The Number Of Blades, *Energy Procedia*, 68, pp. 297 – 304.
[10]. Saeed H., Elmekawy A. M. N. and Kassab S., 2019, Numerical study of improving Savonius turbine power coefficient by various blade shapes, *Alexandria Engineering Journal*, 58(2).
[11]. Dumitrescu O., Mălăel I., Drăgan V. and Gherman B., 2016, The renewable energy generated by the Savonius wind turbine used for water extraction, *Recent Advances in Energy, Environment and Financial Science*.
[12]. Rezaeiha A., Montazeri H. and Blocken B., 2019, On the accuracy of turbulence models for CFD simulations of vertical axis wind turbines, *Energy*, 180, pp. 838 – 857.

DIODICITY INVESTIGATION OF TESLA VALVE

Cosmin Petru SUCIU[1], Razvan Edmond NICOARA[1], **Madalin-Constantin DOMBROVSCHI[1], Emilia PRISACARIU[1], Ioana Octavia BUCUR[1]**

ABSTRACT: The Tesla valve is a NMP (no moving parts) component that facilitates the flow in one direction and inhibits the flow in the other direction. This paper studies the diodicity of two different geometries for such a component. Numerical CFD simulations are presented and the results are discussed. 3D printed parts for each geometry have been printed for an experimental campaign. The inlet and outlet pressure are measured for computing the diodicity. The results are post-processed and the geometries compared. A high diodicity Tesla Valve can be used in many applications as an upgrade, given the fact that there are no moving parts that can be damaged by high temperature or stress.

KEYWORDS: fluidic diode, no-moving-parts, valvular conduit, Nikola Tesla.

1. INTRODUCTION

The Tesla valve was named by its inventor (Nikola Tesla) valvular conduit. It is a unidirectional valve with fixed geometry, that allows the fluid to flow in a preferential direction. Nikola Tesla has received a patent for his invention in 1920. Tesla`s invention presents various channels, that are disposed in a way that allows the flow to pass freely in one direction, but when the direction changes, the stream is subject to rapid reversals of direction thus blocking the flow through friction and mass resistance [1]. The specific efficiency of this valvular pipe can be controlled through the number of elements (nodes). This type of valve does not block entirely the flow, but can provide a resistance dependent on direction.
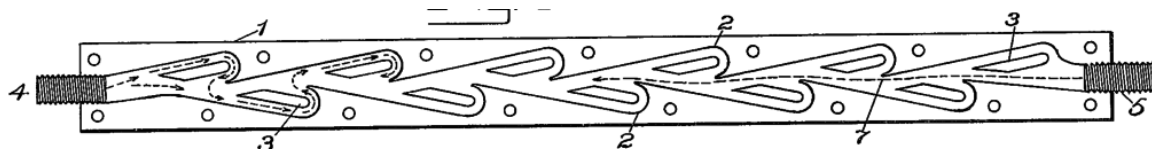

Fig. 1 Tesla Valve [1]

Zhi-jiang et al. [2] conducted a parametric study regarding the usage of the Tesla valve for hydrogen fuel-cell electric vehicles. For such applications, the recharge mileage of vehicles represents an important parameter. In order to develop a highly efficient system, hydrogen storage at high pressures is necessary (35-70 MPa). Furthermore, providing a safe and fast decompression of the hydrogen to a certain pressure is very important. The Tesla valve is a suitable component for the described system, due to its advantages, such as: it induces a large pressure drop for reverse flow, easy manufacture (due to the fact it has no moving parts), high reliability.

Frijns et al. [3] successfully designed a Tesla Valve for pulsating heat pipes. The functionality and diodicity were tested by laminar single-phase modelling and by steady two-phase flow experiments. The valves produced a diodicity which lead to a difference in velocity of 25% for the reverse and forward directions.

Thompson et al. [4] investigated through CFD analysis multiple, identically shaped micro Tesla valves arranged in series. The results obtained showed a clear increase in diodicity for multiple Tesla valves. The study also showed that decreasing the distance between the adjacent Tesla valves provides a boost in diodicity. They also concluded that more Tesla valve are required to maximize diodicity as the Reynolds number increases.

---

[1] Romanian Research and Development Institute for Gas Turbines COMOTI, Bucharest, Romania

Forster et al [5] proposed Tesla valve integration for micro-fluidic applications as a NMP pump. A working prototype was manufactured onto a silicon wafer having the width of about 100μm for experimental investigation. The prototype was named "T45-R". As an outcome, the experimental campaign found an almost linear increase in diodicity with flow rate for low Reynolds numbers (Re < 300).

Most of the research involved in studying and improving Tesla valve efficiency is focused on micro scale fluid applications. This paper aims to study the diodicity mechanism of the original Tesla valve design and compare it to a different design that follows the same principles. The geometries have a hydraulic corresponding diameter of 4mm. Both geometries were numerically analyzed through CFD simulations and the results are presented. Furthermore, for an experimental investigation 3D printed prototypes have been created, in order to measure the static inlet/outlet pressure for both geometries and determine the performance of both designs.

2. CFD analysis

2.1. 3D models, meshing and boundary conditions

The design of the 3D model has been constrained by the overall dimensions of the 3D printer used for the prototypes (150x150x200 mm). The models were created using Solidworks 2017 CAD software. The first step was to generate the fluid domain, that was designed in the shape of a rectangular channel (3x6 mm). The fluid domains are represented in Figure 2. The design from the bottom part follows the same principles as the
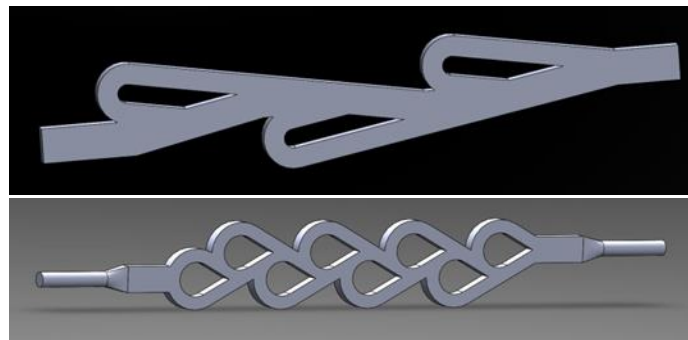

Fig. 2 Fluid domains; Original Tesla Valve (top) [1]; Waterdrop Valve (bottom) [7]

upper model, a series of turns shaped in the form of a waterdrop. Both fluid domains have similar lengths, the only major difference being the number of turns that the fluid flow undergoes in operation.

The mesh is an integral part of the CAE (computer-aided engineering) simulation process. Mesh structure and dimension directly affect the convergence and the speed of the solving process. This being said, because of the limitations regarding the processing power, a 2D analysis is the better approach in order to have a qualitative mesh with relatively a small number of elements.
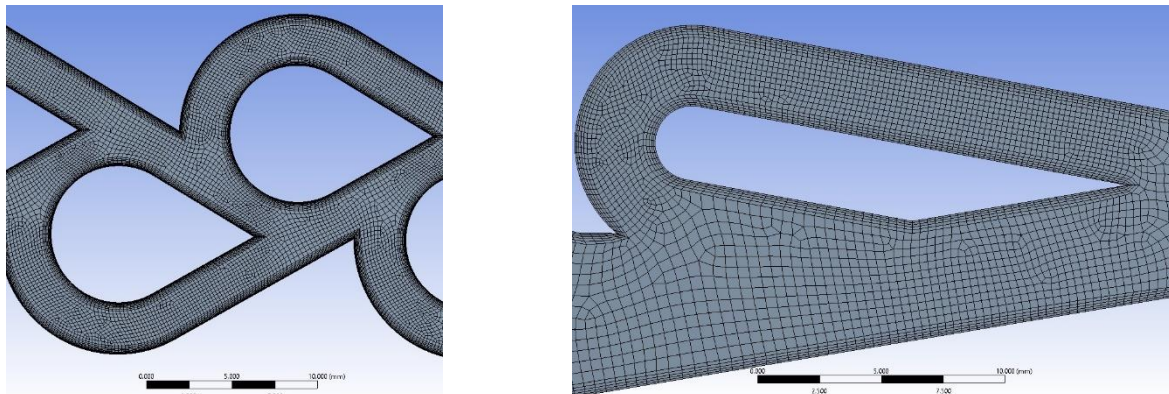

Fig. 3 Fluid domain mesh [7]; Waterdrop design (left) – Original Design (right)

The mesh was created in ANSYS 2020R1(implicit meshing module). The 2D fluid flow domain was extracted and imported in ANSYS for the meshing process. Both geometries have similar mesh characteristics that will enable a correct comparison of the results. Hexahedral elements where chosen with a maximum dimension of 1mm. A minimum number of 15 elements has been imposed between two walls. For capturing the boundary layer properly, wall inflation with a total thickness of 0.5mm has been added, being composed of 10 layers with a growth factor of 1.2 between them. The resulted mesh for both geometries is presented in Figure 3.

2D simulation of a fluid domain can be done using FLUENT solver. The solver considers the domain as a surface on XY plane, but during the solutioning process uses a characteristic length (1m by default) on the Z axis. This is an important aspect because it directly affects the mass flow rate. Both domains were numerically calculated using the same boundary conditions.

The type of solver used is pressure-based. Due to the compressible nature of the flow, the energy equation will also be used. The turbulence model used was k-ω SST (Shear Stress Transport). This is a version of the standard k-ω model. The chosen turbulence model is a combination between the original Wilcox k-ω model, which is used for the flow near the wall, and the standard k-ε model, used away from the walls through a specific function [5]. This type of model is usually used when the boundary layer has an important effect. Taking into consideration the reduced dimensions of the fluid domain, the boundary layer influence can be significant. Given the chosen turbulence model k-ω SST, in order to resolve any possible problems in the vicinity of the boundary layer the value assumed for y+ was 1 [6]. Because of the limitations imposed by computing power, for the conducted CFD analysis the y+ evolution for high flow velocities was not monitored.

Table 1. Boundary conditions

No.	Boundary	Condition	Value	Observation
1	Inlet	Pressure-inlet	300000 Pa	Reference Pressure 0 atm
2	Outlet	Mass flow outlet	0.5 kg/s	-
3	Walls	Adiabatic Wall	-	-

The convergence criterion is a universal concept in numerical analysis. If the realised model contains non-linearities, it cannot be solved directly, so the solution needs to be found iteratively. Although it is not possible to find the exact solution, a sufficiently close approximation can be presented. The convergence criterion defines the accuracy of the final results. This analysis aims for a convergence criterion of 1e-0.4.

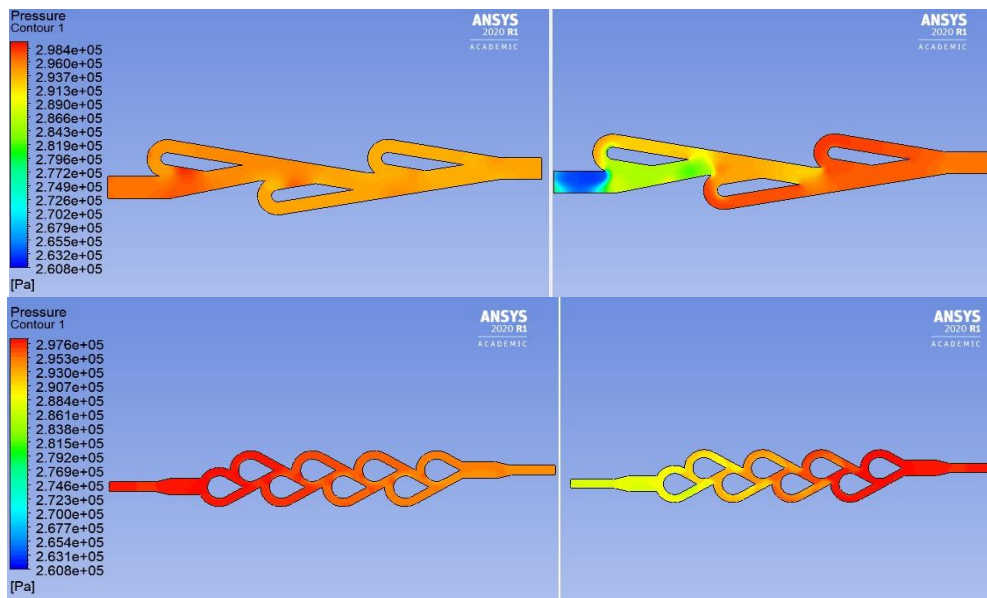### 2.2. Numerical results

Static pressure field

Fig. 4 Original Tesla design (top); Waterdrop design (bottom) [7]

The static pressure field is represented in Fig. 4 for both directions of the flow. The upper part represents the original design, whereas the bottom part illustrates the waterdrop design. For a closer look, on the left side can be observed that the static pressure is almost equal for inlet and outlet. This means the flow is not greatly disturbed and passes freely through the valve. The original design manages to keep the pressure drop lower than the waterdrop design. This is mostly because it induces fewer changes of direction for the working fluid. After inlet, the fluid splits in 2 different channels, being subjected to a higher change in direction than the one seen in the original Tesla design.

Stagnation Pressure Field

Figure 5 represents the stagnation pressure field for both geometries and both flow directions. The difference between Figure 4 and Figure 5 is given by the dynamic component of the stagnation pressure. When comparing both geometries on the normal flow direction, it is clear why there is a bigger pressure drop for the waterdrop design. The main property of a flow going through a direction change is the presence of the radial
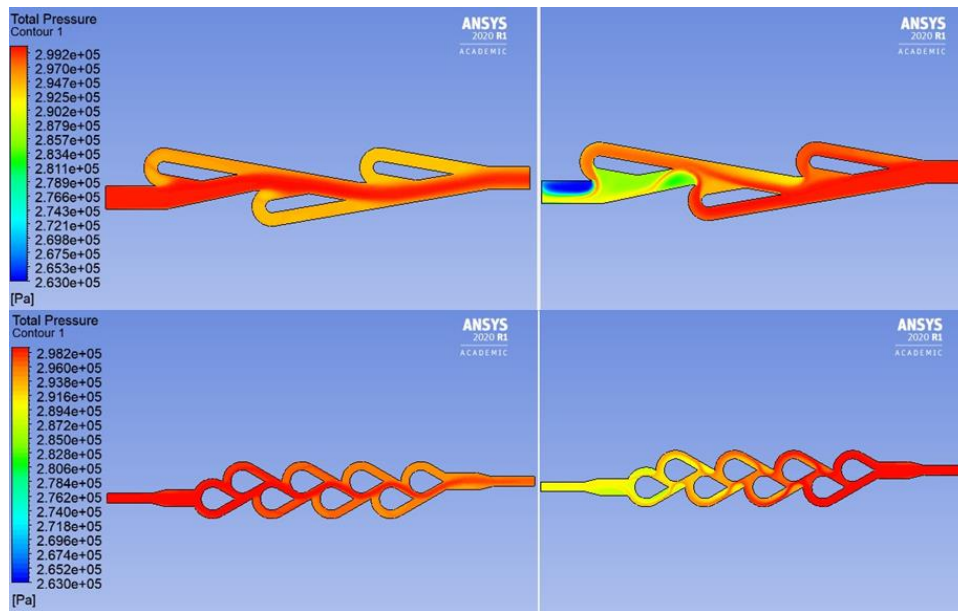

Fig. 5 Stagnation pressure field; Original design (top), Waterdrop design (bottom) [7]

pressure gradient given by the centrifugal force acting on the fluid. The drop in pressure found in this type of flow is caused by the friction forces and the rapid impulse change resulted from the change in flow direction. Both these factors are dependent on the curvature angle, curvature ratio and Reynolds number. The stagnation pressure losses can be expressed by summing the two components: a) the friction component existent in a flow through a straight channel of the same equivalent length, which is dependent mainly on Reynolds number and the rugosity of the channels; b) the component expressed by the losses given by the change in flow direction, which is dependent mainly on the curvature ratio (median radius of curvature/diameter of the channels) and the angle of curvature [8]. The pressure loss for the change in direction can be computed as follows:

$$\Delta P = \frac{1}{2} f_s \rho u^2 \frac{\pi R_b}{D} \frac{\theta}{180°} + \frac{1}{2} k_b \rho u^2 \qquad \textbf{(1)}$$

where,

F_s – Moody friction factor	k_b – curvature losses coefficient	R_b – medium radius
ρ – density	u – average velocity of the flow	D – diameter
θ – angle		

After each loop, one can observe the appearance of a low-pressure zone (vortex). Looking at the Figure 5, we can observe a bounded vortex hitting the outlet of the original geometry for reverse flow. Because the vortex is located close to the boundary of the domain, the solver has created artificial walls for impeding the inflow of air inside the domain. This can be overcome by elongating the outlet duct.

3. EXPERIMENTAL CAMPAIGN

3.1. Experimental models and test stand

The prototypes where modelled in Solidworks based on the fluid domains studied. The valves are designed in two separate parts, one containing the flow channel and the other serving as an instrumentation cover. For this study, two pressure ports suffice for the evaluation of the diodicity of the valve, but for future research, a new cover can be made with other configurations for pressure/temperature measurement. The valves were 3D printed with transparent resin on Form 2 printer from Formlabs [9]. The valves were then cleaned with alcohol for removing any excess resin that could have remained inside the flow channel after the printing process. Both valves were then introduced for a thermal (60 °C) and UV treatment for one hour.
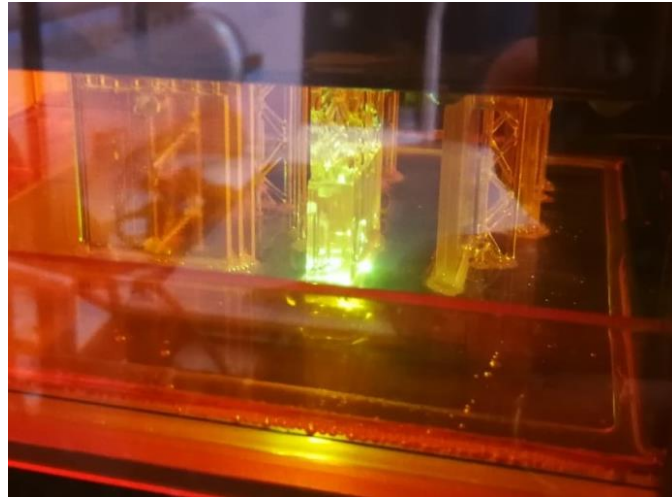

Fig. 6 Valves during the printing process (top);

The test stand is represented in Figure 7. The air supply was ensured by a compressor. Because of the small dimensions of the compressor another reservoir was filled with compressed air at 15 bars. The control vane was then gradually opened until the desired inlet pressure was achieved. The pressure was measured with DSA3217 pressure transducer. Data acquisition was realised using an in-house LabVIEW program.
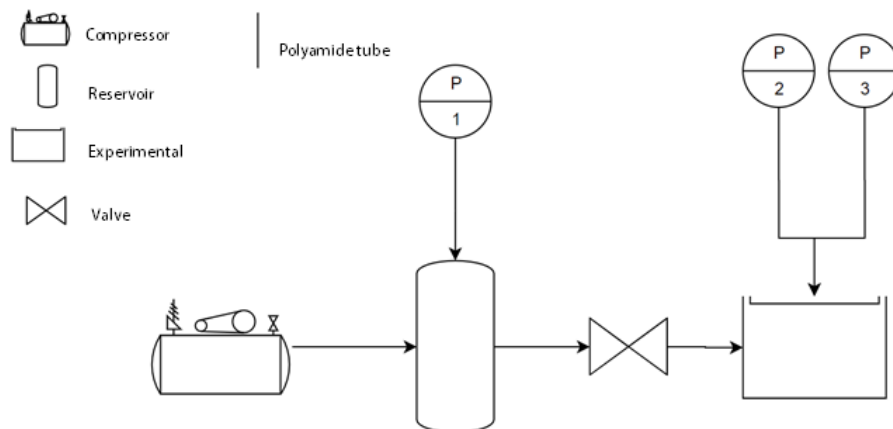

Fig. 7 Test stand diagram [7]

3.2. Experimental results

After the experimental data was collected, the pressure values have been mediated over a period of 10 seconds. The processed data can be seen in Table 2. All pressures are measured relative to atmospheric pressure. The test names are formatted as follows: 1.X refers to reverse flow, whereas 2.X refers to forward flow; "O" stands for original design and "W" stands for waterdrop design; X.1-4 refers to different inlet pressures.

Table 2. Experimental data

| Test name	Total pressure (bar)	P2 (bar)	P3 (bar)	Velocity (m/s)	Reynolds number	Pressure drop	Pressure drop %	Diodicity $[\frac{\Delta P_{reverse}}{\Delta P_{forward}}]$
Tesla O1.2	1.2825	0.3025	0.4357	321	109160	0.1332	30.5655	5.4250
Tesla O2.2	1.2675	0.3699	0.3454	329	111935	0.0245	6.6365	
Tesla O1.2	1.7865	0.5011	0.6747	330	138064	0.1736	25.7308	5.5606
Tesla O2.2	1.7716	0.5846	0.5534	339	115357	0.0312	5.3402	
Tesla O1.3	2.0794	0.6426	0.8063	334	153146	0.1637	20.3078	5.1825
Tesla O2.3	2.0724	0.7235	0.6919	342	156703	0.0316	4.3672	
Tesla O1.4	2.5500	0.8586	1.0242	340	177866	0.1657	16.1752	5.0854
Tesla O2.4	2.5293	0.9530	0.9204	344	180229	0.0326	3.4184	
Tesla W1.2	1.2980	0.2975	0.5543	303	99104	0.2569	46.3368	1.2984
Tesla W2.2	1.3096	0.5554	0.3576	305	107562	0.1978	35.6158	
Tesla W1.2	1.6598	0.4269	0.7426	310	121469	0.3157	42.5105	1.2986
Tesla W2.2	1.6977	0.7635	0.5204	309	129318	0.2431	31.8397	
Tesla W1.3	2.0920	0.5971	0.9639	315	148219	0.3668	38.0519	1.2944
Tesla W2.3	2.0949	0.9879	0.7046	316	144318	0.2833	28.6816	
Tesla W1.4	2.5385	0.7742	1.0881	332	173707	0.3138	28.8416	1.0342
Tesla W2.4	2.5275	1.1936	0.8902	323	168513	0.3034	25.4216	
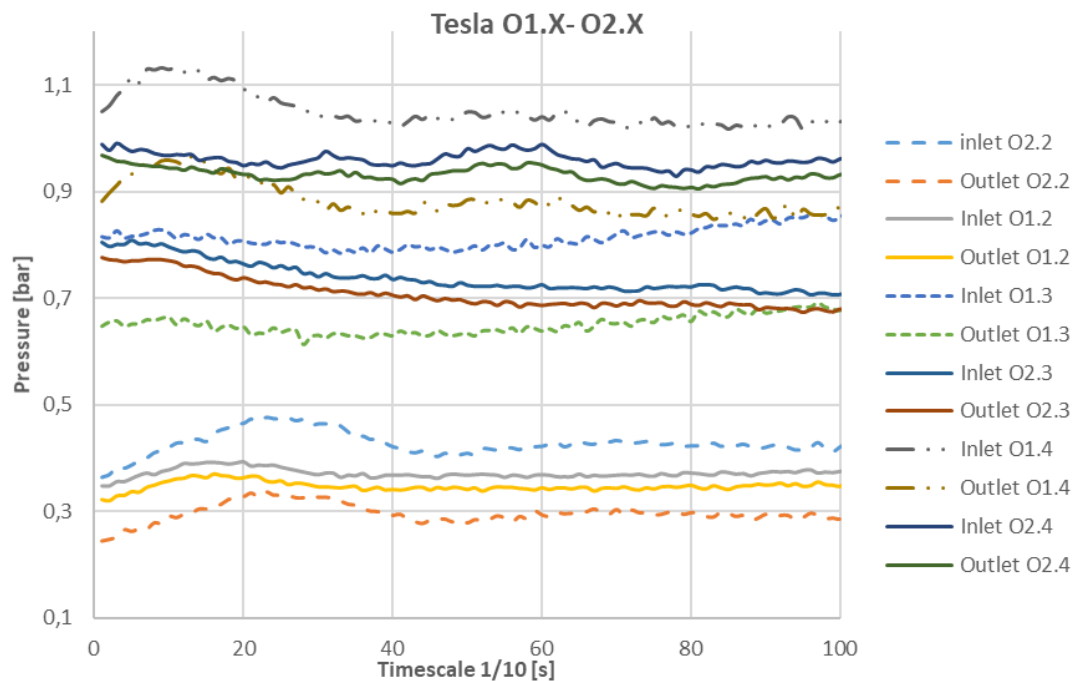
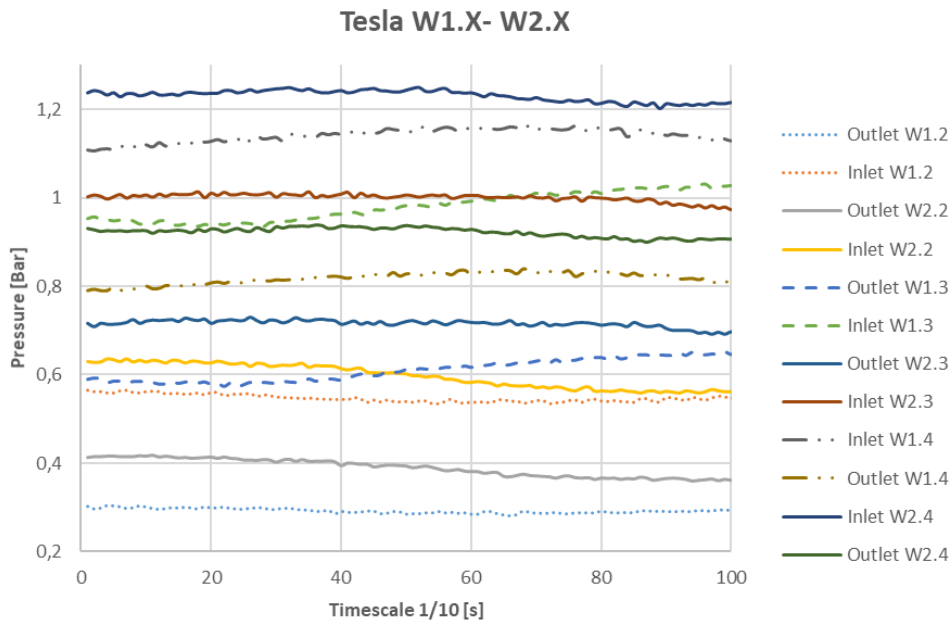**Fig. 8 Original Tesla design pressure evolution**

Fig. 9 Water drop design pressure evolution

The results obtained show a clear difference between the two geometries studied. The original design has performed much better than the waterdrop design. The pressure evolution graphs, Figures 8 and 9, show a clear difference in valves efficiency. While for the original design, there is a big difference in pressure drop between the forward flow and reverse flow, the waterdrop design has almost the same pressure drop for each direction of the flow. This means that the original design has a higher diodicity than the waterdrop design. Table 2 contains the results mediated over a time period over which the pressure was constant. The diodicity difference is quite big, the original design having a diodicity almost five times bigger than the waterdrop design. This is mostly due to the minimum pressure drop provided for the forward flow. As inlet pressure increases, there is an observable increase in diodicity until it starts to decrease. This phenomenon can be related to the Reynolds number achieved for the flow. Further investigation related to the influence of Reynolds number in Tesla Valve diodicity must be made.

The biggest pressure drops obtained for the original design is about 30%. This drop was achieved using only 3 loops. In order to achieve a higher pressure drop, depending on the needs of the application, more loops can be integrated. The loops do not interfere much with the flow in the forward direction, therefore the diodicity is quite big. The waterdrop design achieved a higher pressure drop for reverse flow, 45%, due to the larger number of geometry loops. However, the small diodicity obtained shows a higher influence of the loops during the forward flow.

4. CONCLUSIONS AND FUTURE WORK

This paper studies the diodicity of two different Tesla valve geometries when the hydraulic diameter is 4mm. The original design has been reproduced from the Tesla patent [1], whereas the waterdrop design has been modelled using the same principles but with different channel geometry. A numerical analysis of both designs was presented, and the flow through each of the geometries was characterised. The CFD analysis show that the original design performs much better than the waterdrop design, keeping the influence of the geometry minimal for forward flow.

Two prototypes were 3D printed and tested at different inlet pressures. The data obtained was processed and presented in Table 2. The results from the experimental phase are consistent with the CFD results. The diodicity obtained for the original design was almost five times higher. The data shows a big potential for this type of NMP valve. Further studies will be conducted, with emphasis on the analysis of the influence of the Reynolds number has on diodicity.

Furthermore, the original design achieved a high diodicity with only 3 loops. Future research will be made in order to determine the influence of the number of loops on valve efficiency, evaluating also the maximum diodicity such a valve can provide.

ACKNOWLEDGEMENT

REFERENCES

[1] https://patents.google.com/patent/US1329559A/en ; Nikola Tesla. Valvular conduit, 1920. U.S. Patent No. 1,329,559

[2] Zhi-jiang J., Zhi-xin G., Min-rui C., Jin-yuan Q. (2018); Parametric study on Tesla valve with reverse flow for hydrogen decompression; *International Journal of Hydrogen Energy;* XXX 1-9

[3] Vries, S.F. & Florea, Daniel & Homburg, F.G.A. & Frijns, Arjan. (2017). Design and operation of a Tesla-type valve for pulsating heat pipes. *International Journal of Heat and Mass Transfer*. 105. 1-11. 10.1016/j.ijheatmasstransfer.2016.09.062.

[4] Thompson, Scott & Paudel, Basil & Jamal, Tausif & Walters, D.. (2014). Numerical Investigation of Multi-Staged Tesla Valves. *Journal of Fluids Engineering*. 136. 081102. 10.1115/1.4026620.

[5] F. R. Menter, "Zonal Two Equation k-w Turbulence Models for Aerodynamic Flows," AIAA Paper #93-2906, 24th Fluid Dynamics Conference, July 1993;

[6]. F. R. Menter, M. Kuntz, R. Langtry (2003); Ten Years of Industrial Experience with the SST Turbulence Model; *Turbulence, Heat and Mass Transfer (4)*.

[7] C.P. Suciu; 2020; "Proiectarea unui pulsoreactor cu valva Tesla"; Masters thesis, University Politehnica of Bucharest; Faculty of Aerospace Engineering.

[8] Rowe, M. (1970) Measurement and computation of flow in pipe bends, J. Fluid Mech. DOI: 10.1017/S0022112070002732

[9] Technical specifications Form 2; https://formlabs.com/3d-printers/form-3/tech-specs/; accesed on 12.11.2020

STRESS ANALYSIS OF A HIGH LOAD COMPRESSOR FOR AN ADVANCED MICROTURBINE POWERPLANT

Andreea ALCEA[1], Valeriu DRAGAN[1], Oana DUMITRESCU[1], Ramona STANCIUC[1]

ABSTRACT: The aim of the current paper is to find an optimal configuration for the centrifugal compressor impeller of a micro gas turbine. The tridimensional modelling of the compressor's impeller was achieved using a CAD software optimized for high-speed machinery. As work method, the finite element algorithm implemented into the NASTRAN solver was used to study and analyse the rotor. For pre and post processing of the model the PATRAN software was used. The finite element analysis of the impeller, which will be used to equip a small multifunctional aircraft, has been made in multiple steps in order to optimise the geometry. A material with compatible characteristics and properties to the rotor's use case, AL 2618 was suited given it offered a satisfactory safety factor.

KEYWORDS: micro gas turbine, centrifugal compressor, impeller, FEA, turbomachiney

1. INTRODUCTION

Gas turbines play one of the most important roles in modern power plants. During the last few decades, several attempts have been made to develop microturbines with efficiency levels close to those of larger gas turbines [1]. A large number of geometrical and mechanical restrictions limit the efficiency of micro turbomachinery. Centrifugal compressors are typically used because of the high pressure ratio they deliver per stage [2]. The optimization between aerodynamic performance and structural reliability is critical in order to provide the maximal potential of the compressor performance [3]. Sagar and Kyle [4] discussed that it is essential to provide a suitable thickness of blade such that it can withstand the high centrifugal stress. The magnitude and location of the deformations are important both to design and to its operation since it can cause contact with the compressor housing [4]. Kim et al [5] described that the impeller deformation in operation due to the centrifugal force, aerodynamic pressure and thermal loads change the tip clearance. The failure modes include abrasion, erosion, stress fatigue and others [6]. The microturbine powerplant is developed for a thrust of 80 daN and estimated rotational speed of 45,000 rpm. This is intended to equip a small multifunctional aircraft.

In this paper, a centrifugal compressor impeller is studied. The iterative elaboration of the geometries was carried out on the basis of specific theories of the strength of materials regarding the state of stress in rotating disks, as well as the Von Mises stress distribution, given that this parameter is one of the main criteria used to evaluate the elasto-plastic behaviour of metals. [7]

2. NUMERICAL SIMULATION

2.1 Geometry

For the initial version, a classic flat disk solution was chosen. The model took into consideration the effects of the rotation. The main load consists of the the inertial forces caused by the rotational movement of the impeller.

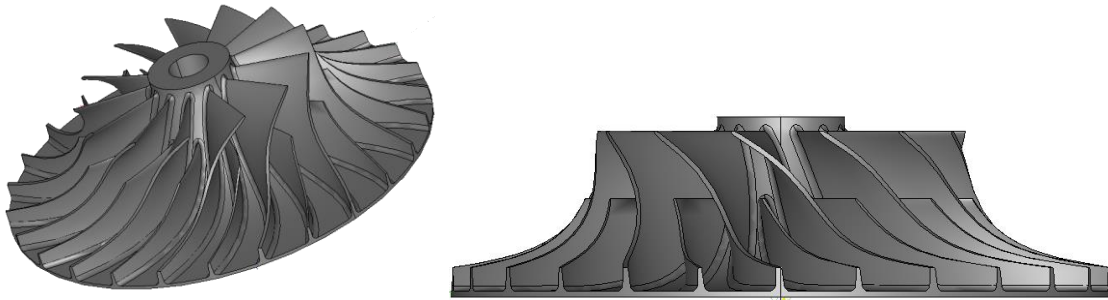[1] Romanian Research and Development Institute for Gas Turbines COMOTI, Bucharest, Romania

Fig. 1 Impeller CAD model

Table 1. Compressor's parameters

Blade number	13
Splitter blades number	13
Hub radius	129[mm]
Tip radius	134[mm]
Angular velocity	45,000 [rpm]
Ratio of compression	4.7
Mass flow	1.4 [kg/s]
Axial force	6000 [N]
Thrust	800 [N]

2.2 Material properties

The material considered for the model is an aluminium alloy, namely AL2618. Its properties are summarized in the table below [8].

Table 2. Material properties

Tensile Strength, Yield	372 [MPa]
Tensile Strength, Ultimate	441 [MPa]
Modulus of Elasticity	74.5 [GPA]
Poisson Ratio	0.33
Density	2760 [kg/m^3]

2.3 Mesh

The imported geometry is meshed using tetrahedron elements method. The model contains a total of 658,671 elements and 1,020,539 nodes.
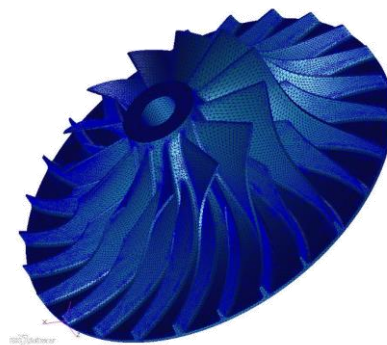
Fig. 2 Mesh model of the impeller

2.4 Boundary conditions

For this analysis the inner diameter about front face was locked against tangential and axial movements and the cylindrical hub surface was constraint tangential (Fig 3). Another condition applied was rotational force. Furthermore, Fig. 4 presents how the compressor is mounted into the assembly.
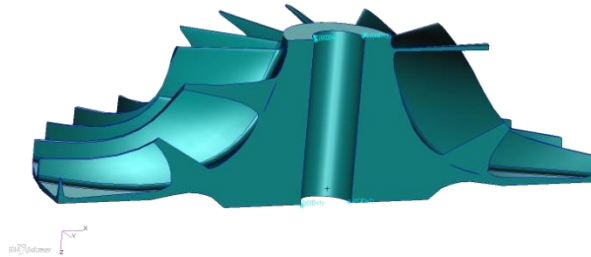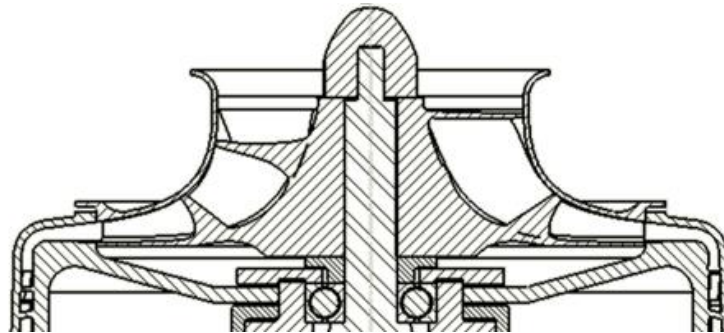

Fig. 3 Boundary conditions

Fig. 4 Compressor mounting detail

3. **RESULTS AND DISCUSSIONS**

Below are presented the results of the performed analysis. The figures show the von Mises stress distribution and the displacements.
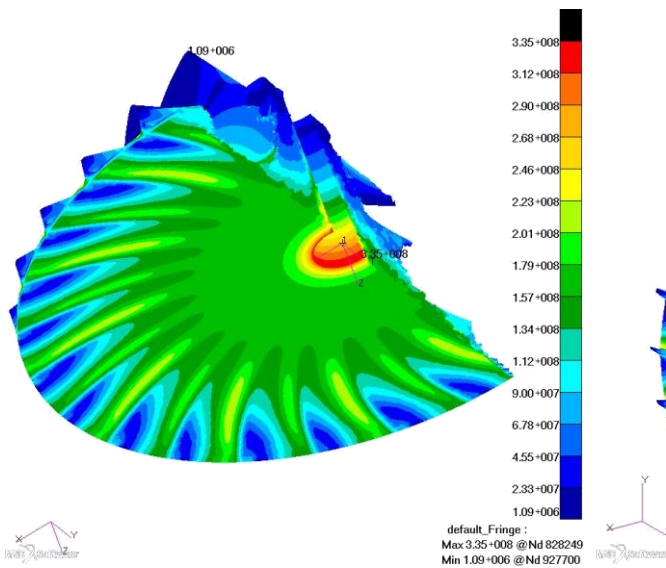

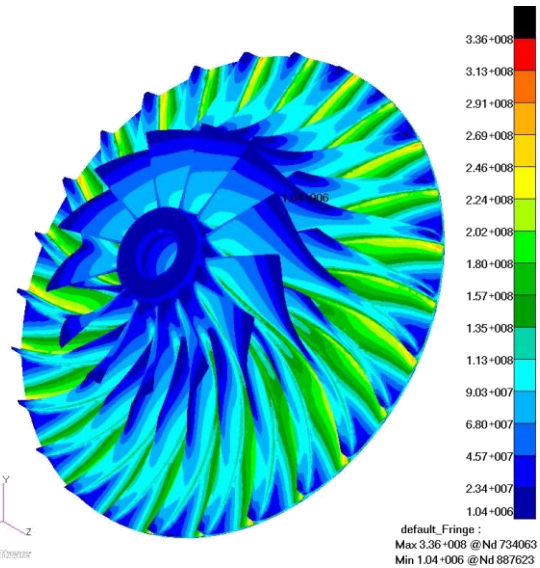**Fig. 5 Von Mises stress distribution-section view [Pa]**   **Fig. 6 Von Mises stress distribution [Pa]**
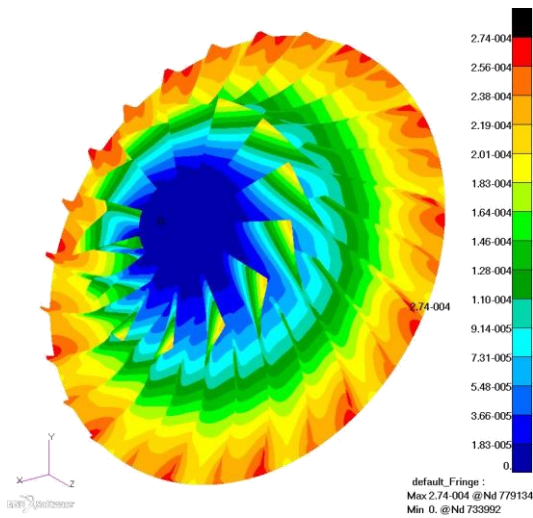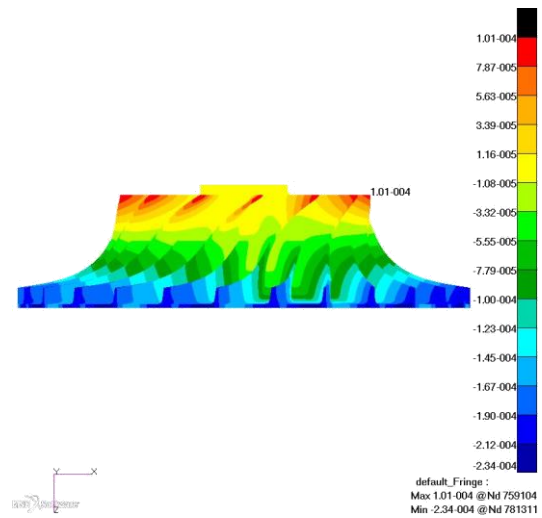
Fig. 7 Total displacements [m]   **Fig. 8 Axial displacements [m]**

The maximum stress of 336 MPa (Fig. 5, Fig. 6) is achieved around the central hole area, resulting in a safety factor of 1.107. The maximum axial displacement is 0.274 mm (Fig. 7) on the tip of the blade in the inlet section area, in contrast to the outlet section where the axial displacement is only -0.234 mm.

In attempt to reduce the main negative aspects of the previous design solution, the shape of the disc was modified near the central hole by practicing a boss and a rounded circular slot (Fig. 9). The resulting rotor height is optimal since the maximum stress is arranged to be away from the contact zone.

Optimising a geometry has, from a technological standpoint, the goal of minimizing the usage of raw material. Also, in order to realise an optimal disk, a base profile that would ensure an even load throughout every section was used. Therefore, the resulting height of the rotor ensures a safe load distribution, while keeping waste to a minimum.
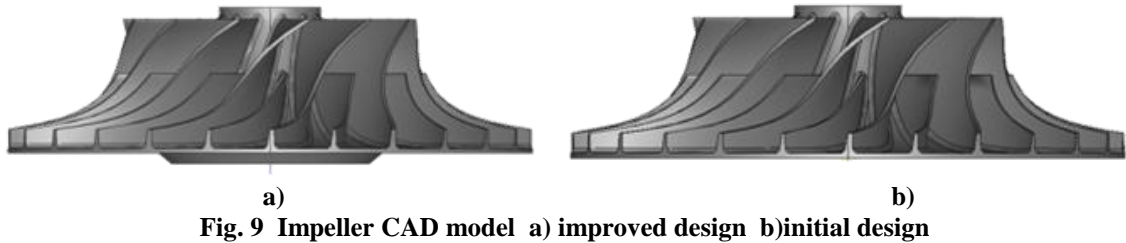

a)   **b)**
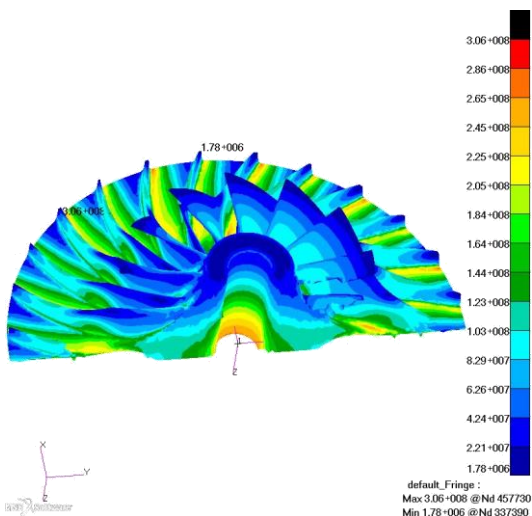**Fig. 9 Impeller CAD model a) improved design b)initial design**

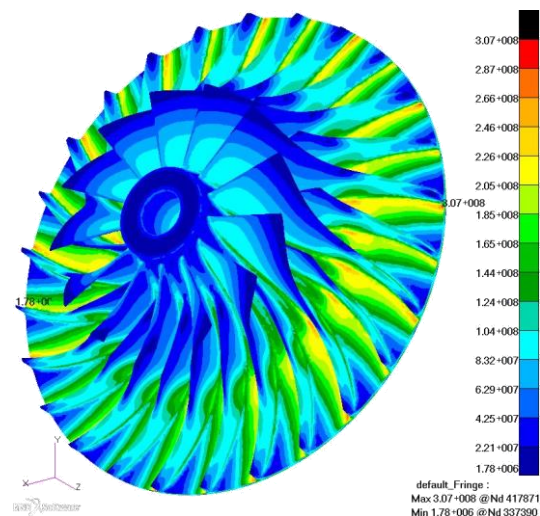**Fig. 10 Von Mises stress distribution–section view [Pa]**   **Fig. 11 Von Mises stress distribution [Pa]**
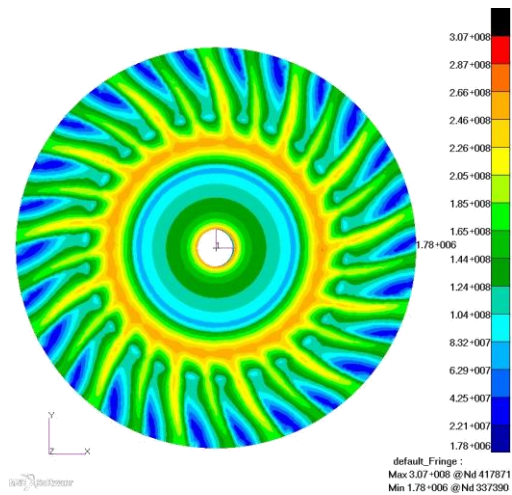
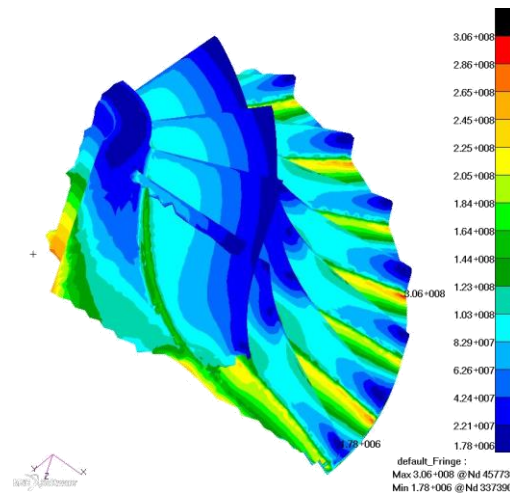**Fig. 12 Von Mises stress distribution [Pa]**

Fig. 13 Von Mises stress distribution [Pa]

From the above figures a maximum stress of 307 MPa can be observed, resulting in an increase of the safety factor up to 1.21. The maximum stresses appear in the area of the connection radius of the blades due to stress concentration. In this case, the value of the fillet radius is 2mm. The variation of the local maximum stress depends on the fillet radius, varying indirectly proportional to the radius value.
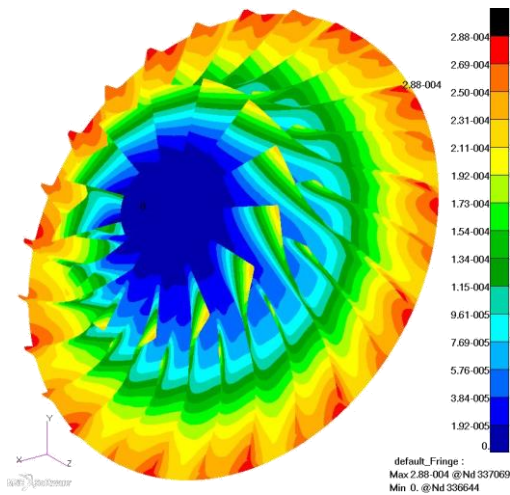
Fig. 14 Total displacements [m]

Fig. 15 Axial displacements [m]
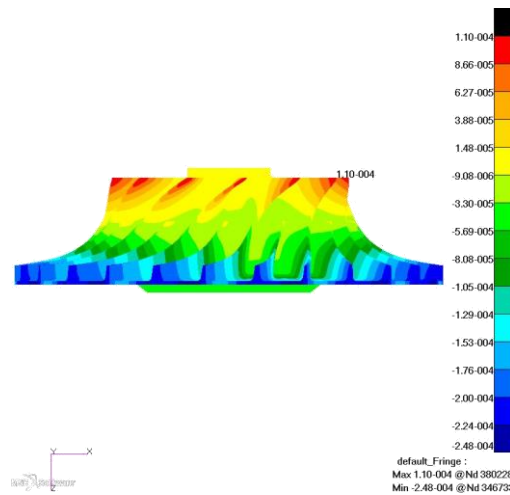
The maximum axial displacement is now 0.248 mm on the tip of the blade in the inlet section area, whereas in the outlet section the axial displacement is 0.11 mm. At the nominal working speed, the deformation at the top of the blade has the effect of decreasing the clearance at the output region and increasing the clearance in the input region.
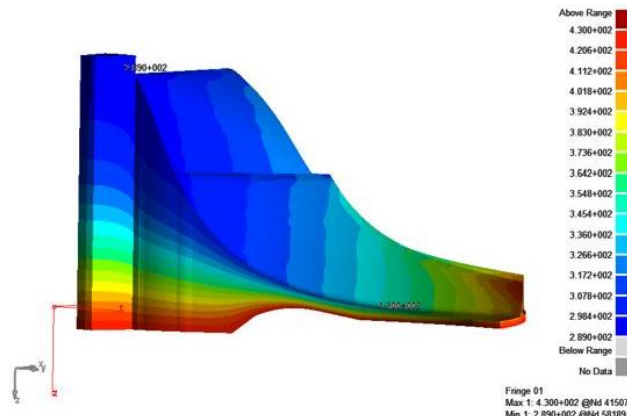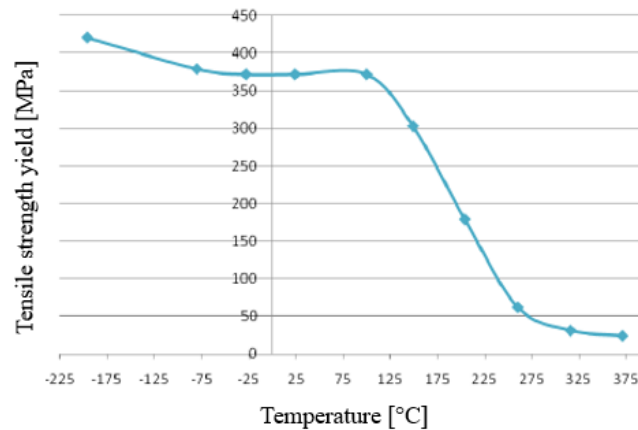

Fig. 16 Temperature distribution [K]

23

Fig. 17 Yield tensile strength variation with temperature

In the maximum stress area (307 MPa) the temperature is 408 K (135°C) and the yield tensile strength 323 MPa. The coeficient corrected with temperature is 1.05 (323/307).

5. CONCLUSIONS

For both impeller geometries, the same blades model was used. The analyses were performed independently for each impeller geometry. The most notable change is observed for von Mises stress. The initial design had a maximum stress in the central hole area. The stress was significantly reduced in that area in the subsequent design when the shape of the disc was modified near the central hole. The change in impeller geometry improved the impeller's structural properties and lead to an increase of the safety factor.

The aluminium alloy AL2618 is suited in this case given it offered a satisfactory safety factor for the operating speed and temperature. The geometry of the rotor disk was improved using the basic profile of the flow channel and the thickness of the equal strength disk.

ACKNOWLEDGEMENT

REFERENCES

[1]. Visser, W. P. J., Shakariants, S. A., and Oostveen, M., Development of a 3kW micro turbine for CHP applications, ASME Turbo Expo 2010, GT2010-22007, Glasgow, Scotland;

[2] de Villiers, L.C.B, 2014, Design of a Centrifugal Compressor for Application in Micro Gas Turbine, Master's thesis, Stellenbosch University;

[3] C. Xu, R. S. Amano, 2012, Aerodynamic and structure considerations in centrifugal compressor design blade lean effects, GT2012-68027;

[4] S. Pakle, K. Jiang, 2018, Design of a high-performance centrifugal compressor with new surge margin improvement technique for high speed turbomachinery, Propulsion and Power Research;

[5] C. Kim, H. Lee, J. Yang, C. Son, and Y. Hwang, 2016, Study on the performance of a centrifugal compressor considering running tip clearance, International Journal of Refrigeration, vol. 65;

[6] G.C. Wang, J.F. Li, X.J. Jia, F.Y. Li, Z.W. Liu, 2014,Study on erosion behavior and mechanism of impeller's material FV520B in centrifugal compressor, J. Mech. Eng. 19;

[7] Liu, Shujie, et al, 2016, Fatigue life assessment of centrifugal compressor impeller based on FEA, Engineering Failure Analysis.

[8] www.matweb.com

CALCULATING AND SETTING UP A SCHLIEREN SYSTEM

Emilia PRISACARIU[1], Valeriu VILAG[1] , Razvan NICOARA[1], Cosmin SUCIU[1] , Cristian DOBROMIRESCU[1,] , Madalin DOMBROVSCHI[1]

ABSTRACT: This paper defines the parameters one must focus on while trying to set-up a schlieren system; its purpose is to follow and explain a mathematical path that can be used to pre-set a system, to offer alternatives in terms of optical path components, and point to the optimum equipment. The end result will be building and aligning an actual optical Schlieren system that will be used to visualize phenomena that are invisible to the naked eye.

KEYWORDS: Z-type, Schlieren, Shadowgraph, parabolic mirrors

NOMENCLATURE

A-   slit area
Al - aluminium
B- brightness of the light source
CRI- colour rendering index
D_0 - diameter of the nozzle
E - general illumination of the background
E_0 - illumination upon the first mirror
C - contrast
S   - sensitivity
P_0 - flow pressure
P_1 - atmospheric pressure
f   - focal distance
f_1 - focal distance of the first parabolic mirror
f_2 - focal distance of the second parabolic mirror
f3 - focal distance of the camera's lens
fps- frames per second
n_0 - refractive index of atmosphere
x   - distance from the nozzle to the first shock diamond
ΔE- differential illumination
ε - anlge of refraction
$\emptyset$ - efficacy of the light source
$\boldsymbol{\theta}$ - the offset angle.

1.   INTRODUCTION

The schlieren system's conventional form is attributed to the german scientist Auguste Toepler, his predecessors being Jean Bernard Foucault (1849) and Robert Hooke (1665). [1] The "schliere" word is of german origin and means "streak". Hubert Schardin was another important figure, whose work represents the last important milestone of the technique. Schardin was the first to apply filters and to obtain quantitative information based on schlieren measurements. [6] The working principle is simple: the Schlieren technique relays on the deflection of light by a refractive index gradient.

The latest development in the field implies using a Schlieren system and a PIV system together, in order to fully characterise the flow. This subject is debated in G.Settles' paper, "*Schlieren "PIV" for turbulent flows*"[7]. There are many adaptations of the schlieren technique .

A very important one is the "*coloured schlieren*", which allows one to visualize, for example, the shock waves over a 2D wedge-plate, where every type of shock wave has a different colour. This can be achieved by placing a prism in front of the light source. The notion of a coloured schlieren has been inspired by the idea of coloured interferometry. One paper that focuses on the optical path of a coloured schlieren system that includes a double-prism, and has variable sensitivity is "*A variable sensitivity and orientation colour schlieren system*", by D.R. Phillpot [8].

The third most important new use of the technique is the *quantitative schlieren*. This technique's purpose is to measure refractive-index distributions and other quantities related to the flow. A paper that characterises the use of schlieren as a quantitative tool is „*A quantitative schlieren method for the investigation of axisymmetrical shock waves*", by Andrzej Cwik and Helmut Ermert [9].
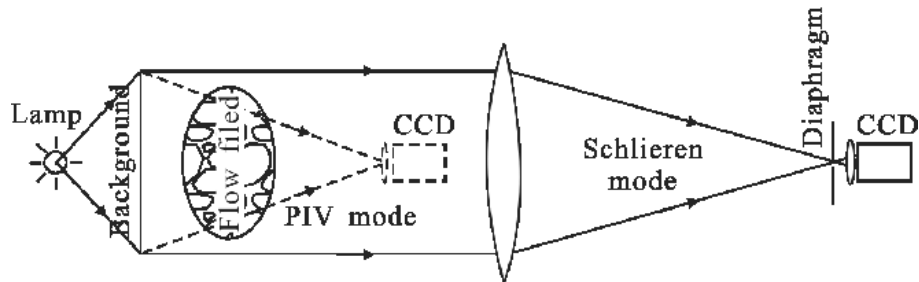

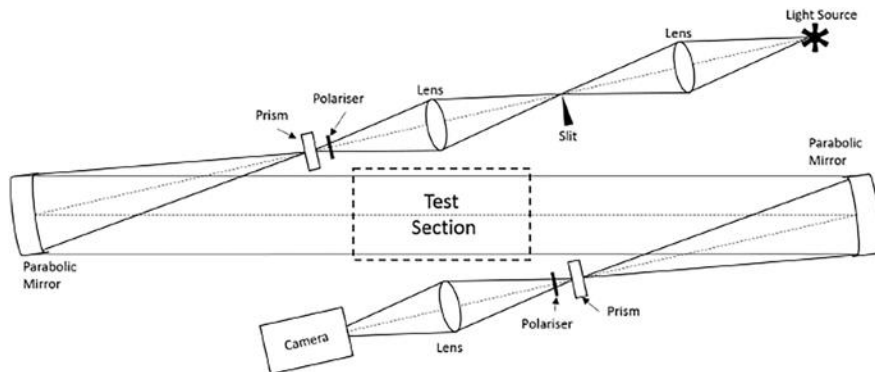**Fig.1 PIV - background oriented schlieren system [4]**

Fig.2 Coloured Schlieren Configuration [5]

The optical characterisation of density can be achieved through the schlieren method of visualization, which can take many forms. It can be easily changed by redefining the optical path: using lenses, 2 parabolic mirrors (Z-type), one single mirror (single mirror configuration), or not using any mirrors or lenses and observing the density changes on a speckled background (Background Oriented Schlieren or Synthetic Schlieren). Usually, the schlieren method, regardless of its configuration, uses one focusing lens, that helps focusing the rays from the light source.

It is important to know the scale of the experiment and how sensitive the system has to be in order to register the density variation. Since the point of the experiments conducted is to obtain quantitative results with the help of the schlieren system, it is safe to say the system will be used as a "*quantitative schlieren*", and therefore, its configuration needs to be the most sensitive; the highest sensitivity belonging to the Z-type schlieren system. Another reason for setting up a Z-type is it implies using mirrors instead of lenses, and mirrors have a larger field of view; off-axis mirrors also cancel each other's aberration in this configuration.

2.   OPTICAL PATH CALCULATION AND ERRORS

The shock diamond formed by air exiting a supersonic nozzle is used to conduct a Shadowgraphy test. Shadowgraphy is defined as: a simple light source that helps the object cast a sharp shadow over a white board.

This shadow can only show large variations of density (for example if the flow is supersonic or if there's a variation of temperature (see Fig. 3 a) and b)). Taking shadowgraph pictures of the phenomenon in this case, helps with future calibration. From the showgraph pictures, one can learn what errors might appear. For example, if the image is blurry, the CCD camera's parameters must be reset or the contrast sensitivity must be increased, in order to see all the elements of the shock diamond. In the figure below, some errors in performing the shadowgraph method can be spotted. The first error is the penumbra just above the air compressor's nozzle (Fig. 3 a). The penumbra appears when the light source is not a point source, but rather an extended one, causing the double-image of the compressor nozzle to form. This means that the jet itself will also have a double image. The second error can be spotted in image of the plume, where the image is too dark and the amout of zoom-in from the camera is affecting the quality of the image. Errors regarding the equipment, and not the technique can be spotted with the help of shadowgraphy.
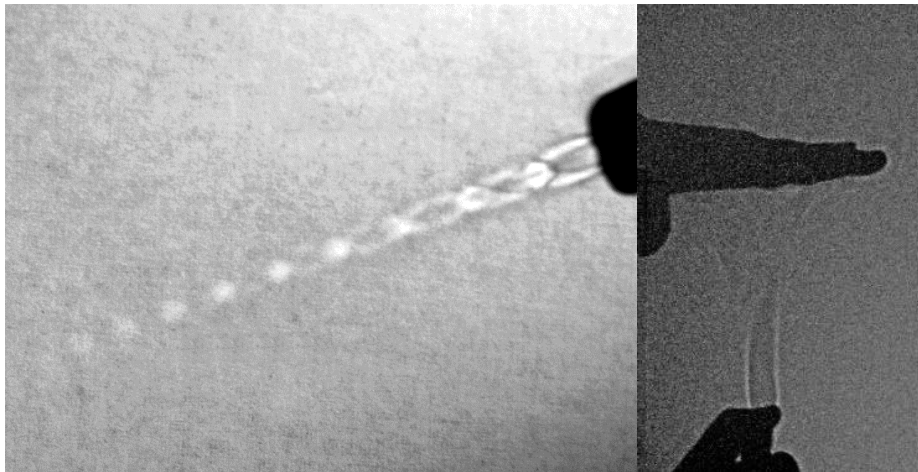

Fig.3 a) Shadowgraphed shock diamond at the exit of an air compressor; b) lighter plume over a hand (pictures taken at INCDT Comoti)

The distance between the nozzle and the first Mach disk of the shock diamond, can be calculated with the following formula, where x is the distance, D_0 is the nozzle diameter, P_0 is flow pressure, and P_1 is the atmospheric pressure:

$$x = 0.67 D_0 \sqrt{\frac{P_0}{P_1}} \qquad (1)$$

For more information on the matter of diamond shock, and compressible fow in general, one can refer to J.D. Anderson, *Modern Compressible Flow with Historical Perspective*, 3rd Ed., 2003 [10].

The comparison between the first picture and the above-mentioned formula can be obtained after framing the jet into a background made out of millimetric paper. With the help from the previous formula, and knowing P_0, P_x and measuring D_0, one can find that "the zone of silence" spreads over a distance of 4.4 mm. However, pictured below, the "zone of silence" appears to measure a bit over 4 mm, the error comes from the fact that the background, the jet and the camera are not placed perfectly parallel.
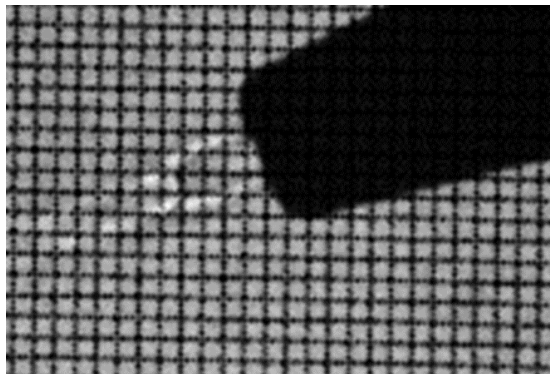

Fig.4 Shadowgraphed shock diamond with millimetric scale (picture taken at INCDT Comoti)

This is another error to make sure to avoid. The experiment must perfectly align with the camera, in order to obtain good results.

The shadowgraphy can be a powerful learning tool before concentrating on a schlieren system wich is more complex because of the optical elements it includes.

This paper however concentrates on the precalculation and presetting of the Z-type schlieren, the afore mentioned shadowgraphy experiment was described in order to underline the fact that by using shadowgraphy (which is less time and money consuming, but has a very poor sensitivity) some of the errors can be taken into account, when thinking about designing a schlieren system.

2.1. Establishing the type of mirrors to be used

The Z-type configuration draws its advantages from the mirrors'placement; the offset angle θ assures one there will be no aberrations in the system, such as coma or astigmatism (the first mirror is the negative of the second one). The aberration of the parabolic mirror grows with θ and with (f/n0).

The offset angle must be very small, especially in the one-mirror configuration, in order to avoid a double intersection of the object with the ligh: firstly, in the light's path from the source to the mirror and secondly from the mirror to the camera.

In the single-mirror configuration, the most important problem is the placement of the object to be observed. If the mirror has a small diameter, the testing area will suffer severe limitations, making it very hard to avoid the above-mentioned error.

This error, combined with the aberration of the mirror, excludes the sigle-mirror configuration as the right configuration for the experiments to be conducted.

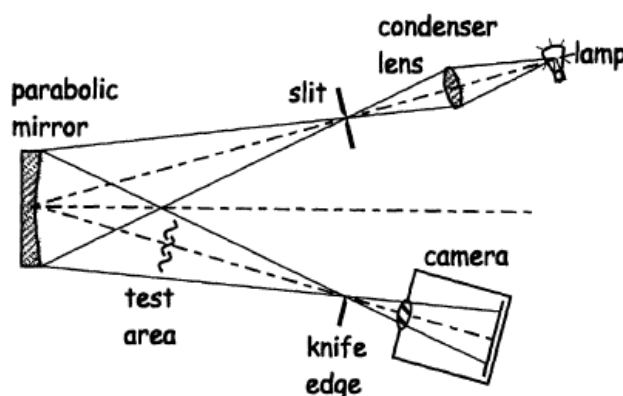The most sensitive configuration remains the Z-type configuration.

Fig.5 Single-mirror off-axis configuration (*G.S.Settles 2001*)

In the Z-type configuration, the same thing can happen if the distance between the mirrors is smaller than $2f_2$. The parabolic mirrors used in schlieren have a large effective focal length, that cancels the risk of a very small testing area and increases the sensitivity. The distance between the mirrors can be as large as the experiment requires, as long as the mirrors are corectly aligned. Another advantage of the parabolic mirrors is the large field of view.

The schlieren visualizing technique uses Al plated mirrors, because it emits in the spectrum of the visible light, matching the light sources's spectrum. Other options may not suit the matter, such as the gold plated mirrors which are useful only in the IR spectrum.

Based on the scale of the experiments, one can also choose the diameter of the parabolic mirrors to be used. For example, the shock diamond shadowgraphed before , only spreads on a distance of a few millimiters, so the diameter of the mirrors can be a few times bigger than that. In general, this configuration will be used to observe small perturbations.

With these facts in mind, knowing that the mirrors need to be Al plated, working in the spectrum of 400-700 *nm* (same as the light source), with a slightly bigger focal length, and a small diameter, the author decided to use the 76 mm, Al protected, parabolic mirrors from Edmund Optics.

More data about the characteristics of the mirrors can be found in the table containing the equipment's description (Table 2).

As Settles well stipulates in his iconic work [3], the Schlieren Z-type system has the advantage of a very large test area (much larger than $2f_2$)). In that case, the use of flat mirrors is necessary, in order to reduce the laboratory space needed for conducting the experiment.

Althought, folding mirrors are not desirable unless compulsory, because they introduce a high sensitivity to vibrations in the system, impose a very big angle of offset that increases the aberration of the mirrors and also make the system very hard to be aligned. The Z-type Schlieren system's optical path is represented in the following figure.
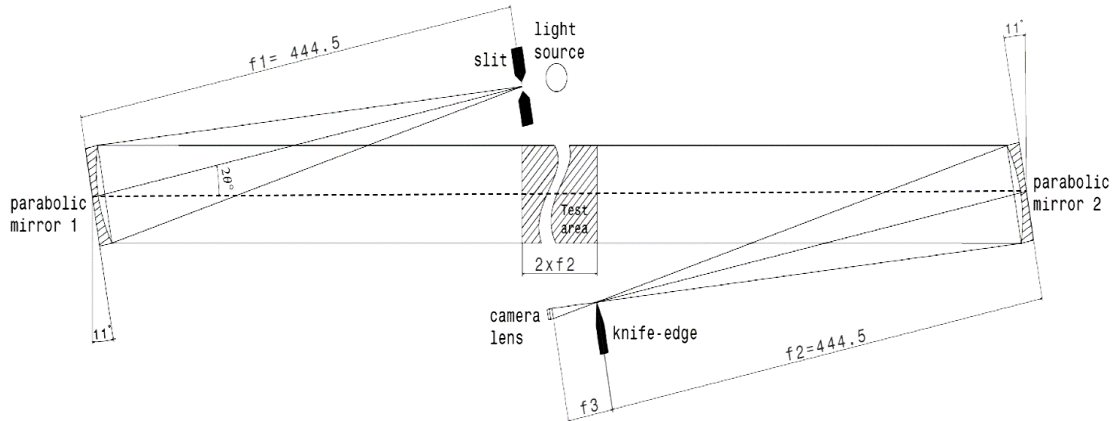

Fig.6 Z-type configuration (author's resulting configuration)

The sketch presents a tilt angle of the mirror equal to 11° . The angle it's exaggerated in order to better fit the equipment in the sketch. Normally, the off-axis mirrors are tilted at an angle not higher than 3° [1]. Also, *f3* represents the focal distance of the camera, which changes with the camera lens.

2.2. Choosing the light source

Choosing the right light source of the Schlieren system is as important as choosing the right optics. The light source needs to be point-like, so that the set-up can respect the Schlieren configuration and for the calibration knife to be effective [1], and the angle at which the rays spread from the source needs to be small, in order to form a very sharp shadow of the object that needs to be observed. In the Schlieren system, before the introduction of the knife edge into the focal point of the second mirror, the background will be illuminated uniformly, the light will be too bright and the sensitivity will be very low. The sensitivity increases while the area of the point source image decreases [1].
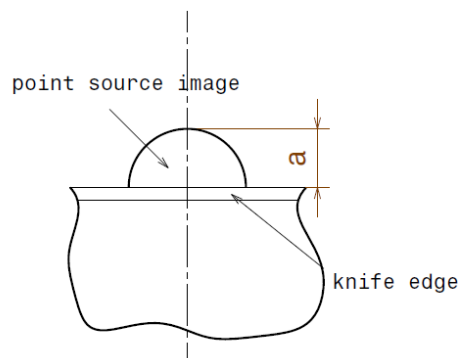

Fig.7 Cut-off of the point source image

The source used needs to cover the visible spectrum, and have the same wavelength as the mirrors. As mentioned before, the wavelength interval for the present configuration is 400-700 nm.
There are many options when it comes to choosing the proper light source, and as described in the literature [1], one can use either of the following: Xenon arc lamp, incandescent or halogen light bulbs, lasers, even the common laser pointer.
The main disadvantage of using an incandescent or a halogen lamp is the fact that they are spatially and temporally incoherent light sources. This characteristic can be cancelled by the use of filters or, like in this case, by adding a slit in front of the source. The slit complicates a bit the process of determinating the exact illumination on the first mirror of the system.

Table 1. Light sources performances [2]

Source type	Luminous flux [lm]	Efficiency[lm/W]	Brightness [Mcd/m^2]	CRI	Lifetime [kh]
Incandescent 60W	900	15	10	100	1
Halogen 50W	1000	20	20	100	2
LED 2002	125	25	3	75	60
LED 2013	1000	250	10	90	60

For this application, the matching of an H1 automotive light bulb with the optical system will be questioned. The idea of a halogent automotive light bulb can be found in an endless count of papers, all starting with the pinacle of the technique, the book writtem by G.Settles, „*Schlieren und shadowgraph techniques: visualizing phenomena in transparent media*" [1].

As seen in Table 1, for the halogen light bulb, the efficacy is the same as for the H1 light bulb used in this application, which has a luminous flux of 1100 and a power of 55, and can be calculated with the next formula:

$$\emptyset = \frac{lumens}{watts} \tag{2}$$

The result of the above-mentioned formula shows that for every watt used, this lamp produces 20 lumens. The radiant intensity for this bulb is given to be 105 candela, based on the manufacturer's indication, but the system will not be using all the light coming from the source. Depending on the geometry of the slit, one can calculate the illuminance on the first mirror of the system. If the slit's area is A, and the luminance (or brightness) after the slit is B, that can be approximated to $1,2 \cdot 10^7 candela/m^2$, one can calculate the illuminace on the first mirror:

$$E_0 = \frac{B \cdot A}{f_1^2} \tag{3}$$

In this case, E_0 results to be 150 $candela/m^2$ (lux), without any knife cut-off. The sensitivity is correlated to the cut-off, but literature mentiones that an experiment which does not need a very sensitive system, usually uses a 50% cut-off. This creats a good-enough contrast and also makes placing the knife-edge more exact. The second mirror will have an illuminance of 75 lux, after the knife-edge is placed.

A difference in the formula of illumination occurs if one adds new optic elements to the system. The value for contrast can be set only after the installation of the system and only after the first images are taken, because the contrast is considered to be the ratio between differential illumination (ΔE) of a point and the general illumination of the background.

$$C \equiv \frac{\Delta E}{E} \tag{4}$$

This formula (4) can also be written as a ratio between the increment gain of illumination times the area of light that has not been cut-off by the knife edge and the magnification factor multiplied by the square of the first focal distance. The contrast is not the only quantifiable variable of importance. The sensitivity plays a very big role, and can be calculated using the next formula:

$$S = \frac{\Delta C}{d\varepsilon} \tag{5}$$

The Schlieren sensitivity is the rate between the contrast and the refraction angle and it's the defining parameter of the technique.

After calculating all of these aspects, the conclusion is that the light source which has the highest value for the luminous flux can be considered the best one, because a lower value for illuminance can always be achieved by adjusting the slit's geometry.

As seen in this chapter, the halogen light bulb has a luminous flux of 1100 *lm,* while the other options would have been an incandescent light bulb with only 900 *lm*, or a LED, with 320 *lm*.

The halogen light bulb is the preffered choice for the system, not olny because of the luminous flux, but also for the CRI, and the higher brightness.

From this point on, the matter of calibration starts, which changes with each experiment, and does not make the subject of this paper.

3. EXAMPLE. SCHLIEREN VISUALIZATION OF A LOW EMISIVITY JET

The present experiment's purpose is to demonstrate otherwise the functionality of a small-geometry nozzle. The visibility of the jet is almost none, due to the fact that the chemical compound exiting the nozzle is mainly water vapours at high temperatures. Due to space limitations, the type of Schlieren used had to be a single-mirror configuration. Keep in mind that the installation was not designed for the use of optical equipment. It has 3 glass windows, but their positioning and fabric makes it hard to apply this particular technique.

Calculations for the emissivity of the jet shows that the emissivity is very low, and the glass from the windows it's screening the jet when one tries to visualize it by means of infrared thermography. Also, while the vacuum chamber is sealed, the glass window splits the light beam in 2, causing the image to double and even triple if the distance from the jet to the parabolic mirror is too small or at the wrong angle.

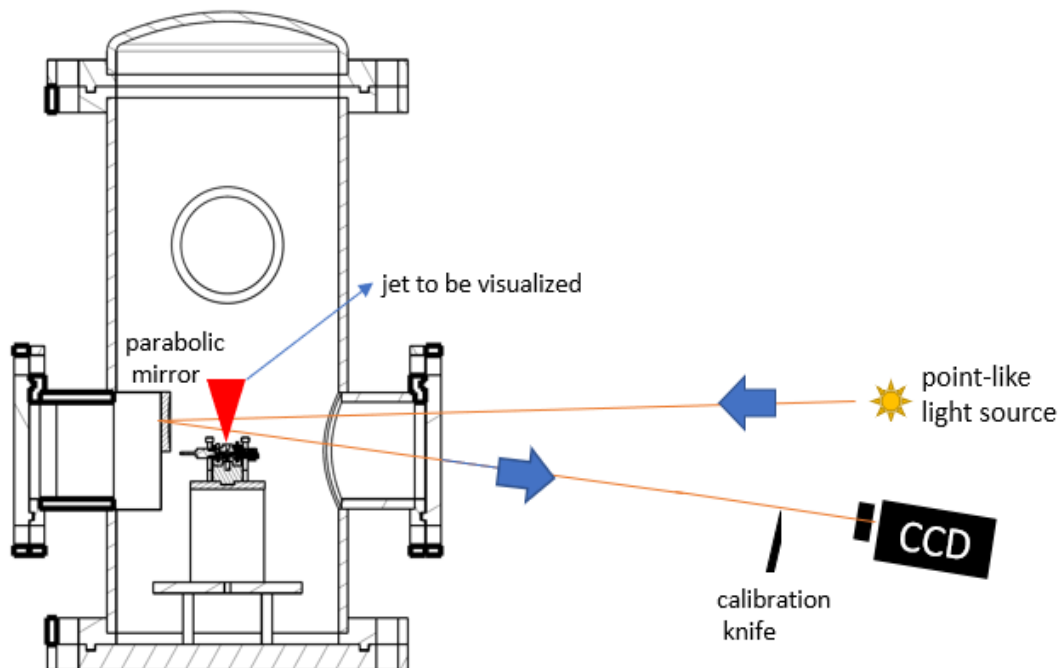The one-mirror experimental set-up is depicted in the following figure.

Fig.7 Sketch of the one-parabolic-mirror configuration

The one-mirror configuration represented the only solution for this problematic experiment. The entrance into the chamber had a very small diameter which caused the angle between the light beam going into the parabolic mirror and the light beam exiting the mirror to be really small - fact that made the optics extremely difficult to align. Another space-limiting issue was the fact that one of the parallel glass windows had little to no space between it and a very important panel that is a part of the installation and couldn't be moved at that time. Due to this fact, the Z-type configuration system, with all its advantages couldn't be applied.

The mathematical path presented before applies if one has doubts about the system sensitivity or tries to find the best configuration when space is not an issue. Giving the fact that the measured temperature of the jet reaches almost 2032K , the densitiy variation will be an important one. Also, it helps to try the shadowgraph method first, because it's less sensitive. If Shadowgraph shows the difference in density, the Schlieren will definitely "see" it too.
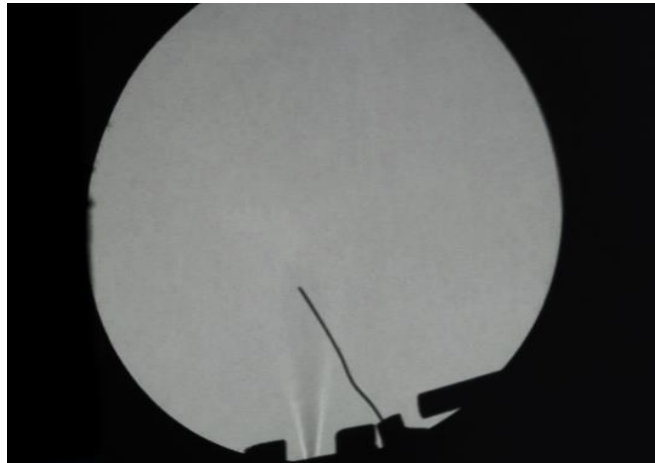
Fig.8 Image of the jet acquired with the Shadowgraph method(pictures taken at INCDT Comoti)

Table 2. Equipment specification

Source type	LED	321 lumens
Parabolic mirror	Ø76mm	EFL 444.5mm
Calibration knife	Black painted	-minimum reflections
CCD Camera	Phantom Veo 410L	Max.7.000fps

The difference between the sensitivity of the Shadowgraph and the Schlieren systems can be seen in Fig.8 and Fig.10, the first one does not show the entire contour of the jet, it only shows the area where the density difference is very large. This assessment is more important if one keeps in mind the fact that the jet is not at all visible by the naked eye.

The experiment was carried on under the following conditions:
-    the distance between the point-like source and the parabolic mirror was approximately 1m, the distance from the parabolic mirror to the knife insertion point was the focal length of the parabolic mirror;
-    the camera and the calibration knife were mounted together on a tripod, and the point like source was mounted on a different tripod. A very important aspect was mounting the two tripods at the same hight, in this way the addition of another light displacement plane was avoided.
-    the calibration knife cut was nearly 80%, due to the fact that the light source was extremely powerful and extended.
-    the parabolic mirror was placed inside the open chamber with a mount that guaranteed the vertical position. If the mirror was inclined, it would have been impossible to find the right angle at which to position the calibration knife.
-    the Schlieren images were recorded at 8500fps, this CCD speed reduces the light intensity as well.
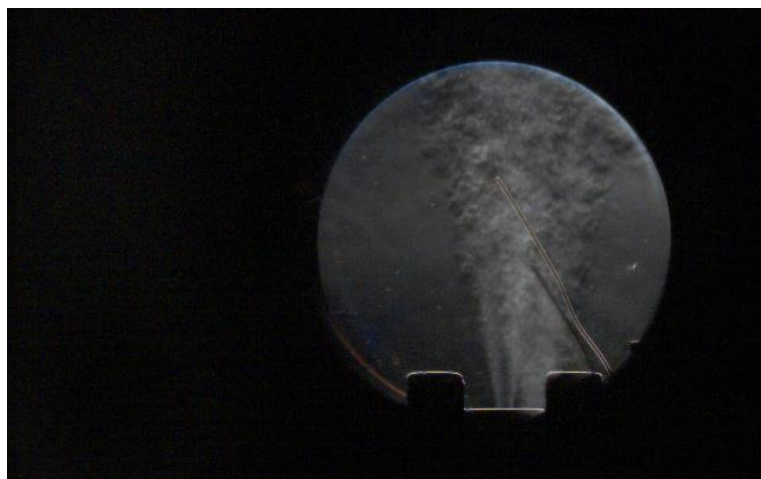

Fig.9 Image of the jet before post-processing(pictures taken at INCDT Comoti)

The post processing was focused on the next steps:

- background removal (a picture was taken before the jet, so that the pixels or eventual glares could be removed afterwards), adjusting the contrast, focusing on the phenomenon;
- in Fig.10 (b) one pixel intensity was chosen as the background substitute, and the intensity chosen was the one that underlined the jet through by creating a contrast. Also, the thermocouple could be kept in the image in this way
- the thermocouple that appears in Fig,9 was eliminated from the post-process version of the pictures (Fig.10 (a))because it also appeard in the background image.
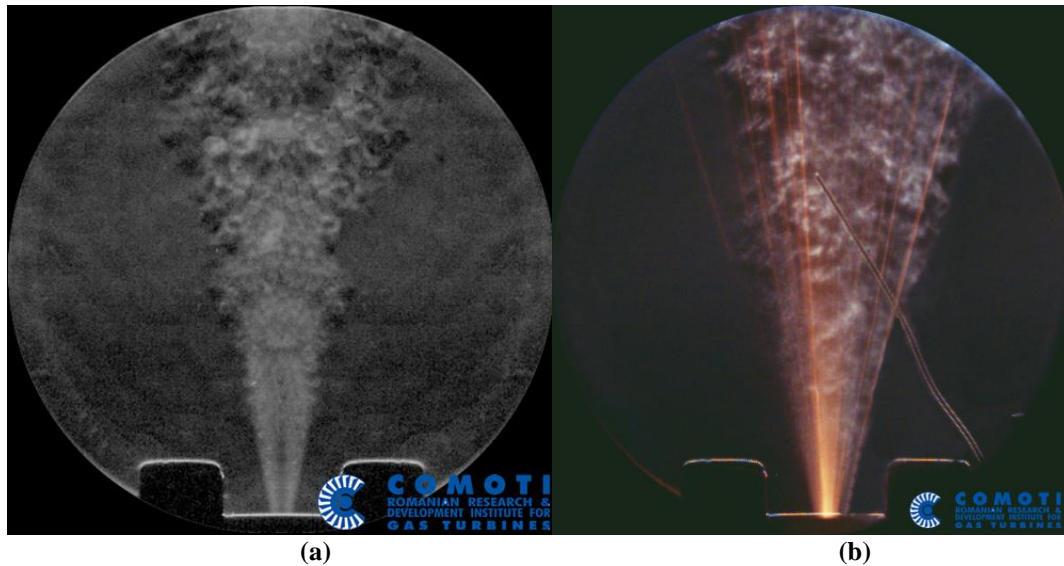- the post processing tool used was the 2020a Matlab software;

(a)   **(b)**

Fig.10 Images of the jet after post-processing(pictures taken at INCDT Comoti)

4. CONCLUSIONS AND FUTURE WORK

Before setting up a Schlieren system, one must know the scale of the phenomena to be tested, and must be able to approximate the sensitivity needed in order to capture the desired images.

The exact sensitivity can only be calculated after the system is installed, but literature offers a big variety of experiments that allows one to approximate some of the variables and then use it to precalculate the system.

The choice of optics has been motivated and the light source has been calculated, the only remaining variable right now in the system, before the experiment calibration, is the high speed camera, which in the presented case is the Phantom Veo 410L, whose characteristics (7000 fps at a resolution of 1280x720) are more than enough to capture the essence of all intended experiments, but if one does not need to capture events that happen at a high speed, a regular camera can also be used.

Setting the Schlieren system allows one to visualize the variation of density that it's undetectable under normal visualizing conditions and can prove or disprove results obtained by numerically simulating the same phenomenon.

The experiment described in this paper is just an example of a real test-case. As in many real-life applications, the conditions of the test case, are not ideal. The Z-type configuration should always be the first choice when thinking about building a schlieren system, but sometimes one can encounter space limitations. In this case, the set-up will suffer important changes. Any set-up that respects the basic principles of the schlieren technique is viewed as such, even if the optical path has more optical elements, like for example it could include flat mirrors, a slit in front of the light source, different mirrors, no mirror, lenses or a diaphragm.

The next step in using the system is calibrating it to form a quantitative system. The post processing code will be improved to the point where it will become a in-house software through which the displacement angle will be calculated, and will allow one to fully characterize the flow.

The schlieren method of visualization is a non-intrusive method, the main disadvantage is it needs optical access to the flow. The Schlieren method can be used in both supersonic and subsonic applications, if the difference in density is big enough to be detected.

REFERENCES

[1] Settles G.S., 1949, *Schlieren und shadowgraph techniques: visualizing phenomena in transparent media*, Springer-Verlag Berlin Heidelberg GmbH, Berlin

[2] Jüstel, T, 2018, *Inkohaerente Lichtquellen Glueh und Halogenlampen,* https://www.fh-muenster.de/ciw/downloads/personal/juestel/juestel/4-InkohaerenteLichtquellen-Glueh-_und_Halogenlampen_english_-1.pdf

[3] Rathakrishnan E., 2007, *Instrumentation, Measurements, and Experiments in Fluids,* vol. I, CRC Press, Taylor&Francis Group, Florida

[4] Ding H., 2006, Experimental investigation of aero-optical effect due to supersonic turbulent boundary layer, *Infrared and Laser Engineering*, vol.45, issue 10

[5] Schulz J., 2019, Flow visualization using a Sanderson prism, *Journal of Visualization, vol 22*

[6] Mazdumar A. 2013, Principles and techniques of Schlieren Imaging Systems, *Columbia University Computer Science Technical Reports*, CUCS-016-13

[7] Gary S. Settles, Dennis R. Jonassen, *Schlieren "PIV" for turbulent flows*, Optics and Lasers in Engineering 44(3):190-207

[8] D. R. Philpott, *A variable sensitivity and orientation colour schlieren system,* Experiments in Fluids 29, 42–44 (2000)

[9] Andrzej Cwik, Helmut Ermert, *A quantitative schlieren method for the investigation of axisymmetrical shock waves,* Ultrasonics Symposium, 1993. Proceedings., IEEE 1993

[10] J.D. Anderson, *Modern Compressible Flow with Historical Perspective*, 3rd Ed., 2003, ISBN-13: 978-0072424430, ISBN-10: 0072424435

HEAT TRANSFER ANALYSIS ON GAS TURBINE ROTOR BLADE

Madalin DOMBROVSCHI[1], Cosmin SUCIU[1], Razvan NICOARA[1], Emilia PRISACARIU[1], Cristian DOBROMIRESCU[1], Ioana BUCUR[1]

ABSTRACT: In this paper, a heat transfer analysis for a gas turbine rotor blade was done. In the first part of the paper, the work of other authors was presented in order to have a better understanding of the heat transfer phenomenon inside a gas turbine blade. This paper's motivation is based on the need for a better understanding of the heat transfer phenomenona. A presentation of the geometry and the numerical calculations precedes the results which are displayed in a graphical way. All the results obtained from the internal cooling case of the rotor blade are compared with the case were there is no cooling for a better observation of the blade temperature differences. The final conclusion is that the results are encouraging and the simulations corroborates the results.

KEYWORDS: Heat Transfer, CFD, Gas Turbine, Rotor Blade, CFX

NOMENCLATURE

ΔT_1	difference between inlet and outlet temperature of the first cooling domain
ΔT_2	difference between inlet and outlet temperature of the second cooling domain
T_{sf}	total temperature in stationary frame
p_{rel}	relative pressure
$\dot{m}$	mass flow rate
p_{ref}	reference pressure
n	rotational speed
T_{ref}	reference temperature

1. INTRODUCTION

Gas turbines play an important role in today's industrialized society and as the demand for power is constantly increasing, the power output and the thermal efficiency of gas turbines must increase in order to meet the forecasted demand [1]. Some other major applications for gas turbines, besides power generation, are aviation, oil and gas industry and marine propulsion. Various methods have been developed and investigated in recent years with regards to the improvement of gas turbines overall efficiency. Most common methods include regeneration, intercooling and reheating [2].

Regeneration implies the altering of the gas turbine cycle by introducing a heat exchanger or a recuperator. The main role of the recuperator is to capture the heat from the exhaust gas and use it for the heating of the compressed air. Then, the compressed pre-heated air enters the combustion chamber. Studies regarding this cycle optimization method have been made concerning its feasibility with respect to industrial gas turbines, concluding that, although it provides an improved efficiency by more than 5%, its implementation is relying on the development of modern ceramic-composite heat exchanger configurations [3]. In the second part of the 1900s A. C. Peterson [4] and H. N. Lockwood [5] proposed different regeneration systems that were aiming to improve the overall efficiency of gas turbines, reduce noise levels compared to existing systems and ensure better control over the combustion process.

A great percentage of the power developed by gas turbines is needed by the compressor, as the work required by the compression process is high. In order to reduce the work needed for the compression, this process could be done in two different stages (low pressure compression and high pressure compression) that

---

are provided with an intercooler between them in order to increase the efficiency of the process. This method, namely the intercooling method, can exceed the efficiency of the classic Brayton gas turbine cycle with over 7% [6]. Reheating is another method mentioned used for the purpose of improving gas turbine's efficiency. This method implies using a high pressure turbine and a low pressure turbine with a reheater between them. Usually, the high pressure turbine is used to drive the compressor, while the low pressure turbine provides only useful power output [7]. Recent studies combine the two methods in attempt to generate a greater amount of power. In addition to having a thermodynamic cycle that combines the two methods, various researchers also include new elements into the cycle, such as the conversion of the exhaust CO_2 into methane that can be used as additional fuel [8] or the testing of various coolants (steam compared to ammonia-water mixture [9]). For the development and optimization of such innovative associations heat transfer investigations are required.

Due to the fact that for most gas turbine power plants a considerable share of the power developed is used to drive the compressor, gas turbines present low thermal efficiency. This can be improved by increasing the temperature of the gas entering the turbine. The major disadvantage of such an approach is that high temperatures might cause serious damage to the turbine's blades, as these temperatures might be above the permissible limit for the used materials. In order to prevent this, internal cooling is a well-known developed solution, that implies the existance of cooling passages for turbine blades and vanes [10]. Current state of the art provides a large number of studies regarding heat transfer for such geometries in order to predict the impact different cooling passages have, as their configuration and placement can influence their positive impact on the blade's temperature [11]. Given the costs and efforts necessary to manufacture turbine blades with such cooling passages, the utility of computational fluid dynamics (CFD) methods for the ascertaiment of the heat transfer phenomenon in the mentioned configurations and their influence on the flow inside the turbine was promovated since the 1990s [12].

In paper [13], Popescu et al. compare two configurations for the blade cooling passages, focusing on evaluating which solution is better suited for applications inside the stator blade of gas turbines. Authors' research concluded that the second solution, with three holes, has a superior efficiency to the other analyzed geometry, while also offering better distribution of temperature in the stator wall. One important observation the authors make in order to further improve the selected solution is that the diameter of the third hole is not big enough and it needs a higher mass flow or a lower temperature for the coolant. The investigated geometries are illustrated in figure 1.
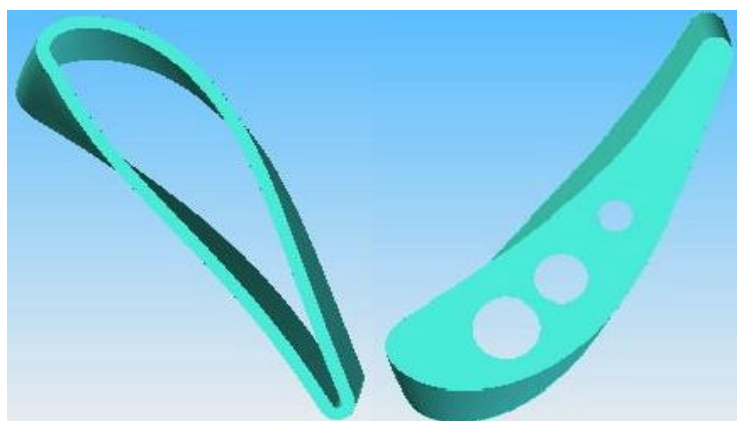

Fig. 1. Stator blade solutions from [13]

Another study regarding internal cooling of turbine blades is conducted by Moskalenko et al. in paper [14]. The research is directed at the influence of nine internal cooling channels for the stator blade. The diameter of these channels varies from the leading edge to the trailing edge. For the analytical investigation the Fluent component of the ANSYS software was employed. The emphasis of the paper was on the determination of the heat transfer coefficient from the cooling channel wall to the coolant. The article concluded that the obtained data was in good agreement with results from experimental campaigns, confirming that CFD simulations represent a powerful tool for the investigation of heat transfer in turbomachinery, in order to further optimize and develop such mechanisms. In figure 2 the investigated geometry is presented, whereas in figure 3 the dependency between the average temperature of the blade and the coolant's temperature is illustrated. Two types of coolant were considered in [14], namely air and water vapor, concluding that steam can be a more efficient coolant than air.
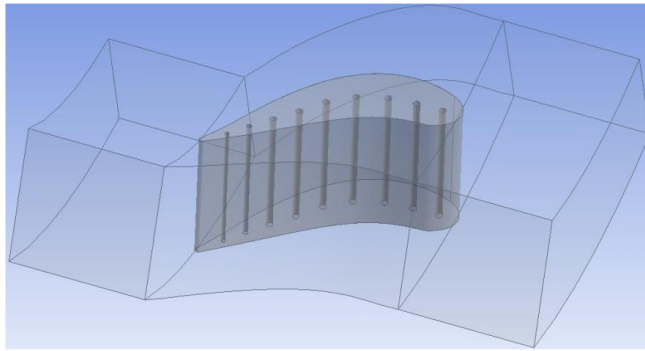
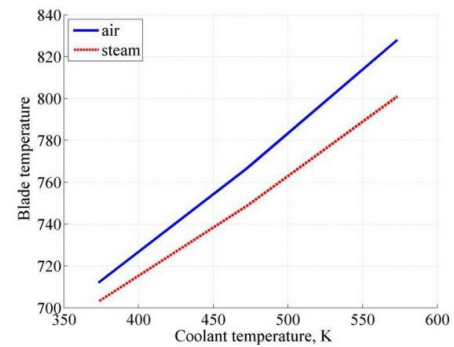**Fig. 2 Geometry model from [14]**

Fig. 3 Average temperature of the blade and cooland temperature dependency [14]

In order to correctly implement internal cooling solutions for the turbine's blades, Wright et al. highlight in [15] the importance of heat transfer evaluation in turbines. By assessing heat transfer behavior one can improve the configuration of the internal cooling channels.

2. THEORETICAL MODEL DESIGN

This paper aims to analyze the heat transfer on the first turbine stage of the MTI-1500 experimental turbine engine. The values of interest regarding the engine will be presented later in the paper. The turbine stage consists of 30 guide vanes and 61 rotor blades. Figure 4 shows the geometry of the guide vanes and rotor blades.
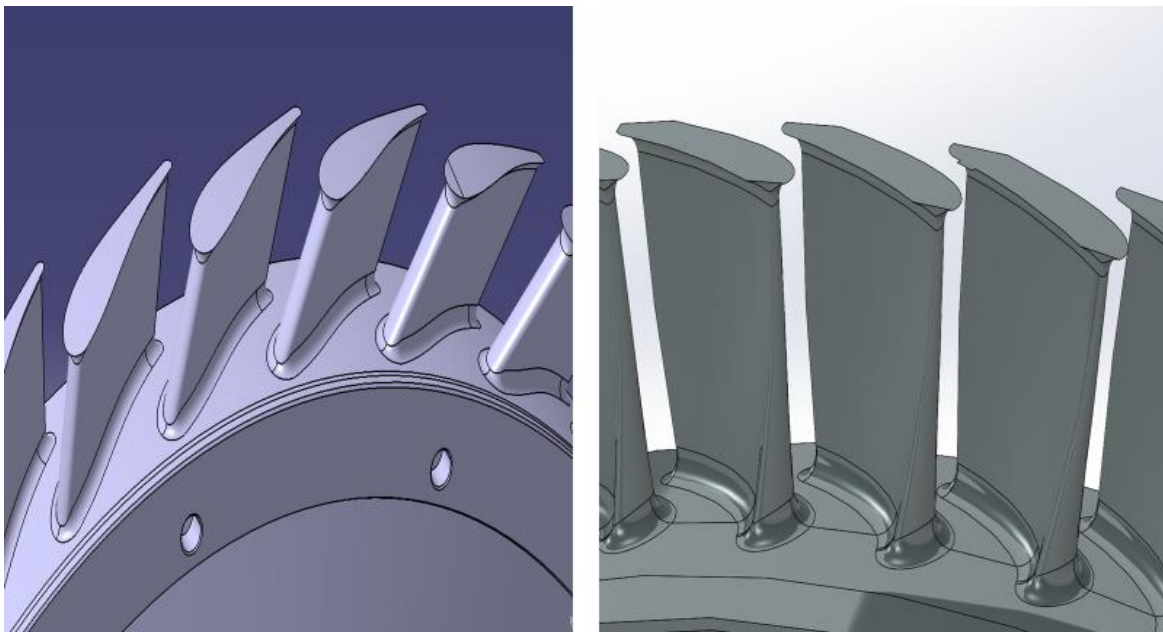
Fig. 4 Turbine guide vanes and rotor blades

The cooling of the rotor blade will be done using two variable cross section channels. The cross section of the channels are placed at 5%, 20%, 35% and respectively 50% of the axial chord of the 10 cross sections of the rotor blade. The cross sections and the geometry of the cooling channles inside the rotor blade can be observed in figure 5. The cooling channels have a diameter of 1mm and their cross sections are placed equidistant from pressure side and suction side.
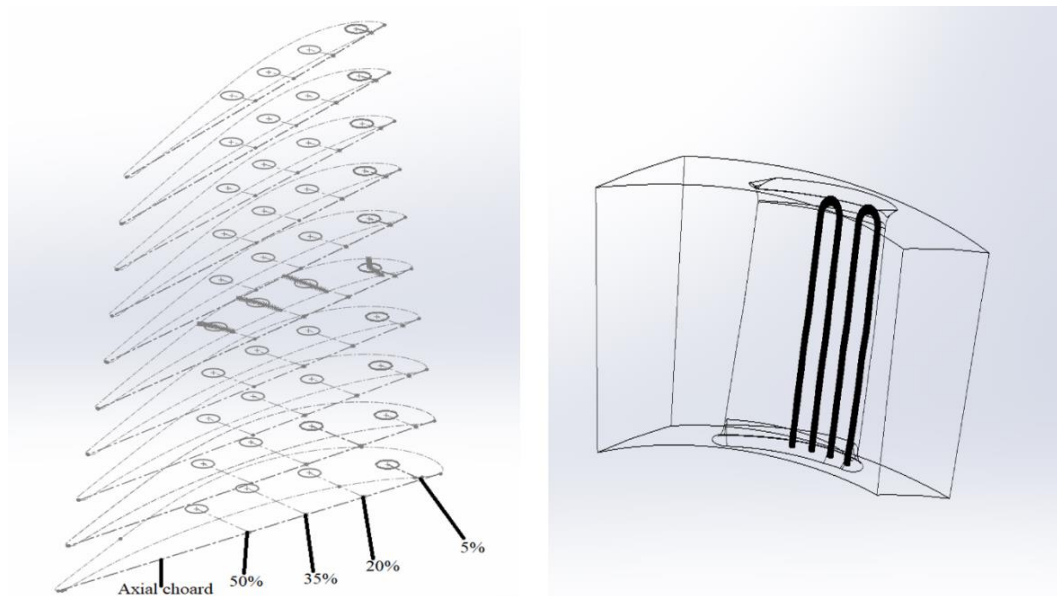
Fig. 5 Cross sections of the rotor blade and cooling channels

The percentage values were chosen based on the theory presented in [10], where the distribution of heat flux on the airfoil surface is explained in detail. In figure 6, the heat flux distribution over the airfoil surface of the rotor blade is presented. It can be observed that the heat flux reaches it's highest values in the 0-50% of the axial chord zone.
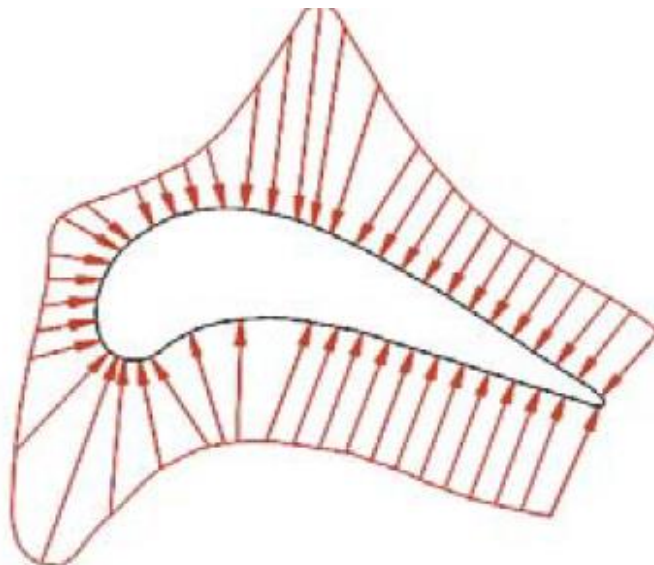

Fig. 6 Heat flux distribution over the surface of a rotor blade[1]

3. NUMERICAL CALCULATIONS

As it was mentioned before, the subject of this paper is to analyze a different cooling method than the ones presented earlier. The numerical investigation involved varying the cooling mass flow, from 0% of the gas mass flow to 1% of the gas mass flow. As a result, a number of four numerical simulations were conducted, with the cooling mass flow of 0%, 0.25%, 0.5% and respectively 1% of the gas mass flow. The numerical domains alongside the boundary conditions are presented in figure 7. The software used in order to perform these numerical calculations is ANSYS CFX.
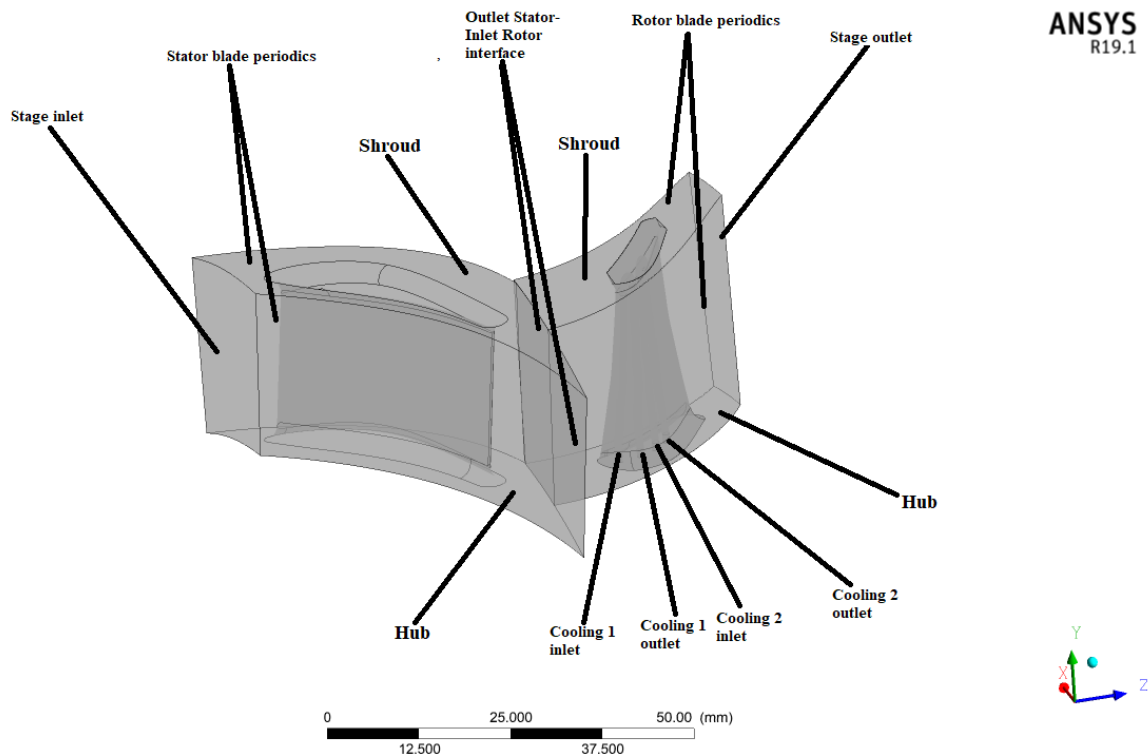
Fig. 7 Numerical domains and the boundary conditions

The boundary conditions are as follows:
Inlet conditions:
- T_{sf} for stator domain: 1263 K
- T_{sf} for each cooling domain: 620 K
- p_{rel} for stator domain: 0 bar
- p_{rel} for each cooling domain: 0bar

Outlet conditions:
- $\dot{m}$ for the turbine stage: 8.1kg/s
- $\dot{m}$ for each cooling domain: 0, 0.000322, 0.000644, 0.001288 kg/s

Wall conditions :
- No slip wall
- Adiabatic wall

Other conditions:
- p_{ref} for the turbine stage: 10.2 barA
- p_{ref} for each cooling domain: 10.2 barA
- Working fluid for all domains: Air ideal gas
- n for the rotor domain: 22000 rev/min
- n for each cooling domain: 22000 rev/min

This simulation is a steady-state simulation with the material chosen for the solid domain, the rotor blade itself, is Nickel with the proprieties from ANSYS material library. The thermal radiation was neglected. Between the solid domain and the fluid domains, the flow domain of the stage and the internal cooling domains, interfaces have been created in order to perform the heat tranfer. The only regions that have the boundary condition set as "WALL" are the hub and shroud regions. A number of 1103 iterations were performed for each one of the cases. The turbulence model used for this simulation is k-ε. The numerical grid used is unstructured, made of tetrahedra having a number of 8243523 elements for all the domains. Because of the limitations imposed by the proccesing power the boundary layer influence was not taken into account for this study, furthermore there has been no inflation created near the wall, thus the y+ value specific for the chosen turbulance model has not been achieved. The numerical gird is presented in figure 8.
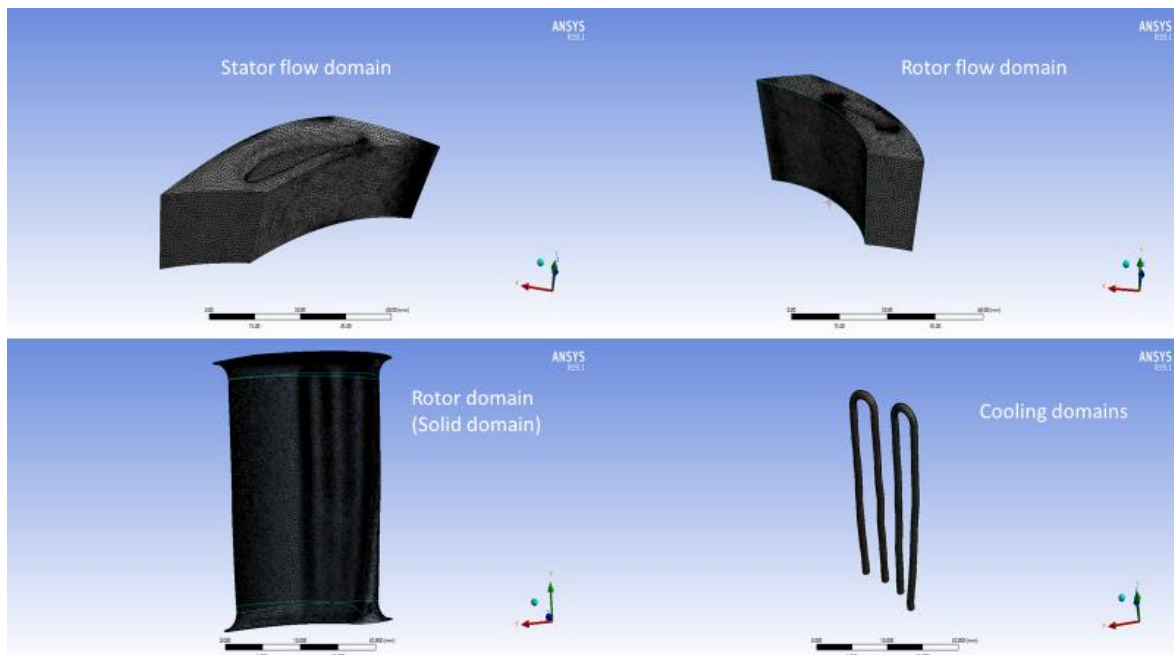
Fig.8 Numerical grid

For a better visualization of the heat transfer inside the rotor blade, a number of 12 temperature measuring points ware created for each section of the cooling domain. The points distribution can be seen in figure 9.
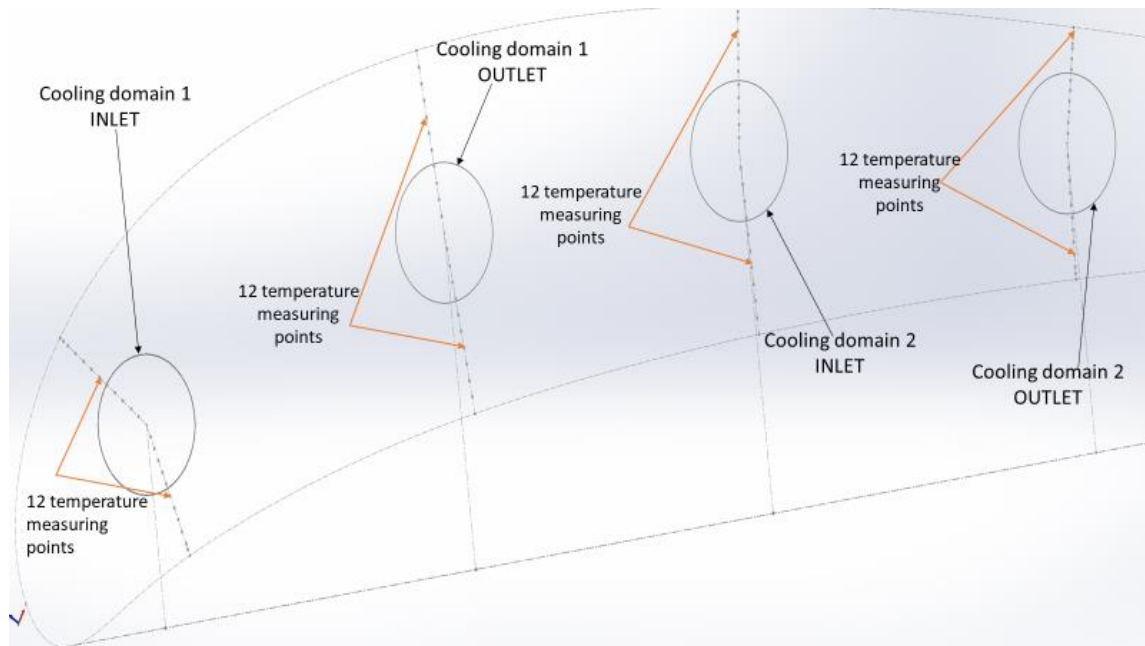

Fig. 9 Distribution of the temperature measuring points

3.1 Numerical results and discussion

The results of interest for this kind of analysis are the blade temperature, the variation of the cooling fluid temperature and the temperature captured by the twelve measuring points. In the following rows the results of interest will be presented and discussed.

When it comes to heat transfer in gas turbines, the most important parameter is the blade temperature. In figure 10, the maximum, minimum and average temperature of the rotor blade for each one of the four cases that were studied in this paper are presented.

As it can be observed in figure 10, the results are theoretically consistent because all three temperatures drop. It can be seen that the maximum temperature increses from 1174.99 K to 1176.5 K. The reason for that can be due to a numerical error or it can mean that with this particular cooling method for this particular gas turbine blade, the maximum temperature cannot drop anymore. This observation can be studied in a future paper. The graph presented in figure 9 can be very helpful if an estimation of the three temperatures for any percentage included in this paper's range [0%, 1%] is wanted.
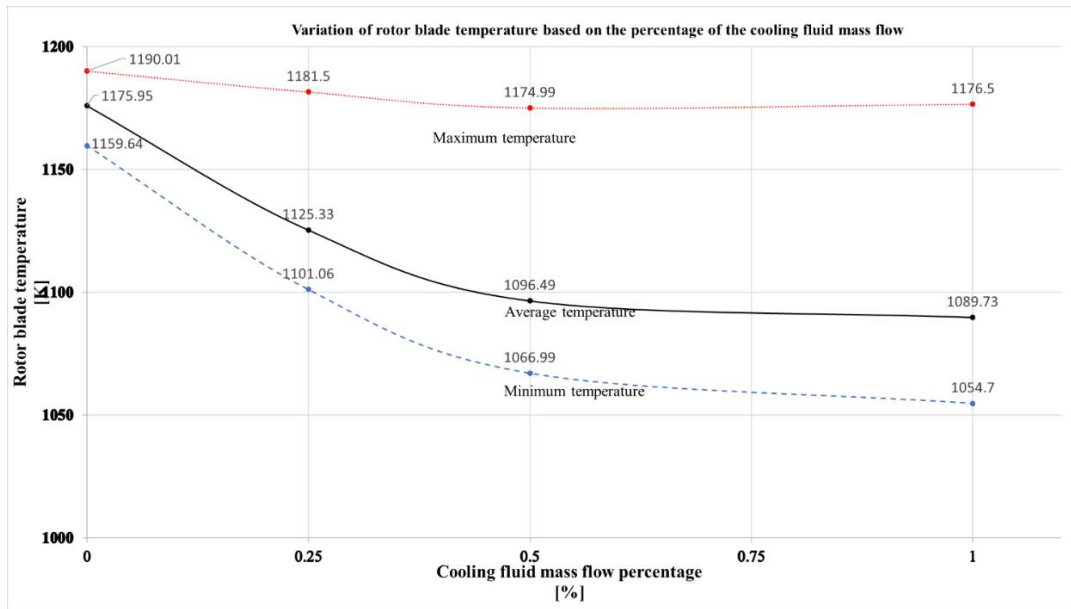

Fig.10 Variation of rotor blade temperature

Another interesting result is the variation of the cooling fluid temperature for each cooling domain, ΔT_1, ΔT_2. This results can be found in table 1 and figure 11. In figure 11 it is presented the coolant temperature inside the blade for the 0.000322 kg/s and 0.000644 kg/s cases.

Table 1. Variation of the cooling fluid temperature

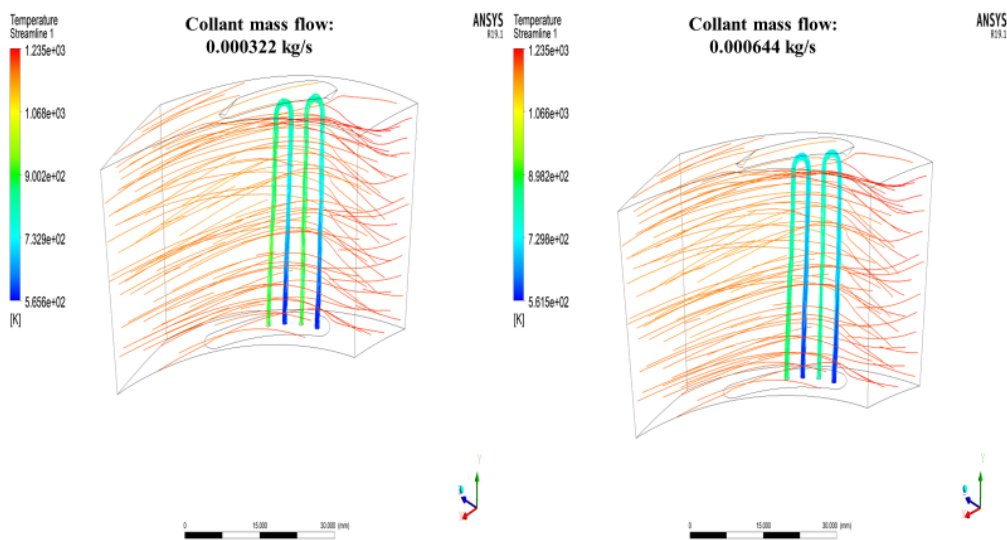| Cooling domain mass flow [kg/s]	ΔT_1	ΔT_2
0.000322	340.848	350.448
0.000644	277.181	289.825
0.001288	286.311	288.802

Fig.11 Temperature of the coolang inside the rotor blade

As it was expected, the cooling fluid absorbed heat from the rotor blade. These values can be improved with the change of the cooling geometry.

The last result of interest is represented by the variation of the rotor blade's internal temperature. As it was mentioned before, this temperature will be measured using 12 temperature measuring points. Because the variation from one point to another is very small, only the average temperature for these 12 points is presented (table 2).

Table 2. Average temperature of the 12 temperature measuring points for the mean radius

Cooling domain mass flow [kg/s]	Average temperature inlet 1 [K]	Average temperature outlet 1 [K]	Average temperature inlet 2 [K]	Average temperature outlet 1 [K]
0	1173.3	1172.5	1172.5	1172.6
0.000322	1104.9	1108.7	1111.5	1125.7
0.000644	1069.4	1072.3	1075.2	1094.9
0.001288	1060.1	1064.7	1068.8	1089.4

From table 2, it can be concluded that the heat transfer inside the rotor blade is done in accordance with the theory regarding heat transfer inside a solid body. It is important to mention that the temperature measurements using the 12 points were done for the mean radius. Because the variation of the temperature from one point to another is very small, a graphic representing the variation of the measured temperature has been done. The graphic represents the variation of the temperature for the case with de cooling domain mass flow equal to 0.001288 kg/s.
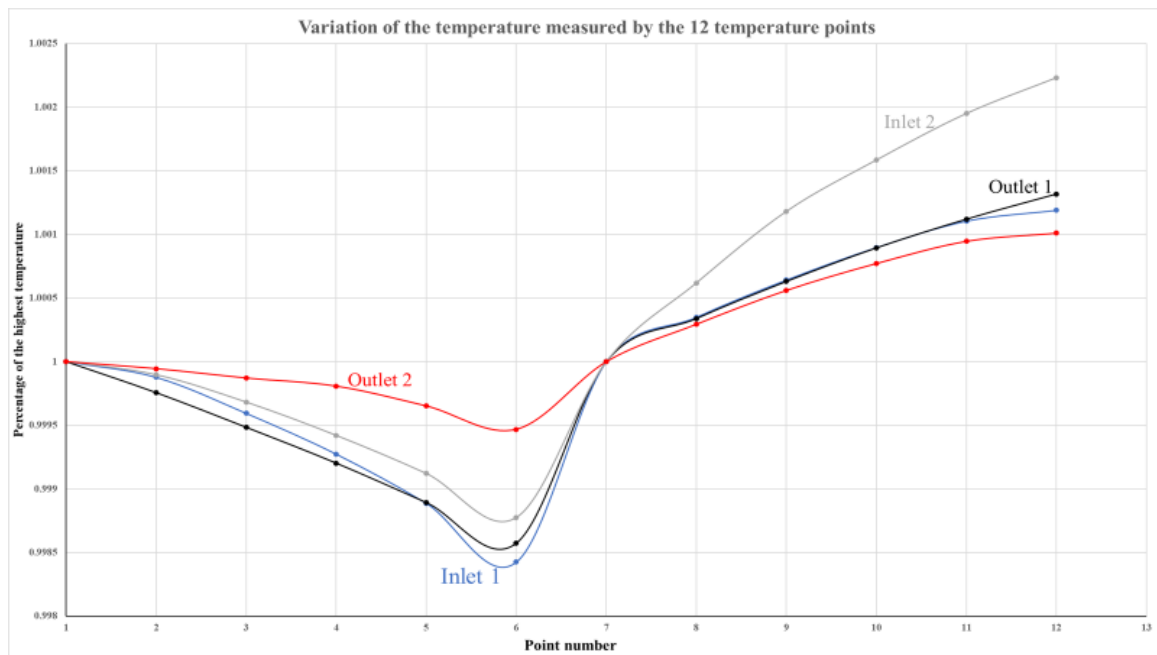

Fig. 12 Variation of the temperature measured by the 12 temperature points

As it can be observed from figure 12, the y axis represents the ratio between the first value of the temperature, which is measured by the first temperature point of each side. The reference temperatures for the four sections presented in figure 10 are as follow:

- Inlet 1, first half, $T_{ref} = 1060.87$K
- Inlet 1, second half, $T_{ref} = 1059.65$K
- Inlet 2, first half, $T_{ref} = 1069.95$K
- Inlet 2, second half, $T_{ref} = 1066.85$K
- Outlet 1, first half, $T_{ref} = 1066.05$K
- Outlet 1, second half, $T_{ref} = 1063.26$K
- Outlet 2, first half, $T_{ref} = 1089.92$K
- Outlet 2, second half, $T_{ref} = 1088.53$K

4. CONCLUSIONS

In this paper was presented a cooling method of a axial turbine rotor blade using the numerical calculation of CFD type was presented. The rotor blade temperature was obtained. By modifying one parameter, the coolant mass flow, the variation of the rotor blade temperature was achived. An interesting addition to this case will be a cooling study based on the performance of this turbine stage. Before that, a study on the heat transfer was needed to see if the methodology presented in this paper is viable.

For future work, a study can be conducted in order to determine which cooling geometry is the best for this particular gas turbine stage. A fluid-structural interaction case will definitely be made to determine if the blade will resist to the applied stress.

ACKNOWLEDGEMENT

REFERENCES

[1]. Filippov S. P., Dilman M. D., Ionov M. S.; 2017; Demand of the power industry of Russia for gas turbines: the current state and prospects; *Thermal Engineering*; 64; 829 – 840.
[2]. Espanani R., Ebrahimi S. H., Ziaeimoghadam H. R.; 2013; Efficiency Improvement Methods of Gas Turbines; *Energy and Environmental Engineering*; 2; 34 – 54.
[3]. McDonald C. F., Wilson D. G.; 1996; The utilization of recuperated and regenerated engine cycles for high-efficiency gas turbines in the 21st century; *Applied Thermal Engineering*; 16; 635 – 653.
[4]. Peterson A. C.; 1965; Heat regeneration system for gas turbines; US3079754A.
[5]. Lockwood H. N. Jr.; 1974; Gas turbine regeneration system; US3949548A.
[6]. Sahu M. K., Sanjay; 2017; Thermoeconomic investigation of power utilities: Intercooled recuperated gas turbine cycle featuring cooled turbine blades; *Energy*; 138; 490 – 499.
[7]. Alves M. A. C., Carneiro H. F. F. M., Barbosa J. R., Travieso L. E., Pilidis P., Ramsden K. W.; 2001; An insight on intercooling and reheat gas turbine cycles; *Proceedings of the Institution of Mechanical Engineers, Part A: Journal of Power and Energy*; 215; 163 – 171.
[8]. Khan R., Shukla A. K., Sharma M., Phanden R. K., Mishra S.; 2020; Thermodynamic investigation of intercooled reheat gas turbine combined cycle with carbon capture and methanation; *Materials Today: Proceedings*.
[9]. Maheshwari M., Singh O.; 2020; Thermo-economic analysis of combined cycle configurations with intercooling and reheating; *Energy*; 205.
[10]. Wright L.; 2006; Enhanced Internal Cooling of Turbine Blades and Vanes; *Materials Science*.
[11]. Han J. C., Huh M.; 2009; Recent Studies in Turbine Blade Internal Cooling; *International Centre for Heat and Mass Transfer – Digital Library*.
[12]. Iacovides H., Launder B. E.; 1995; Computational fluid dynamics applied to internal gas-turbine blade cooling: a review; *International Journal of Heat and Fluid Flow*; 16; 454 – 470.
[13]. Popescu V. M., Petcu R, V. Silivestru.; 2007; Simulation of cooled gas turbine stage; *Ansys & Fluent User's Group Meeting*.
[14]. Moskalenko A. B.; Kozhevnikov A. I.; 2016; Estimation of Gas Turbine Blades Cooling Efficiency; *Procedia Engineering*; 150; 61 – 67.
[15]. Wright L. M., Han J. C.; 2015; Heat transfer enhancement for turbine blade internal cooling; *Journal of Enhanced Heat Transfer*; 111 – 140.

ANALISYS OF GAS TURBINE STABILITY AT IDLE AND SUB-IDLE SPEEDS

Razvan NICOARA[1], Cosmin SUCIU[1], Cristian DOBROMIRESCU[1], Madalin DOMBROVSCHI[1], Emilia PRISACARIU[1]

ABSTRACT: As many gas turbines, aviation or industrial gas turbines, operate frequent start and stop cycles, a need to characterise the engine behaviour across a broad range of operating regimes including idle and sub-idle regimes can be identified. This paper studies the dynamic stability of a gas turbine engine at low speeds. Experiments of a gas turbine engine were conducted on a dedicated test rig in order to determine the engine behaviour for a series of idle and sub idle regimes and evolutions. Experimental data results are presented and analyzed. The gas turbine used for this study is an aeroderivative helicopter turboshaft engine with a rated power of 1500 SHP which was modified to run on natural gas. The paper details the experimental installation, test procedure and results as well as the analysis of the parameters variation at different speeds.

KEYWORDS: experimental, start-up, low regimes, turboshaft, gas generator

NOMENCLATURE
CC – Combustion Chamber
EOP – Engine Oil Pressure
EPR – Engine Pressure Ratio (commonly known as OPR - Overall Pressure Ratio)
GGT – Gas Generator Turbine
N1, NGG – Gas generator rotational speed
N2 – Free turbine rotational speed
PT – Power Turbine
SHP – Shaft horse power
T.G.T – Turbine Gas Temperature (sometimes referred to as exhaust gas temperature - E.G.T.)
VB – Vibration level

1. INTRODUCTION

As the energy needs are constantly increasing and the emission gases become an even more pressing problem, the need for clean power generation increases. Thus, a solution used at the moment is the natural gas fired gas turbines and combined cycle power generation plants. Gas turbine power generation represents a suitable solution to be integrated with renewable power sources. As renewable power sources cannot always provide constant power generation, gas turbine can be used to fill the energy needs as they can respond to rapidly changing power demand. Thus, many gas turbines operate frequent start and stop cycles. Therefore, it is very important to identify the engine behaviour across a broad range of operating regimes including idle and sub-idle regimes for safety and fuel economy.

When referring to aviation gas turbine engines, the regime is for most of the time constant, as the engine is operated mostly at higher, more fuel efficient speeds. Nonetheless, rapidly changing regimes are present, thus information about engine performances at different speeds, including low speed regime, are still required. One example of a complex and rapidly changing speed process is the acceleration of a helicopter turboshaft engine which is in a sleeping mode (a sub-idle stabilized regime in which the gas generated is kept

---

by an electric motor, with no combustion). Such flight modes are being proposed for multiengine helicopters in order to reduce the fuel consumption [1].

For gas turbine start-up processes, two systems are required to ensure that the engine will start satisfactorily. Firstly, the compressor-turbine rotor assembly must be rotated to a certain speed to ensure that adequate air passes through the combustion chamber. Secondly, energy must be introduced into the system in order for the fuel-air mixture to ignite. The operations of both systems are automatically controlled. A typical start-up sequence is presented in Fig. 1.
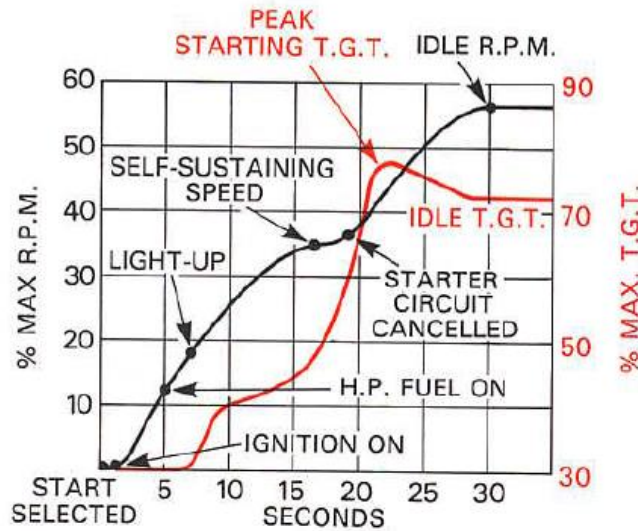
Fig. 1 Typical starting process of a gas turbine engine [2]

It can be deduced, from Fig. 1, that during the starting process a temperature peak is reached and the idle regime is set in order to avoid the high temperature even though the engine is self sustaining at lower speeds. Additional examples of start-up parameters variations are presented in Fig. 2 for TV2-117A and TV3-117MT gas turbine engines.
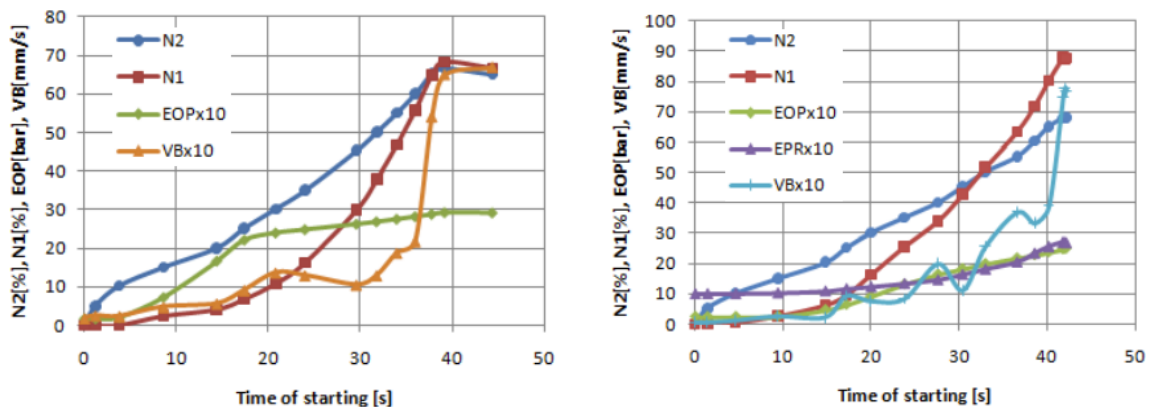

Fig. 2 Variation of TV2-117A, TV3-117MT respectively, engine parameters for a hot run [3]

The command and control of the engine is accomplished by an engine control system which is a closed-loop control system that consists of four types of control components: controller, sensor, execution element and accessory. The purpose of these systems is to achieve the required thrust or shaft power, however due to the reduced feasibility of in flight thrust of shaft power measurements the rotational speed or engine pressure ratio has been effectively used as a mean of controlling engine performances. Thus, the shaft speed becomes the desired output variable, controlled by an actuator position which is a fuel metering valve. The variation of fuel injected in the combustor leads to a specific variation in shaft speed and engine thrust. Feedback from engine sensors (tachometers or pressure transducers) is used to achieve a close-loop system.

A simplified diagram of a shaft speed based control system is presented in Fig. 3. Furthermore, engine pressure ratio or turbine temperature control systems are used.
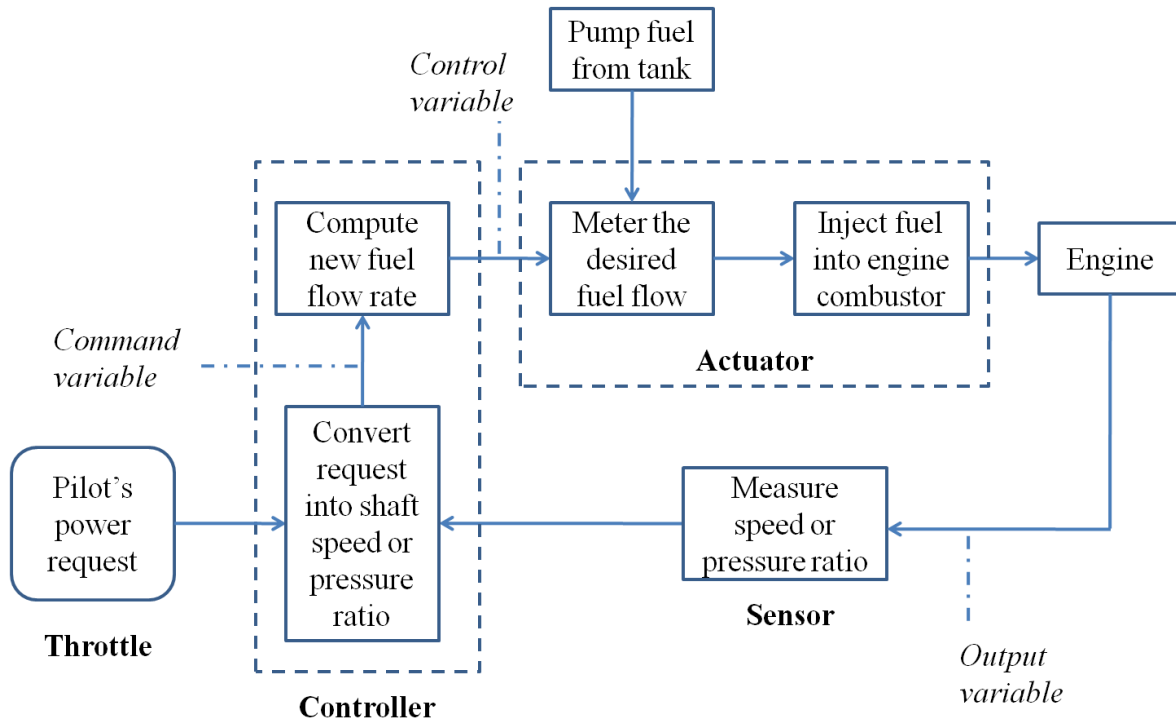

Fig. 3 Diagram of a simplified engine control system (reproduced after [4])

The engine shaft speed is maintained constant by an automatic control system. Most of the time this represents a closed loop where the fuel mass flow injected in the combustion chamber is varied with a value proportional to the difference of the actual speed and the reference speed. The present paper aims to experimentally investigate the stability of this closed loop at sub-idle speeds. Even though the engine performances are a well studied subject, the engine evolutions and performance estimation at sub-idle speed still poses some difficulties due to instabilities, poor reliability of components maps and complex burning processes.

2. EXPERIMENTAL SETUP

The gas turbine engine used for this study is a modified Klimov TV2-117A helicopter engine, with a take-off power rated at approximately 1500 SHP. The engine was modified by the Romanian Research and Development Institute for Gas Turbines COMOTI in order to be fuelled with natural gas. The modified, natural gas fuelled, TV2-117A engine will be referred as TA2.

The experiments were conducted at COMOTI's Gas Turbine Experimentation Complex on a dedicated test rig for aeroderivative turboshaft engines. The test rig is specially equipped to deliver natural gas from the national grid to power the respective engine. A pressure regulator and a diaphragm mass flow meter are used to measure and control the natural gas parameters.

To control the engine regime a signal is sent to a gas fuel dosimeter which controls the injected fuel mass flow rate for different operating regimes. An injection ramp delivers the fuel to the 8 injectors of the gas turbine. A diagram of the experimental installation is presented in Fig. 4. The experimental installation is also equipped with data acquisition control and display system.

The main experimental parameters recorded during testing are presented in Table 1. A more comprehensive description of the experimental test rig is presented in [5].

Table 1. Main parameters recorded during experimental testing [5]

No.	Parameter	Symbol
1	Atmospheric pressure	P0
2	Atmospheric temperature	T0
3	Gas generator speed	NGG
4	Power turbine speed	NTP
5	Compressor exit pressure	P2
6	Compressor exit temperature	T2
7	Medium turbine inlet temperature	T3M
8	Exhaust temperature	T5
9	Natural gas pressure	PGC
10	Fuel flow rate	WF
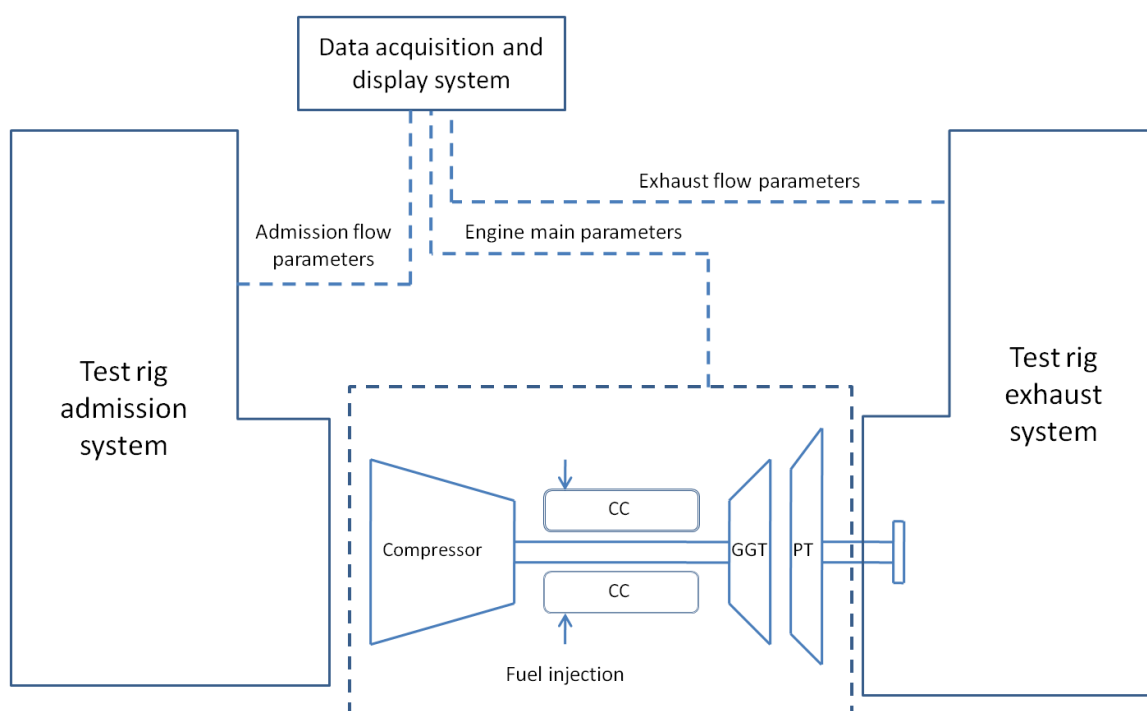
Fig. 4 Experimental installation setup

As can be determined from the experimental setup presented in Fig. 4 the power turbine is not connected to a power consumer. Thus, the power generated during these experiments is null. This development leads to a higher rotational speed of the power turbine and a lower backpressure for the gas generator. This is thought to have a reduced impact on the gas generator evolution as the backpressure for the considered engine regimes is small. Nonetheless, the power turbine speed was closely traced during experimental testing. In Fig. 5 is presented the TA2 engine mounted on the dedicated test rig, capable of providing natural gas as engine fuel. In Fig. 5 can also be identified the electric generator (used as a mechanical power consumer) which is unconnected to the power turbine.

Fig. 5 TA2 engine on test rig

In order to experimentally determine the engine stability at different sub-idle speeds the following test procedure was pursued. The engine was normally started to its idle speed and after a short stabilisation period the reference speed was gradually lowered. From the idle speed, 10500 rpm, which corresponds to a regime of approximately 50%, the engine speed was lowered to 8600 rpm, approximately 40%. During the same experiment a sub-idle acceleration was tested as well as a start-up with to a sub-idle speed. The time-speed variation of this experiment is presented in Fig. 6.
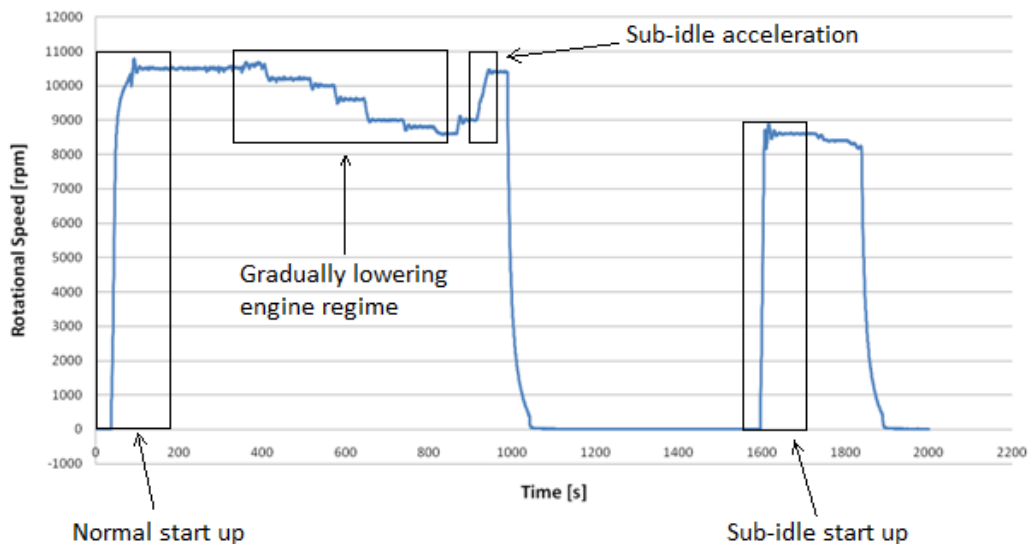
Fig. 6 Shaft speed variation during experimentation

3. EXPERIMENTAL RESULTS AND DISCUSSION

The parameters evolution during a normal start up follows the trends presented in Fig. 1. After the rotor reaches a certain speed, driven by the electrical starter, the fuel is injected and ignited which cause the rapid acceleration of the shaft. The gas generator speed variation during a normal start up is presented in Fig. 7. For easier interpretation the engine parameters are represented in this study reported to their respective value at idle speed. As can be determined from Fig. 7, a constant value of fuel flow is injected at a certain shaft speed which leads to a rapidly increase in temperature. With the shaft speed increase, the mass flow through the engine increases as well, thus the air-fuel ratio increase which leads to a slower rise in temperature. Then, the mass flow follows a linear evolution until close to the idle speed where a few loops can be identified as the command system is used to achieve the required idle speed.
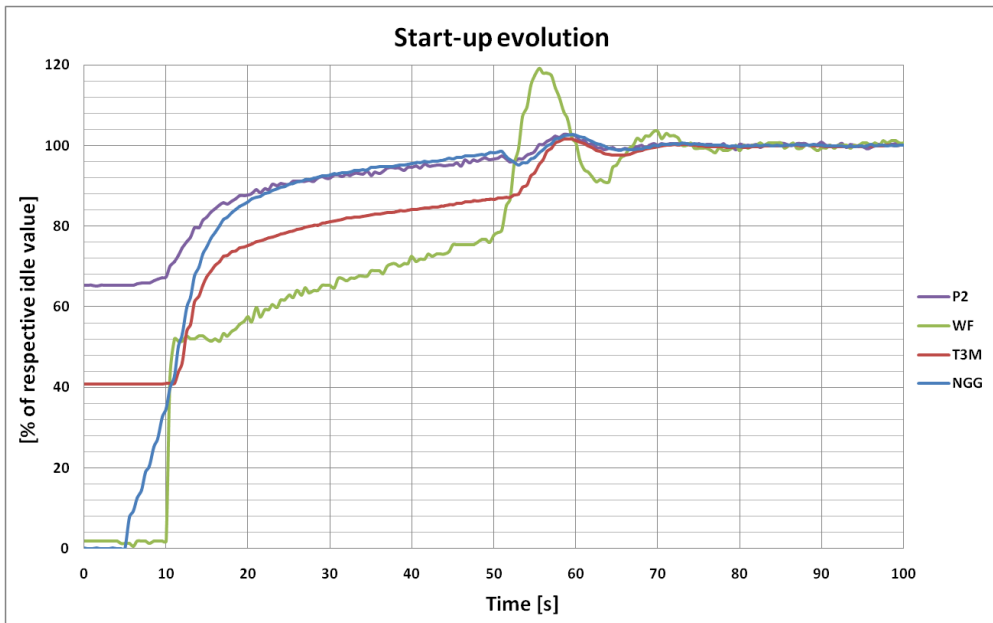
Fig. 7 Parameters variation during a normal start up

Engine regime was reduced in order to test the engine stability. The regime variation was completed, as presented in Fig. 8, by gradually reducing the reference speed with limited steps. With the variation of the reference speed the actual speed decreases and a number of control loops are needed to achieve the respective speed. A slight increase in number and amplitude of the control loops can be identified as the reference speed decreases but once the speed is reached the engine regime is stable.
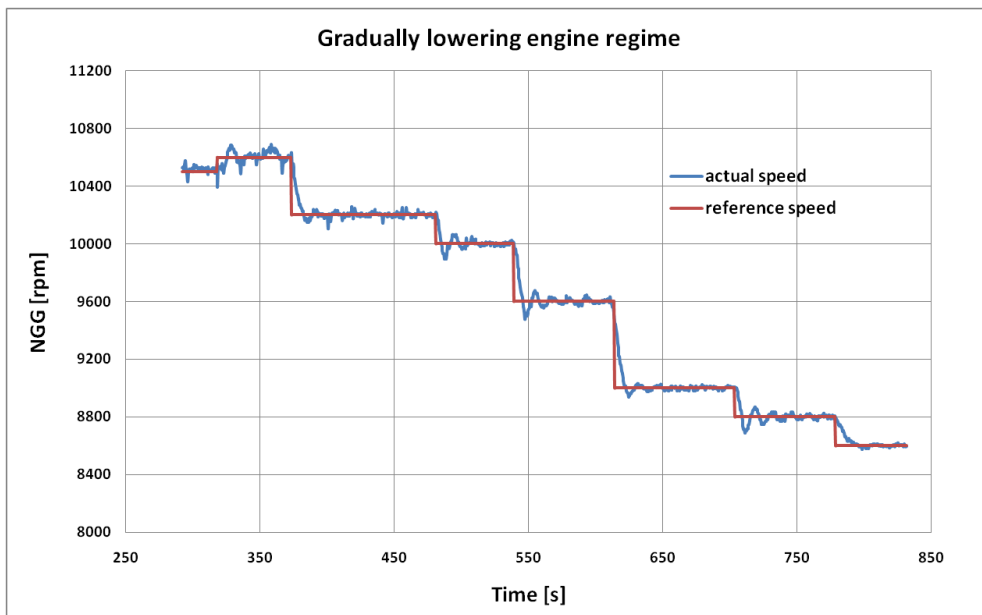
Fig. 8 Shaft speed during engine regime variation

Figure 9 shows the parameters variation with the change of engine regime. The parameters are represented as a percent of their value at idle speed. The engine mass flow decrease determines a decrease in shaft speed which leads to a decrease in compressor exit pressure and engine mass flow. The lower fuel mass flow correlated with a decrease of air mass flow explains the relative constant temperature value of the engine presented in Fig. 9.
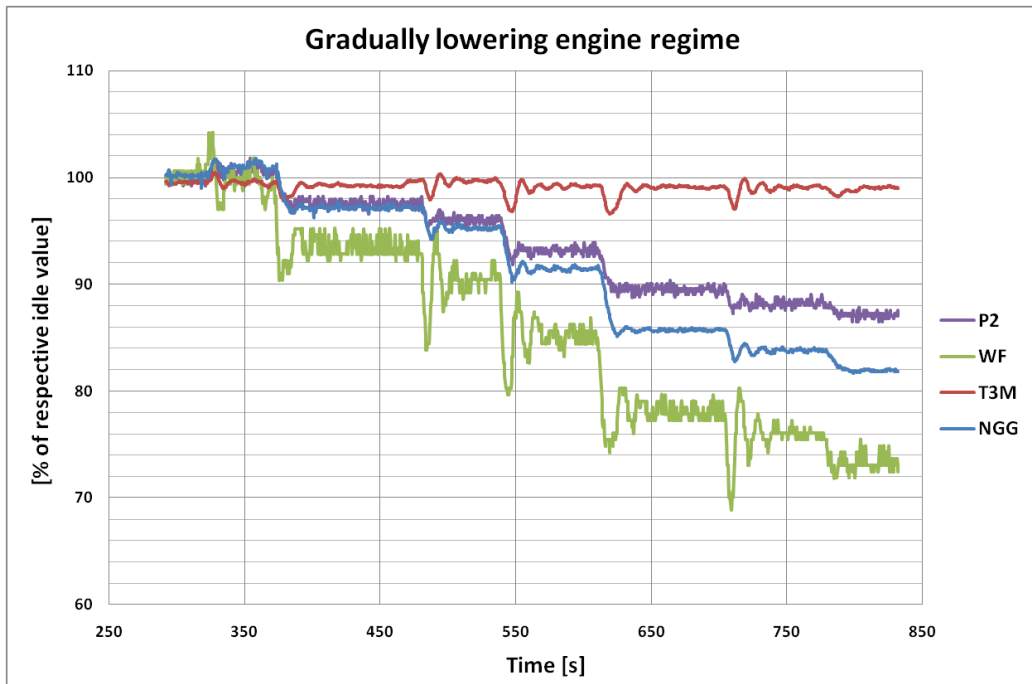
Fig. 9 Engine parameters during engine regime variation

A sub-idle acceleration was tested from a shaft speed of 9000 rpm to 10400 rpm, close to idle speed. In this interval the engine parameters did not show any instability as the speed increase normally. Figure 10 shows the parameters variation during sub-idle acceleration.
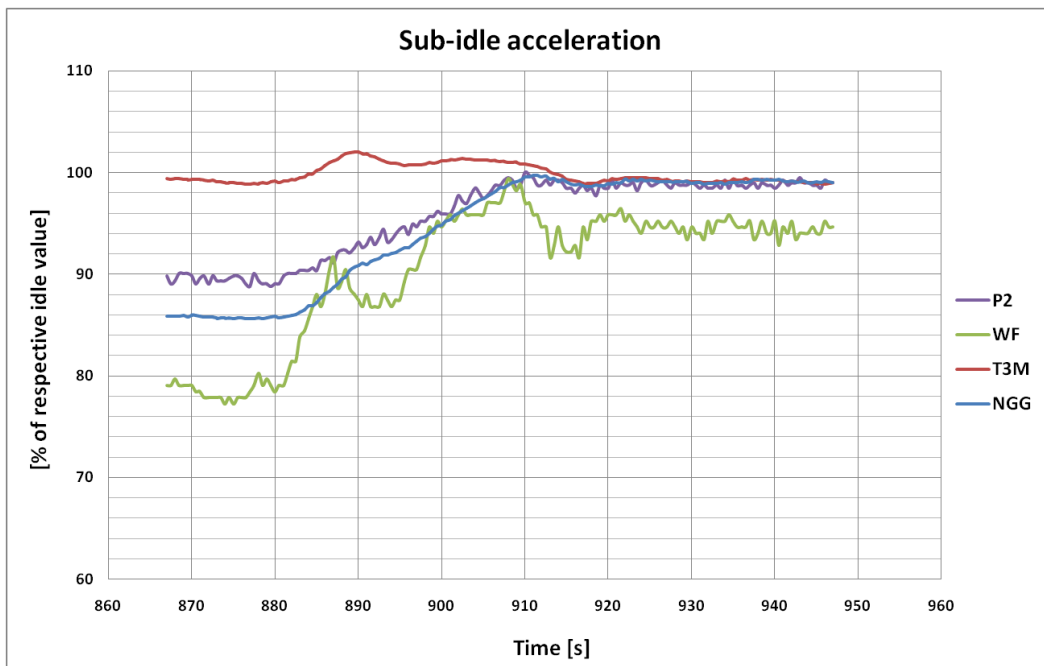
Fig. 10 Engine parameters during engine regime variation

As the engine could be operated at sub-idle speeds, as was previously discussed, a start up process was tested with a lower reference shaft speed. The start up procedure is identical but the reference speed is 8500, down from 10500 rpm. With the lower reference speed more loops were needed to achieve the required speed, as can be determined from Fig. 11 which presents the shaft speed variation for the two start up processes.
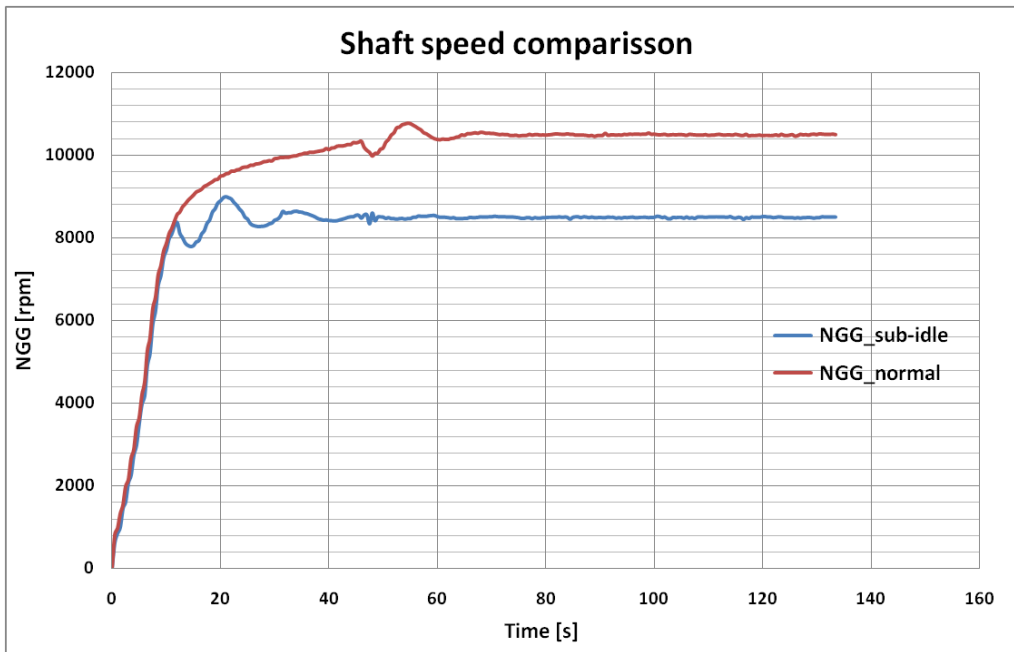
50

Fig. 11 Comparison of shaft speed evolution for two different start ups

The engine parameters variation, determined by the closed loop near the required reference speed, can be determined from the Fig. 12 and Fig. 13 as well, which shows the fuel mass flow and turbine inlet temperature variations. The values of the parameters presented in Fig. 12 and Fig. 13, for both normal and sub-idle start up processes, represents the actual data divided to their respective value at idle (10500 rpm).
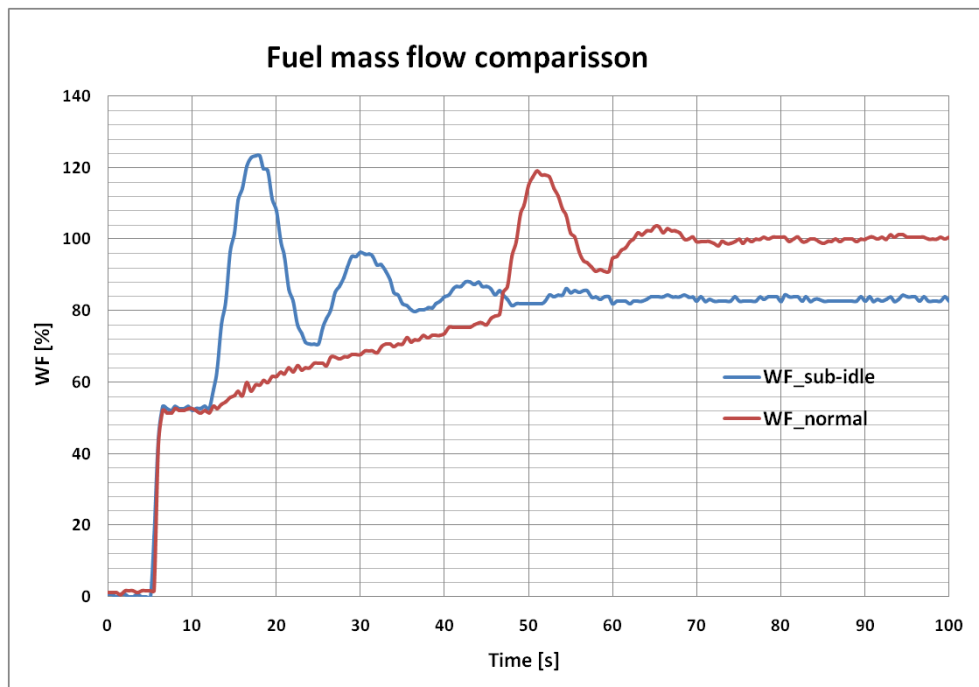

Fig. 12 Comparison of fuel flow evolution for two different start ups

In the first phase of the starting process, a constant value of fuel is injected in the combustion chamber, which is a common element for the two processes studied (as can be determined from Fig. 12). As the shaft speed increases, in the normal procedure, a linear phase follows and finally the mass flow calibration for the respective reference speed. For the sub-idle reference speed the linear phase is no longer present and the fuel flow calibration for the respective speed determines a sharp increase fuel flow which

leads to a sharp increase in temperature, as can be determined from Fig. 13. After the reference speed is achieved the regime becomes stable.
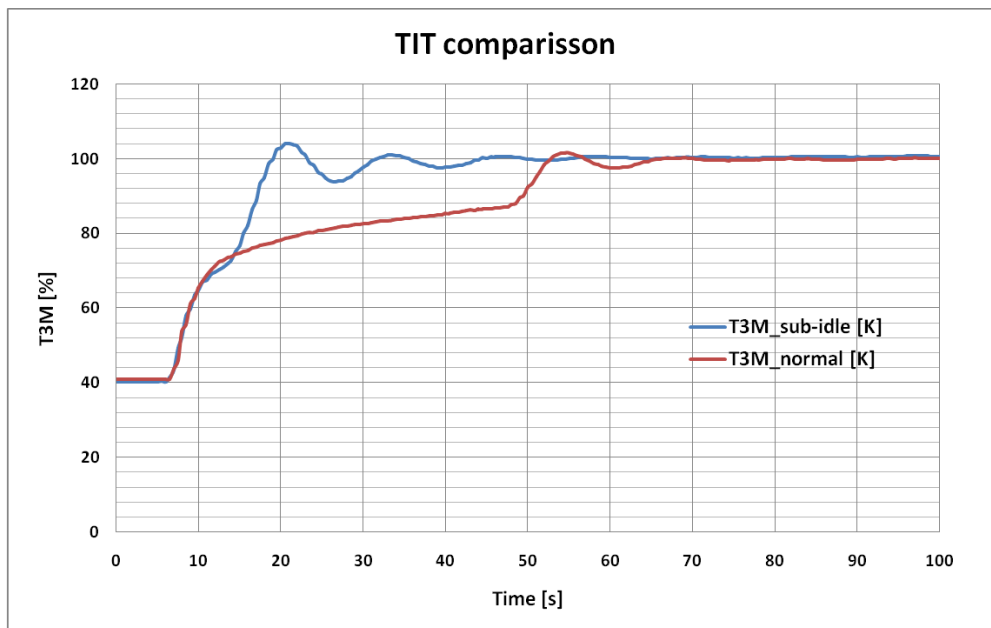

Fig. 13 Comparison of turbine inlet temperature evolution for two different start ups

4. CONCLUSIONS

The present paper discusses the engine stability at idle and sub idle speeds. Experimental data was gathered from tests performed on an aeroderivative engine. The paper also presents the experimental installation. Relevant data for sub-idle speeds was obtained by performing a normal start up procedure and then gradually lowering the regime. A sub-idle acceleration was performed on a limited interval as well as a sub-idle start up process.

The result showed that the engine achieved dynamic stability at the tested speeds; a slight increase in number and amplitude of the control loops was identified as the reference speed decreases but once the speed is reached the engine regime is stable. From the sub-idle acceleration analyses resulted that a normal variation of the parameters occurs. This result may be influenced by the limited interval for which the acceleration was performed.

In the case of sub-idle start up, important differences resulted from data analysis when compared to a normal start up. Both processes followed the same starting procedure but with different reference speeds. It was determined that the sub-idle start up process lacked the linear, slow acceleration phase, this phase being replaced by an abrupt acceleration which leads to a sharp increase in turbine inlet temperature. Also, more control loops were needed to reach the required speed. The engine achieves dynamic stability once the reference speed is reached.

When analysing the present paper results it is important to remember that the data, on which this study is based, was obtained from an engine which is powered by natural gas. In case of other fuels, especially liquid fuels, important differences may occur. These differences can be related to specific heat values, air-fuel mixtures and vaporisation processes.

Future work should concentrate on determining the engine emissions variation at sub-idle speeds, vibration analysis and acceleration response times. A sub-idle acceleration should be conducted on a larger speed interval. Furthermore, the influence of power extraction on gas generator evolution should be investigated at the respective low engine regimes.

REFERENCES

[1] Ferrand, A, Bellenoue, M, Bertin, Y, Cirligeanu, R, Marconi, P, & Mercier-Calvairac, F. "High Fidelity Modeling of the Acceleration of a Turboshaft Engine During a Restart." *Proceedings of the ASME Turbo Expo 2018: Turbomachinery Technical Conference and Exposition. Volume 1: Aircraft Engine; Fans and Blowers; Marine*. Oslo, Norway. June 11–15, 2018. V001T01A034. ASME, https://doi.org/10.1115/GT2018-76654;

[2] Rolls-Royce plc (United Kingdom), 1986, "*The jet engine*", 5 ed., Reprinted 1996 with revisions, ISBN 0-902121-2-35, page 121;

[3] Razvan Marius, Catana & Fuiorea, Ion. (2019). DEVELOPING STARTING PROGRAMMES OF GAS TURBINE ENGINES INTO A TEST BENCH", U.P.B. Scientific Bulletin, Series D, Vol. 81, Issue 2, 2019;

[4] Jaw, L.C.; Mattingly, J.D., *Aircraft Engine Controls*, American Institute of Aeronautics and Astronautics, NewYork, NY, USA, 2009; ISBN 978-1-60086-705;

[6] Vilag J., Stanciu V., Vilag V., Cuciumita C. (2013). *Experimental setup for gas turbines operating on alternative gas fuels,* U.P.B. Scientific Bulletin, Series D, Vol. 75, Issue 3, 2013 ISSN 1454-2358.

SUPERSONIC PLANAR TURBINE CASCADE TEST BENCH

Cosmin Petru SUCIU[1], Cleopatra Florentina CUCIUMITA[1]**, Răzvan Edmond NICOARĂ**[1]**, Mădălin DOMBROVSCHI**[1]

ABSTRACT: Considering the growing interest in reusable rockets and rocket engines, making a versatile supersonic turbine for the turbopump assembly is a necessary advancement for the industry. This paper presents an experimental test bench for a planar supersonic turbine cascade like the ones used in turbopumps for launchers with payloads of up to 200 kg. Schematics with the data acquisition and test bench components are presented. A set of measured parameters are added to show that the proposed objectives of the experimental test bench have been met. An analysis of the measurement uncertainty for the parameters of interest is also included.

1. INTRODUCTION

Space travel is heading towards a more sustainable and economical structure. Both government agencies and start-up companies expressed growing interest in reusable launchers. At the same time, space programs started to look into alternative fuels, exploring more environmental friendly, economical and widely available options. Therefore, rocket engines should be more versatile and more reliable, allowing multiple use and different working fluids.

One of the important components in a rocket engine is the turbopump, which has the role of delivering fuel and/or oxidizer from the tanks to the thrust chamber at high pressures and as quickly as possible. It consists of two major components: a turbine and a rotodynamic pump. Supersonic turbines are preferred for such applications as they can produce a higher specific work output. The efficiency of such a turbine is lower than that of conventional turbines, around 50-60% [1]. Nevertheless, the advantages of being lighter and having high specific work output at low mass flow rates outweigh the efficiency disadvantage if used in the rocket industry. The rocket engines requirement of being more versatile and reliable transfers to its components in general, and to the turbine, in particular.

Lee et al have tested a single rotor supersonic impulse turbine with 12 guide vanes [2]. The test was performed with air gas instead of flue gasses. The obtained results showed the highest efficiency at design point.

With the need of developing new turbines, comes the need of testing them for performance validation for different working fluids. In response to this need, a new test rig was built and presented here. This test bench that can accommodate a planar stage of a turbine (stator and rotor) suitable for launchers that can carry a payload of up to 200kg into LEO (Lower Earth Orbit). Detailed measurements of the turbine can be performed, including: mass flow rate measurements, pressure distribution along the guide vanes flow channels, total pressure and Mach number in the section between the stator and the rotor and gas total temperature. The test rig is also equipped with the required devices for controlling the flow regime.

A detailed description of the test rig, along with an example of a test article and the instrumentation required for analysing the flow characteristics is given in the following. An analysis of the uncertainty of measurement for the mass flow rate and the pressures is also presented. A set of experimental data is given with the purpose of demonstrating the test rig capabilities.

---

[1] Romanian Research and Development Institute for Gas Turbines COMOTI, Bucharest, Romania

2. EXPERIMENTAL TEST BENCH

2.1. Test article description

The testing assembly was modelled keeping in mind the main objectives of measurements (characterising the flow within the turbine) and the limitations of the test rig:

• Absolute Pressure 5bar
• Test different types of working fluids
• Possibility of taking measurements of mass flow rate, pressure (stagnation and static) and temperature (stagnation).

After a thorough analysis of the objectives presented above, we have established a few guidelines to respect during the design process:

1. The airflow domain has to be properly sealed in order to be able to keep the pressure constant.
2. Possibility of mass flow rate measurement.
3. Possibility of static pressure measurements near the rotor and stator canals, as well as in the inlet and outlet section of the domain.
4. Possibility of stagnation pressure measurement after the stator critical section, inside the supersonic flow.
5. Possibility of taking total temperature measurements of the working fluid.
6. Possibility to adapt the measurement probes positions without affecting the overall design.
7. Accurately predict Mach number.

The 3D modelling was done using Solidworks CAD software. At first, we have created the geometry of the air flow domain. The domain has an axial inlet and a tangential outlet that will allow the air to expand freely. Four different channels for the stator blades were chosen to be studied. For the rotor blades, the equivalent was 6 channels. The domain height was chosen to be 10mm, to meet the area requirements for the application and have a minimum technological height. The walls near the stator and rotor were modelled according to the pressure side and suction side of the blades. After the domain was properly constrained, we modelled the testing assembly.
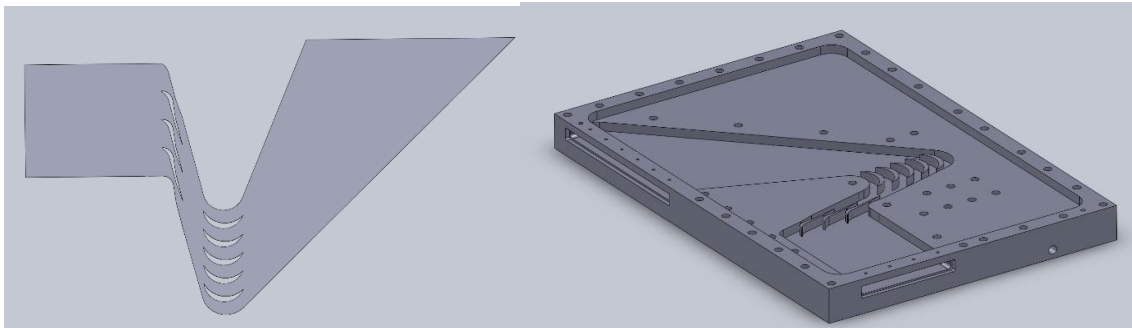

Fig. 1 Air flow domain (left); Plate assembly (right)

A semi-finished 520x360x40mm plate was used for the airflow domain. Because of the small dimensions of the stator blades, they were machined directly within the domain. The next step was to create two pockets for the inlet and outlet sections, (Fig. 1). The domain sealing was ensured with a cover plate and mastic sealant. Another pocket at the top of the domain was modelled in order to create the sealing surfaces for the cover plate. Because of machining constraints, the margins of the plate are 20mm wide and contain screw clearance holes that will allow the cover to be mounted tight on the plate. Also, M6 screw holes were placed near the channel to ensure that the pressure inside will not deform the cover and affect the sealing.

The cover lid was modelled to fit perfectly over the airflow domain and the margins of the plate. Another pocket was created in the area of interest for pressure measurements (above the blades) in order to allow a second lid to be mounted for placing the instrumentation probes. This second lid simplifies the assembly, and creates the possibility to adapt the measurement points more easily, without changing the whole design. Fig 2 presents how the lids are assembled to the main plate and the static pressure probes position. The position for the static pressure probes was selected to be just above the two middle stator flow channels. Multiple probes were mounted along the flow channels for multiple points measurement. The lower part of the lid contains five 0.3mm holes for each stator channel, concentric with the pressure probe holes (Fig 2 right).
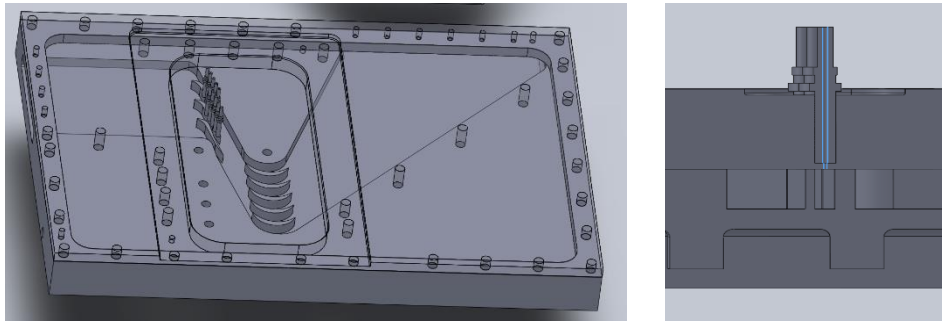
Fig. 2 Test article assembly(left) ; Static pressure probes (right)

After the manufacturing process, laser measurements were conducted on the plate to assess the production results. The results presented in Fig 3 show a deformation of the plate. The plate was fitted on the CNC with 4 clamping jaws (2 on the inlet side and 2 on the opposite side). The plate has gained stress during the milling processes. After the removal of the clamping jaws, the plate bent into a concave form. In Figure 3 we can see that on the sides, the biggest difference is about 0.5mm, whereas on the middle the difference is of -0.475mm. This affects the position of the bolts that centre the instrumentation cover and the position of the pressure probes.
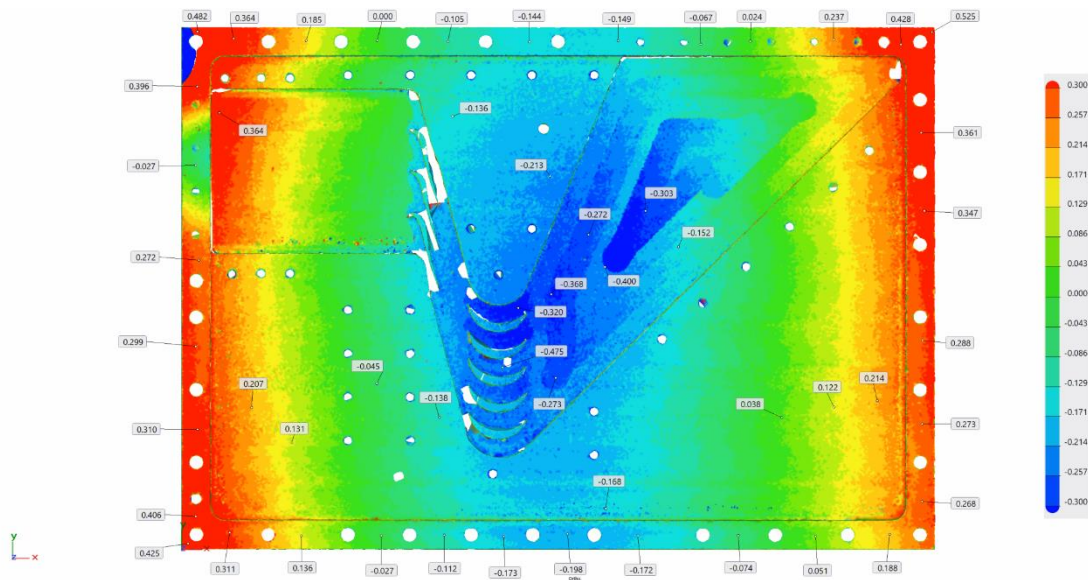
Fig. 3 Plate assembly laser measurement

To overcome this, a stand (bed) was crated on which the plate was mounted and pressed tight. The screws on the sides of the plate were used to mount it on the stand, similarly to the way it was mounted on the CNC.

2.2. Mounting device for Aeroprobe 5-Hole

Due to the L-shape of the 5-Hole probe, a device on which the probe can be mounted and sealed from leaking pressure was needed. The device contains 3 separate parts as depicted in Fig 4. Part1 is split in 2 symmetrical sides so it can be attached to any point of the probe without having the need of gliding it through any of the ends. There is a variable diameter hole inside this part. The smaller diameter is needed in order to create a flat smooth surface on the boundary between the canal and the cover. Either Teflon, for testing at ambient temperature or, copper/steel EMI Shielding screen for high temperature tests, can be used. Part1 will be mounted tight in Part2. The conical part of the device is used for creating a tight seal with the material used. During mounting, the conical surface pushes the sealing material towards the centre, thus making the seal tight.
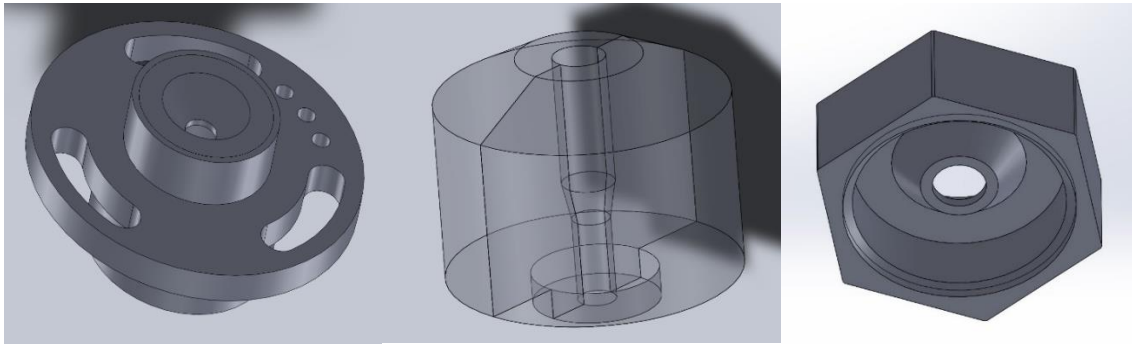
Fig. 4 Part1 (left); Part2 (middle); Part3 (right)

On the instrumentation cover we have drilled 3 concentric holes. The first one, that pierces through all material, allows the pressure probe to pass to the other side of the cover. The second hole, that is 17mm deep, creates the resting surface for Part1, as well as the surface needed for centring the device. The third hole creates the space needed for Part2. Part2 is not split. It is mounted on the probe by turning the probe at an angle, in order for the tip to pass through the hole in the centre of the part. Between Part1 and Part2 the sealing material is used.

Part3 was created to be able to make the sealing more controllable. There was a high risk of putting too much sealing material, which would cause Part2 to not sit tight on Part1, thus making the sealing unreliable. Part3 has an M24x2 thread that can be screwed over Part2. This pushes the sealing material inside even more towards the pressure probe, blocking the hole firmly.

As a result, there are 2 sealing zones that keep the pressure inside the channel. The sealing zones are presented in Fig 5 in blue. The first one is obtained using a simple gasket. The second one not only provides a tight sealing against pressure leak, but also supports keeping the pressure probe in place, blocking it for moving up or down. The faces that are represented with red lines are used for centring the parts.
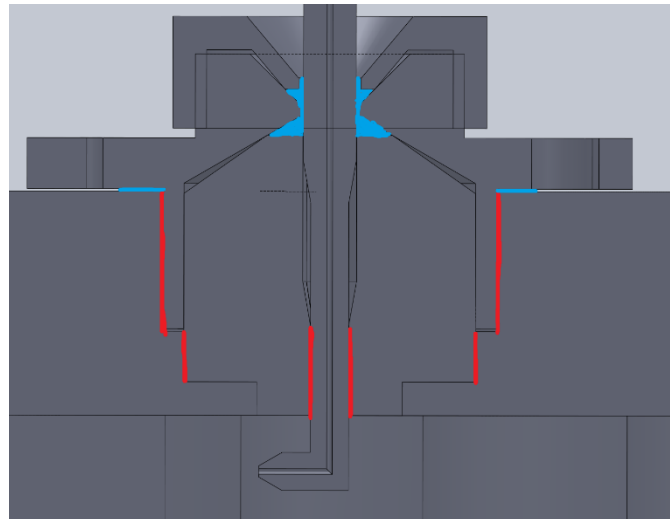

Fig. 5 Aeroprobe 5-hole device assembly mounting

2.3. Experimental test rig setup

In order to characterize the flow through the turbine row, the following flow parameters will be measured:
- Total pressure at the inlet of the experimental model
- Total temperature at the inlet of the experimental model
- Mass flow rate
- Static pressure along the Laval nozzle, where pressure is expected to vary the most
- Total pressure at the outlet of the stator
- Total pressure at the outlet of the experimental model.

For allowing the measurement of the parameters listed above, a dedicated test rig has been developed which is depicted in the diagram from Fig. 6. A list of the relevant components and their functioning ranges is also given in Table 1.
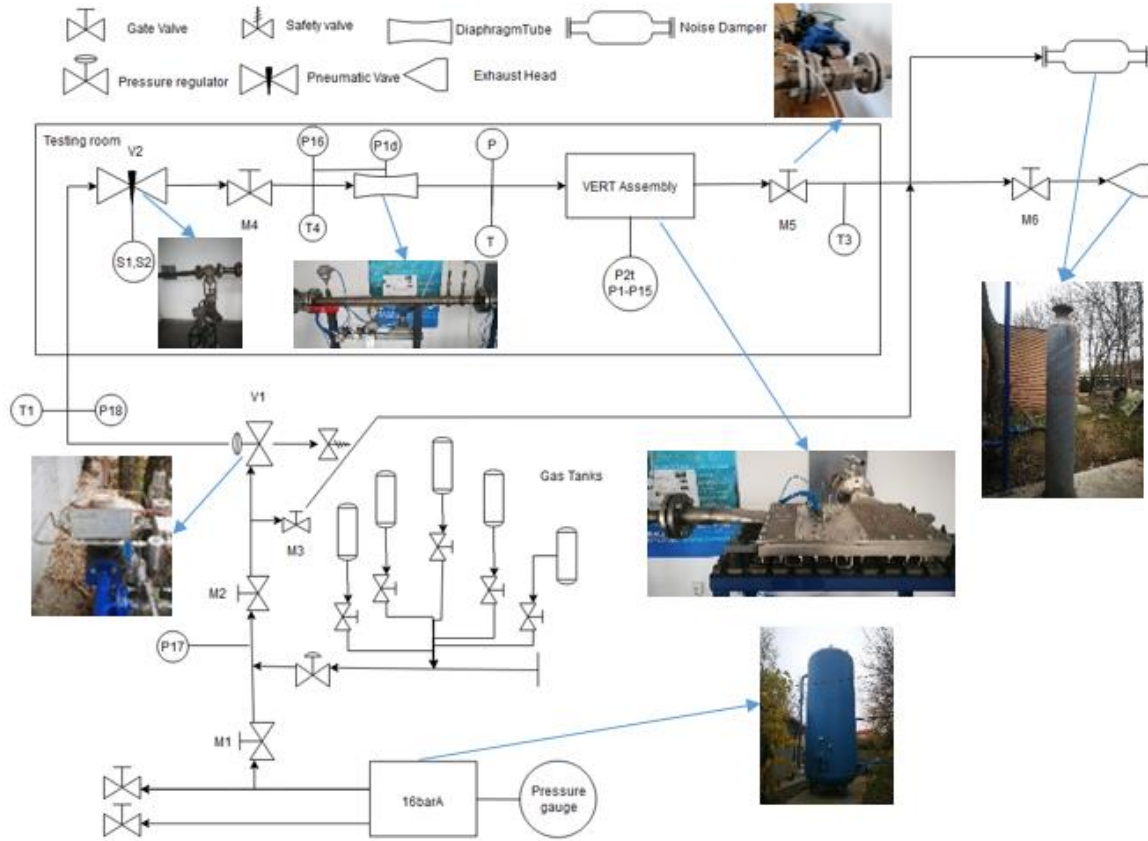

Fig. 6 Experimental Rig Diagram

Table 1. Relevant components

Nr.	Sensor/Location	Range	Accuracy	Measuring Device
1	Inlet Gas Temperature	-250 °C–600°C	0.1°	Resistance Temperature Detector
2	Outlet Gas Temperature	0 °C–200°C	0.015°	Thermocouple
3	Total/Static Pressure Inlet	0-51 barA		Existing Pressure Probe
4-8	Total Pressure between blade rows	0-51 barA		Aeroprobe 5-hole probe
9-18	Static pressure Stator	0-51 barA	±0.05%FS scanivalve accuracy	Existing Pressure Probe
19	Rosemount 3051SMV MultiVariable Transmitter	$P_{static}= -0.979 – 55.2$ bar $P_{differential}= 0 – 1$ bar		Diaphragm Tube
20	Rosemount 3051SMV MultiVariable Transmitter	-250 °C–600°C		Resistance Temperature Detector

21	Collector Tank Pressure	0-51 barA		Existing Pressure Probe
22	Flow control valve Inlet & Outlet Pressure	0-51 barA		Existing Pressure Probe
23				
24	ARCA ECOTROL853.8C1	-		Reading of opening percentage
25	ARCA ECOTROL853.8C1	-		Opening control
26	HABONIM pneumatic control valve C35 SR-2A2B	-		Reading of opening percentage
27	HABONIM pneumatic control valve C35 SR-2A2B	-		Opening control

The current capabilities of this test rig are summarized in Table 2.

Table 2. Test rig capabilities

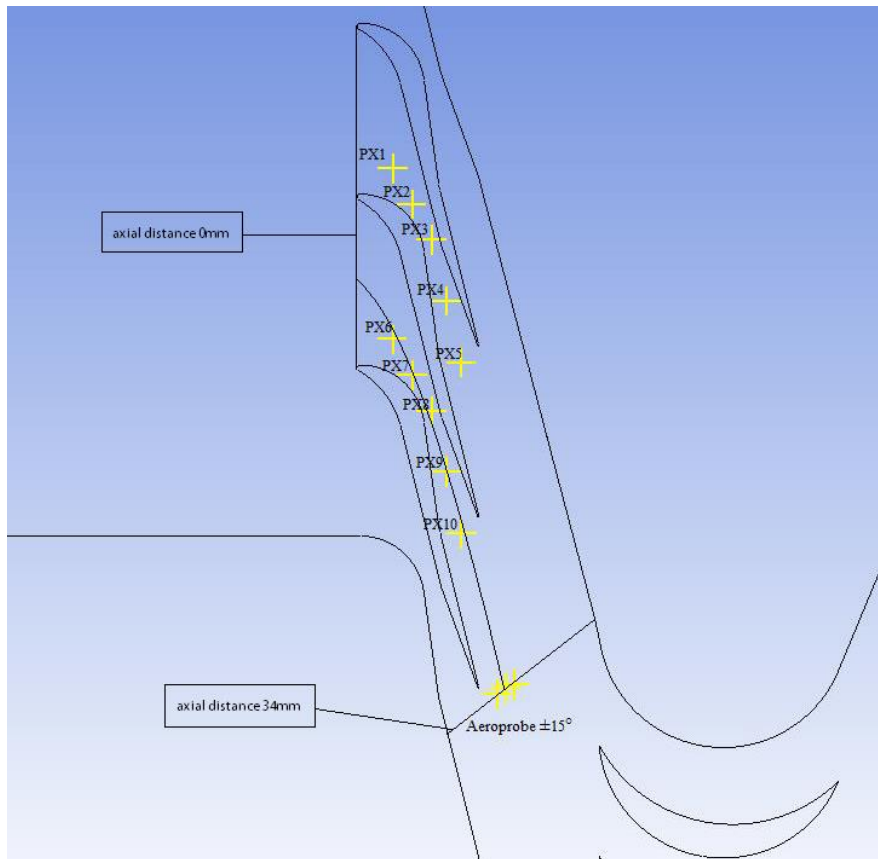| Fluid/Parameter	Inlet pressure [bar] (up to)	Outlet counter pressure [bar]	Inlet temperature [°C]	Maximum tested mass flow rate [kg/s]
Air	10	adjustable	ambient	0.1562
Methane	4.5	adjustable	ambient	0.0835

Fig. 7 Static pressure measurement points distribution inside the guide vanes and Aeroprobe location

Test rig capabilities are mainly constrained by the fluid feeding system. The air is provided from a reservoir filled with compressed air at 15 barA having a volume of 15 m³. Going for a higher pressure than the one described in Table 2 is not possible because of the rapid discharge of the reservoir and slow adjustment of the regulator and vanes in the desired position. The methane is provided by the local gas distributor and has a maximum pressure of 4.5 bar.

In Figure 7 one can see the distribution of the pressure measurement points along the guide vanes. The points have been placed in the middle of the channel along a streamline. The axial distance is measured from the entry section of the guide vane to right after the exit section where the Aeroprobe has been mounted. Given that there is supersonic flow before the Aeroprobe, we expect no interference inside the stator with the total pressure probe. The pressure drop along the guide vanes is one of the main objectives of the test rig.

3. Pressure measurement error

3.1. Static pressure measurement error inside the guide vanes flow channels

The pressure measurements conducted inside the guide vanes flow channels have an underlying error due to manufacturing process, measurement line and transducers accuracy. From the measurement line presented in Fig 8 we have no errors cause by the length of the tubing because the measured process is stationary. Ethernet cable transfer of data from the scanivalve to PXIe is neglected because it is very small compared to the precision of LabVIEW output data.
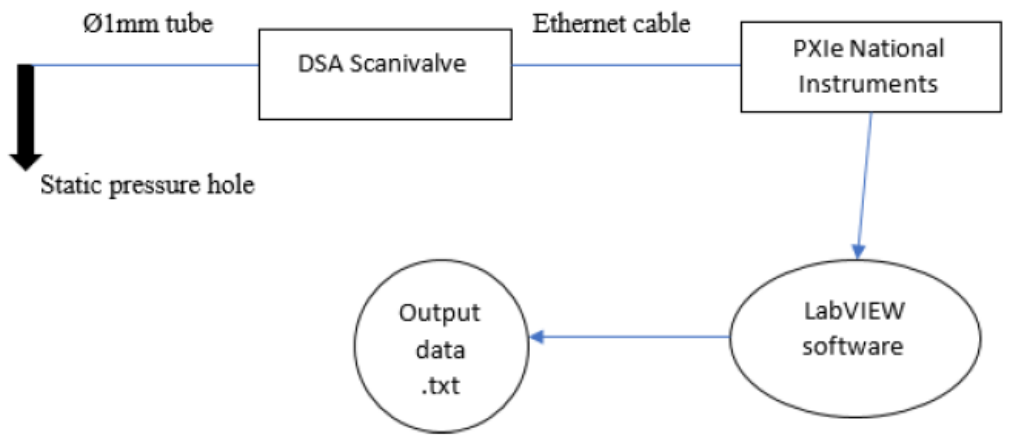

Fig. 8 Static pressure measurement line inside the guide vanes

Table 3. Error type

No	Cause	Observations	Error
1	DSA Scanivalve	Accuracy from Scanivalve data sheet	± 0.05%FS FS = 750psi
2	Hole angle	Probe hole angle 30°	+0.3%
3	Hole edges	Probe hole radius ¼ Ø	+0.2%
4	Hole dimension	Ø = 0.3mm; Mach < 1	+0.05%
5	Labview	Data saving precision	±0.001bar

To determine the measurement errors, the worst-case scenario for each of the error type presented in Table 3 is considered, as follows:

1) Scanivalve accuracy was taken from the DSA data sheet. An error of 0.05%FS translates into ±0.0258 bar for each measurement point. There is no need to take into account the accuracy related to the operating temperature if the experiments are done in an ambient temperature that fits in the interval given by the producer 0-60 °C for which there is no additional error, which is the case for these measurements.

2) Hole angle affects directly the pressure measurement. Depending on the orientation of the hole with respect to the fluid flow, a maximum error of 0.3% can occur because of the partial dynamic pressure captured by

60

the probe. Given the manufacturing method of the holes (laser cut), an inclination of 30° of the holes is impossible. Usually these types of machines give an angle deviation of maximum 1°. Since for this calculus we decided to take the worst-case scenario, the maximum value for this type of error as found in the literature was also considered.
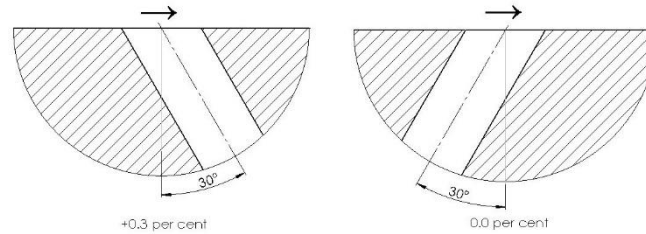

Fig. 9 Hole orientation angle [3]

3) Measuring static pressure with minimal error requires hole taps that present sharp edges that will not affect the flow passing over them. If a radius of curvature is applied to the hole edge, one would expect the inviscid flow streamlines to bend slightly downward into the hole, with a point of inflection near the point of separation [3]. The holes were cut from the side that comes in contact with the flow. This means they have developed a small radius inwards because of the heat produced by the laser. The radius size is really hard to determine because of the small dimensions of the holes (0.3mm diameter). Again, we have considered a scenario for which we have found error values in the literature and which will also cover the existent radius dimensions of the current hole taps.
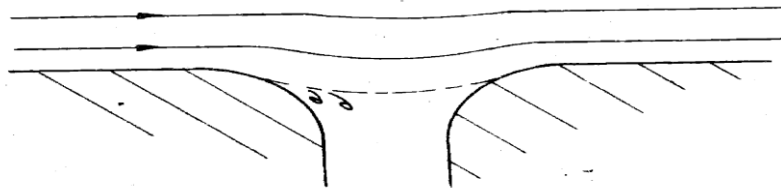

Fig. 10 Hole radius interference [3]

4) The shear stress of the boundary layer passing over the static pressure hole induces recirculating flows in the cavity, which in turn entrains relatively high momentum fluid from the free stream into the static pressure hole [3]. This results in a static pressure in the passage which is higher than the pressure on the surface. Hole diameters below 0.5mm have minimal errors compared to larger diameters [4]. The error is dependent on the Mach number in that region. Beyond Mach 1 there is no influence on the hole whatsoever if the diameter is at most ¼ of the height of the flow canal.

5) The software developed in LabVIEW for data acquisition provides an output data with 3-digit precision. This means it introduces an error of ±0.001bar for each pressure point measured.

Considering the highest static pressure measured inside the guide vanes flow channels for the error calculation (5 bar), the total error can be computed as follows:

$$\delta p = \sqrt{0.0258^2 + (5 \cdot 0.003)^2 + (5 \cdot 0.002)^2 + (5 \cdot 0.0005)^2 + 0.001^2} = \pm 0.03158 \, bar \qquad (1)$$
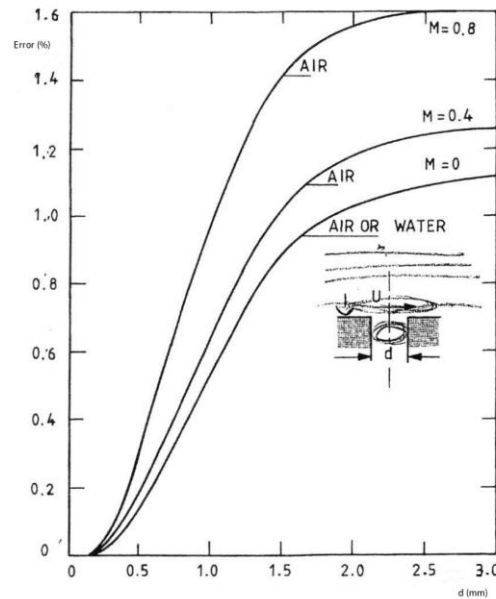
where δp is the static pressure error.

Fig. 11 Effect of hole size and Mach number on static pressure error [4]

4. RESULTS

Measurements were conducted on the test article described above for verifying the functionality of the experimental rig and demonstrating its capabilities. The air was fed through DN50 pipes to the experimental module. The pressure regulator was set at a pressure of 7 barA. The Electric ball Valve was used for achieving a constant pressure of 6 barA at the inlet of the experimental article during the experiment. The pneumatic valve from the exhaust of the experimental test article was used to induce varying back pressure in order to control and vary the flow regime. The registered parameters were saved and processed. The pressure distribution along the guide vanes flow channels for different flow regimes was plotted in Fig 12. The pressure was computed as a ratio between the measured pressure of the sensor and the inlet pressure. According to Fig 11, a full range of regimes were obtained experimentally, including:

- Subsonic isentropic flow, for which the theoretical pressure ratio between the back flow at the exit of the nozzle and the inlet pressure needs to be above 0.9575
- Shockwave inside the nozzle, for which the pressure ratio needs to be above the computed theoretic value for shockwave at the outlet of the nozzle, namely 0.4486
- Shockwave outside of the nozzle, for which the pressure ration needs to be below 0.4486
- Designed isentropic supersonic flow, for which the theoretic pressure ratio needs to be around 0.0685.

The pressure ratios described above have been calculated for the guide vanes geometry using the Area Mach number relation [5] and have been confirmed experimentally.
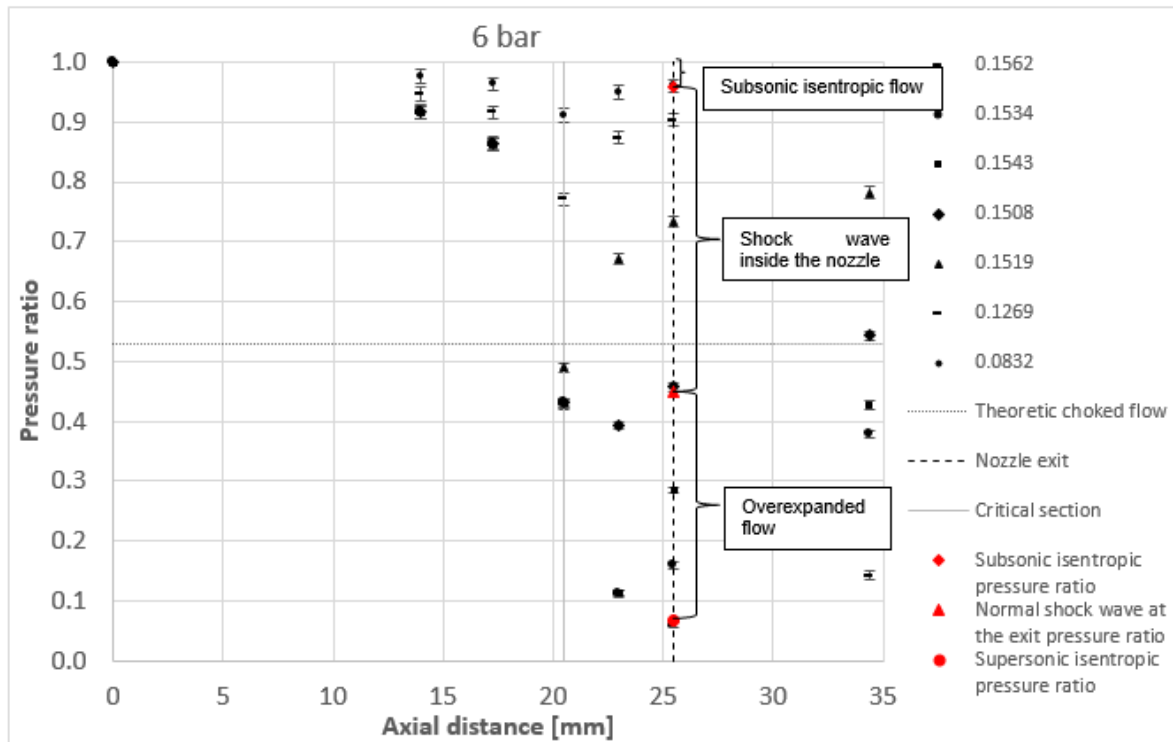
62

Fig 12 Pressure distribution along stator channel 1 for air at 6barA
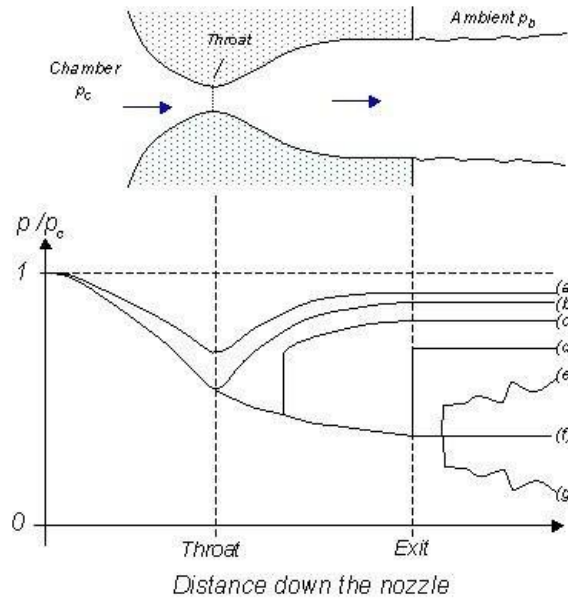

Fig 13 Fig. 1 CD Nozzle and its Pressure Distribution Along the Nozzle for different Flow Patterns (a) Subsonic (b) Chocked (c) Shock in Nozzle (d) Shock at Exit (e) Over Expanded (f) Design Condition (g) Under Expanded [6]

5. CONCLUSIONS AND FURTHER DEVELOPMENT

This paper presents the development of a new experimental test bench for supersonic turbine cascades of small dimensions. The 3D modelling of a test article is described along with the device used for mounting the 5-Hole Pressure Probe inside the supersonic jet. Relevant components of the test bench are presented as well as a diagram that shows the configuration of the test rig. The test rig current capabilities were summarized.

In the second part there is an analysis of the uncertainties of measuring the static pressure along the stator channels. The total error is calculated for the highest pressure measured (worst case scenario).

The functionality of the test bench and its capabilities were also verified and presented in the last part of this paper. The measurements show that all the possible flow regimes within the convergent-divergent shaped nozzles of the stator row have been achieved.

The test rig can be further developed to accommodate for other working fluids (like the flue gases of a combustion process), rotating turbomachinery, higher inlet temperatures and pressures and more detailed measurements. It can also be adapted to accommodate for other applications that would benefit from these working fluids and flow parameters. Improvements can be done for a higher accuracy control of the outlet pneumatic valve, thus allowing for a larger number of flow regimes to be measured.

ACKNOWLEDGEMENT

REFERENCES

[1] Moffitt TP. Design and experimental investigation of a single-stage turbine with a rotor entering relative Mach number of 2, NACA report no. RM E58F20a, 1958.

[2] Lee, Hanggi & Shin, Juhyun & Jeong, Eunhwan & Choi, Changho. (2016). Turbine Performance Experiments for the Turbopump of a Liquid Rocket Engine. International Journal of Aerospace System Engineering. 3. 25-29. 10.20910/IJASE.2016.3.1.25.

[3] Rayle, R.E. Jr.: "An investigation of the influence of orifice geometry on static pressure measurements." M.S. Thesis, M.I.T., 1949

[4] J. Anthoine et al. "Measurement Techniques in Fluid Dynamics"; von Karman Institute for Fluid Dynamics; 3rd revised edition

[5] Dr Hui Hu "Lecture # 12: Shock Waves and De Laval Nozzle Lecture # 12: Shock Waves and De Laval Nozzle"; Department of Aerospace Engineering Department of Aerospace Engineering Iowa State University Iowa State University Ames, Iowa 50011, U.S.A Ames, Iowa 50011, U.S.A

[6] Modeling and Simulation of a Supersonic Convergent Divergent Nozzle Using Computational Fluid Dynamics (CFD) - Scientific Figure on ResearchGate. Available from: https://www.researchgate.net/figure/CD-Nozzle-and-its-Pressure-Distribution-Along-the-Nozzle-for-different-Flow-Patterns-a_fig1_330738735 [accessed 8 Dec, 2020]

COMOTI
INNOVATES FOR
A CLEAN BETTER WORLD